Quantifying and Enhancing Puncture Resistance in Railroad Tank Cars Carrying Hazardous Materials

Phase I: Preliminary Study

Prepared for

Transportation Issues Team
The Chlorine Institute
Arlington, VA

Prepared by

Ted L. Anderson, Ph.D., P.E.
Structural Reliability Technology, Inc.
Boulder, CO

Steven W. Kirkpatrick, Ph.D.
Applied Research Associates, Inc.
Mountain View, CA

September 1, 2006

SRT
2465 Central Avenue, Suite 110
Boulder, CO 80301
(303) 415-1475 (Ph)
(303) 415-1847 (fax)
www.srt-boulder.com

APPLIED RESEARCH ASSOCIATES, INC.
2672 Bayshore Parkway, Suite 1035
Mountain View, CA 94043
(650) 625 8150 (Ph)
(650) 625-8145 (fax)
www.arasvo.com

EXECUTIVE SUMMARY

This report is a critical assessment of puncture resistance and the potential for lading loss in tank cars. The effect of material properties and tank car design on puncture resistance is examined.

An overview of the fracture behavior of steels is presented, followed by a discussion on possible improvements in tank car materials. Much of the previous work on improvements in steel for tank car applications has focused on low-temperature toughness properties. However it is the resistance to *ductile* fracture that is the most important factor in lading loss because most punctures occur by ductile rupture. The authors recommend that the next generation of tank car steel have very low sulfur content and sulfide shape control to provide superior upper-shelf toughness. Further work is necessary to determine whether a carbon-manganese steel or a microalloyed steel would be better suited for tank car applications.

An examination of trends from prior accident data led to the development of a predictive model that quantifies the effect of design modification and material properties. For existing chlorine tank cars, the model and prior accident data indicate that a total of 44 punctures through the head and shell (combined) are expected for every 1000 cars involved in a mainline accident. If the proposed design modifications for chlorine cars (i.e., increased wall thicknesses, addition of head shields) are adopted, but tank car steel quality is unchanged, the model predicts 12 punctures per 1000 cars. However, if a new steel with, hypothetically, twice the puncture resistance is adopted, the predicted punctures decrease from 44 to 2 per 1000 cars if the design remains unchanged. If *both* the steel and design are improved, the model predicts 2 punctures per 10,000 cars.

To validate the conclusions of the puncture model, a puncture resistance test for tank car materials is desirable. As part of a preliminary effort to develop a puncture test, a series of computer simulations of fracture and puncture were performed. These analyses were restricted to relatively small-scale laboratory experiments. Full-scale simulations of tank car punctures are recommended for a subsequent phase.

This report includes previously unpublished work performed by the authors as part of their investigation of the recent derailment near Minot, ND. This work includes experimental data and detailed nonlinear dynamic computer simulations. Many of the computational procedures developed in the Minot investigation will be applicable to full-scale puncture simulations, which will be undertaken in a future study.

TABLE OF CONTENTS

1 BACKGROUND

When a derailment or other rail accident occurs, the resulting collision forces can lead to a loss of lading from tank cars. While such an event is always undesirable, it is particularly damaging when the cars contain a hazardous material. Two relatively recent derailments in Minot, ND [1,2] and Graniteville, SC [3] that resulted in significant releases of hazardous materials have heightened the concern over lading loss during rail accidents. There is a strong desire in the rail industry to develop a new generation of tank cars that are more resistant to puncture in the event of an accident.

In recent years, normalization of steels for tank cars carrying gases has become mandatory. The requirement reduces the incidence of brittle failures during rail accidents. However, the accident data has shown that the normalization requirement has had a negligible effect on the frequency of lading loss. The overwhelming majority of lading loss incidents are ductile failures [4, 5]. Normalization provides no significant protection against ductile puncture or ductile fracture.

There are a number of ways to increase the puncture resistance of tank cars, including:

1. Increasing the thickness of the shell and head.
2. Adding head shields and jackets.
3. Using modern high-toughness steels in place of traditional carbon steels.

Other possible remedies have been proposed, such as honeycomb and crumble zones. A major difficulty is that there is presently no recognized method to quantify the improvement in puncture resistance of a proposed design. Past accident data can be used to infer the relative benefits of increases in plate thickness, but there are practical limits to section thickness. Tougher steel *should* result in an improvement in puncture resistance, but quantifying this benefit is difficult.

This report takes a critical look at the issue of puncture resistance. There is an extensive discussion of the effect of material properties on puncture resistance, and we offer recommendations on potential next-generation steels. A database of previous rail accidents is used to assess the effect of tank car design features such as wall thickness, jackets, and head shields. A model is developed to explain the trends in previous accident data and to predict the effect of design modifications. Finally, some preliminary computer simulations of fracture and puncture are performed.

This report includes previously unpublished experimental and computational results from the investigation of the Minot, ND derailment.

2 EFFECT OF MATERIAL PROPERTIES ON PUNCTURE RESISTANCE

This chapter begins with a brief review of the microscopic mechanisms of fracture in ferritic steel (Section 2.1), followed by a discussion of the effect of chemistry and microstructure on fracture resistance (Section 2.2). These fundamental principles lead directly to the authors' recommendations for steels with improved puncture resistance, which are presented in Section 2.3.

2.1 Fracture Mechanisms in Steel

The two fracture mechanisms that are of primary interest in tank car steels are illustrated in Figure 2.1 [6]. Cleavage fracture is characterized by rapid transgranular crack propagation. It is referred to as *brittle* fracture, but it can be preceded by significant plastic deformation. Ductile fracture occurs through the nucleation and growth of microscopic voids at nonmetallic inclusions, usually manganese sulfide (MnS). These two mechanisms are described further below.

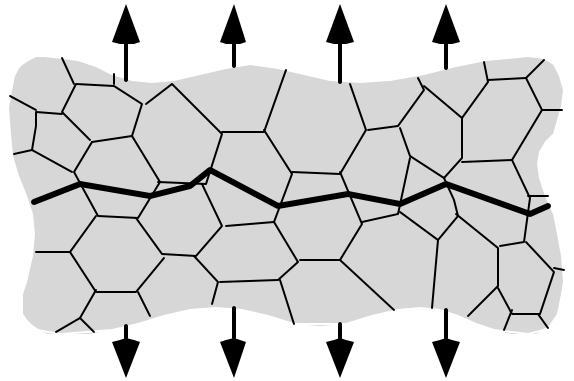

a) Brittle fracture (cleavage).

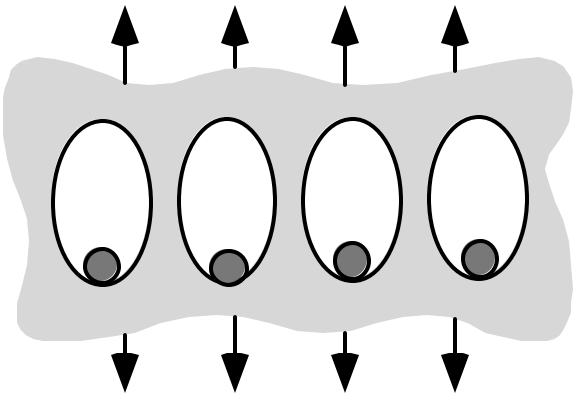

b) Ductile fracture (microvoid coalescence).

FIGURE 2.1 Fracture mechanism in steel [6].

2.1.1 Cleavage (Brittle) Fracture

A photograph of a brittle fracture in a tank car is shown in Figure 2.2 [1]. The fracture surface in a typical brittle failure is flat and is perpendicular to the principal stress direction. In coarse-grained steels, shiny facets can be seen at low magnifications. Higher magnifications are necessary to discern cleavage facets in fine-grained steels. Figure 2.3 is a scanning electron microscope (SEM) photograph of cleavage in a low-alloy steel. The lines on each facet are called *river patterns*.

In body-centered cubic (BCC) metals such as ferritic iron, cleavage fracture occurs on the cube faces of the unit cell, which have the lowest packing density in the crystal. That is, there are fewer bonds to break per unit area on preferred cleavage planes than on other planes in the crystal. In polycrystalline metals with randomly oriented grains, a cleavage crack must change directions each time it crosses a grain boundary.

The formation of river patterns as a result of the twist angle between cleavage planes in adjoining grains is illustrated in Figure 2.4. When the crack reaches a grain boundary, it must immediately change orientations to accommodate the nearest cleavage plane on the adjoining grain. This causes the crack to split into a number of parallel fracture planes. These parallel planes link up by tearing. As the fracture propagates across the grain, the parallel fracture planes merge. This process is repeated when the cleavage crack reaches another grain boundary. The river patterns can be used to infer the crack propagation direction on the microscopic scale. Figure 2.5 is an SEM photograph that shows a close-up of river patterns in a low-alloy steel. The resistance to cleavage fracture increases with decreasing grain size, due in large part to the energy dissipation that occurs when cleavage cracks cross grain boundaries.

FIGURE 2.2 Brittle fracture in an anhydrous ammonia tank car that derailed near Minot, ND [1].

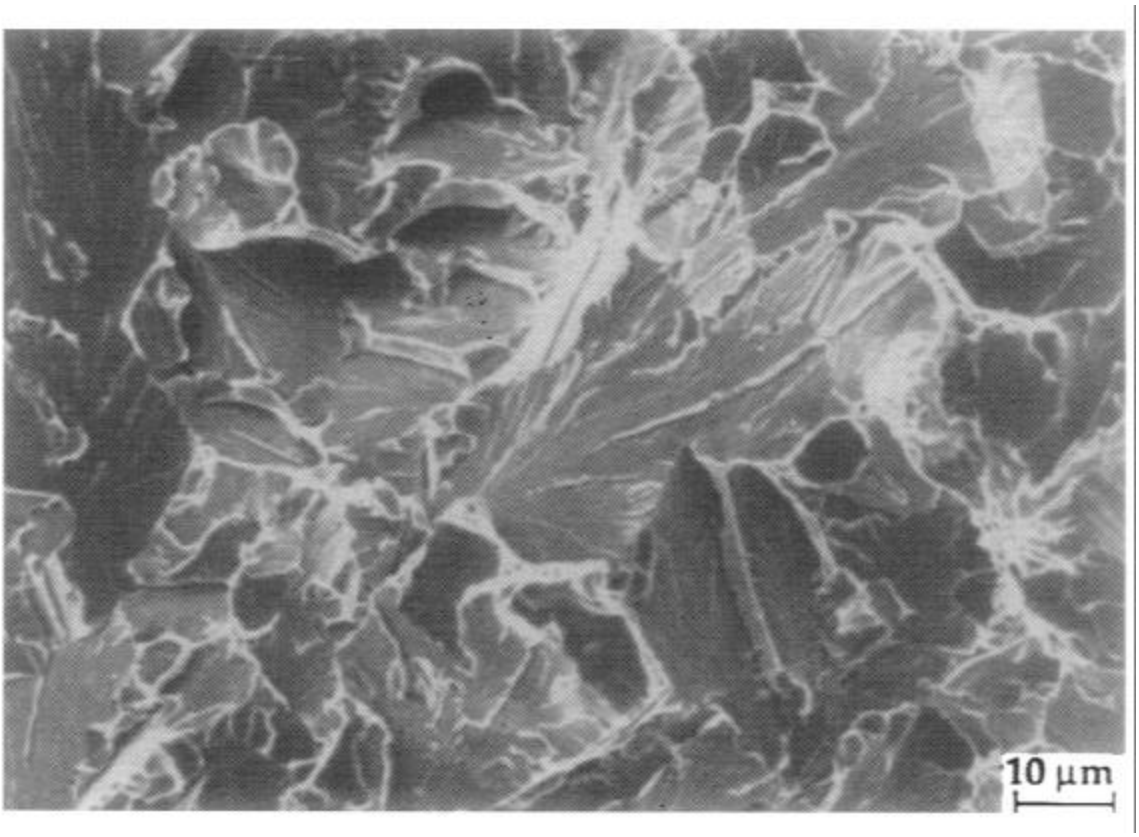

FIGURE 2.3 SEM photograph of transgranular cleavage fracture in steel [6].

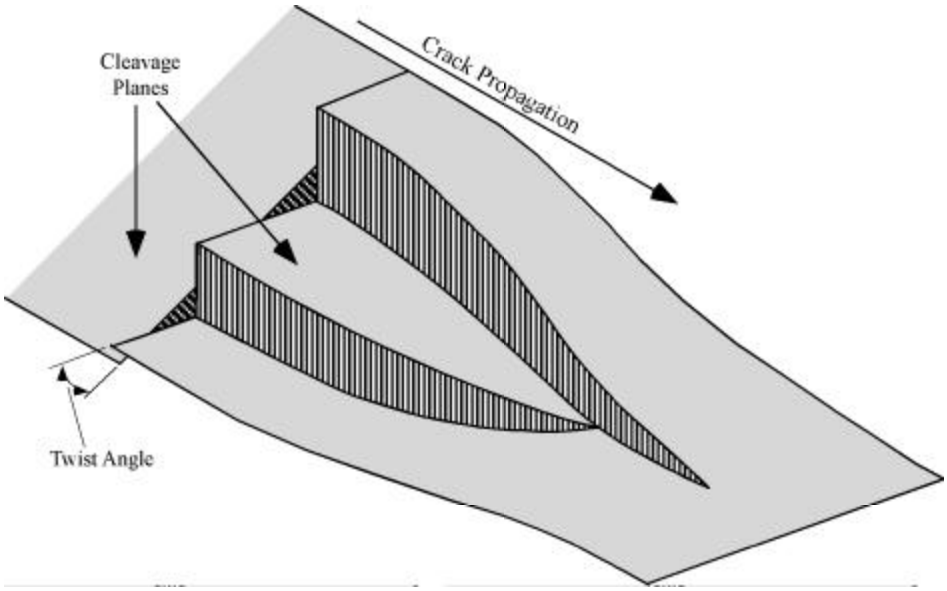

FIGURE 2.4 Formation of river patterns as a result of cleavage fracture crossing a twist boundary [6].

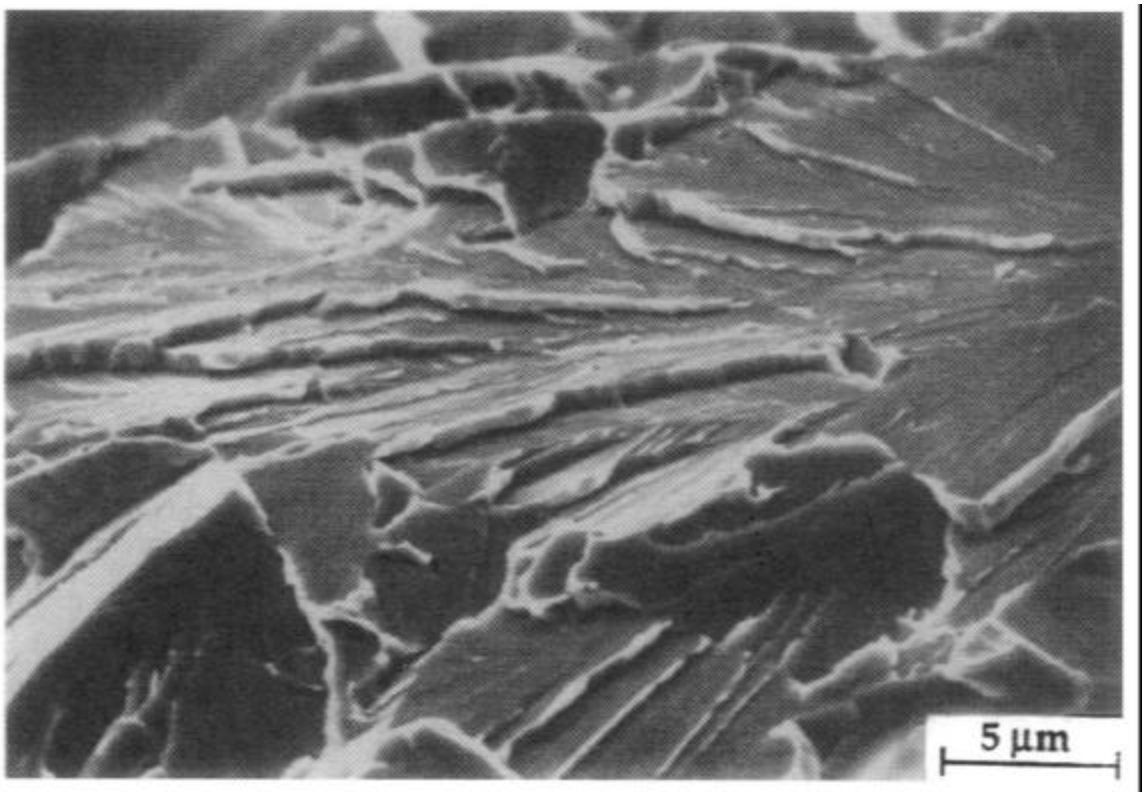

FIGURE 2.5 SEM photograph of river patterns in steel [6]. The light areas correspond to tearing between parallel cleavage planes.

2.1.2 Ductile Rupture (Microvoid Coalescence)

The microscopic processes that result in ductile fracture are illustrated in Figure 2.6 [6]. Microvoids that nucleate at inclusions grow as a result of plastic strain. Plastic strain concentrates between voids, resulting in local necking and coalescence (fracture). Figure 2.7 is an SEM photograph of the fracture surface of a material that failed by microvoid coalescence.

Macroscopically, ductile fracture tends to have a dull appearance, compared to the shiny faceted surface that is characteristic of cleavage fracture. In some instances, the fracture surface of a ductile failure is oriented approximately 45 degrees from the applied stress. Figure 2.8 is a photograph of a 45-degree ductile fracture in the head of an ammonia tank car that derailed near Minot, ND [1].

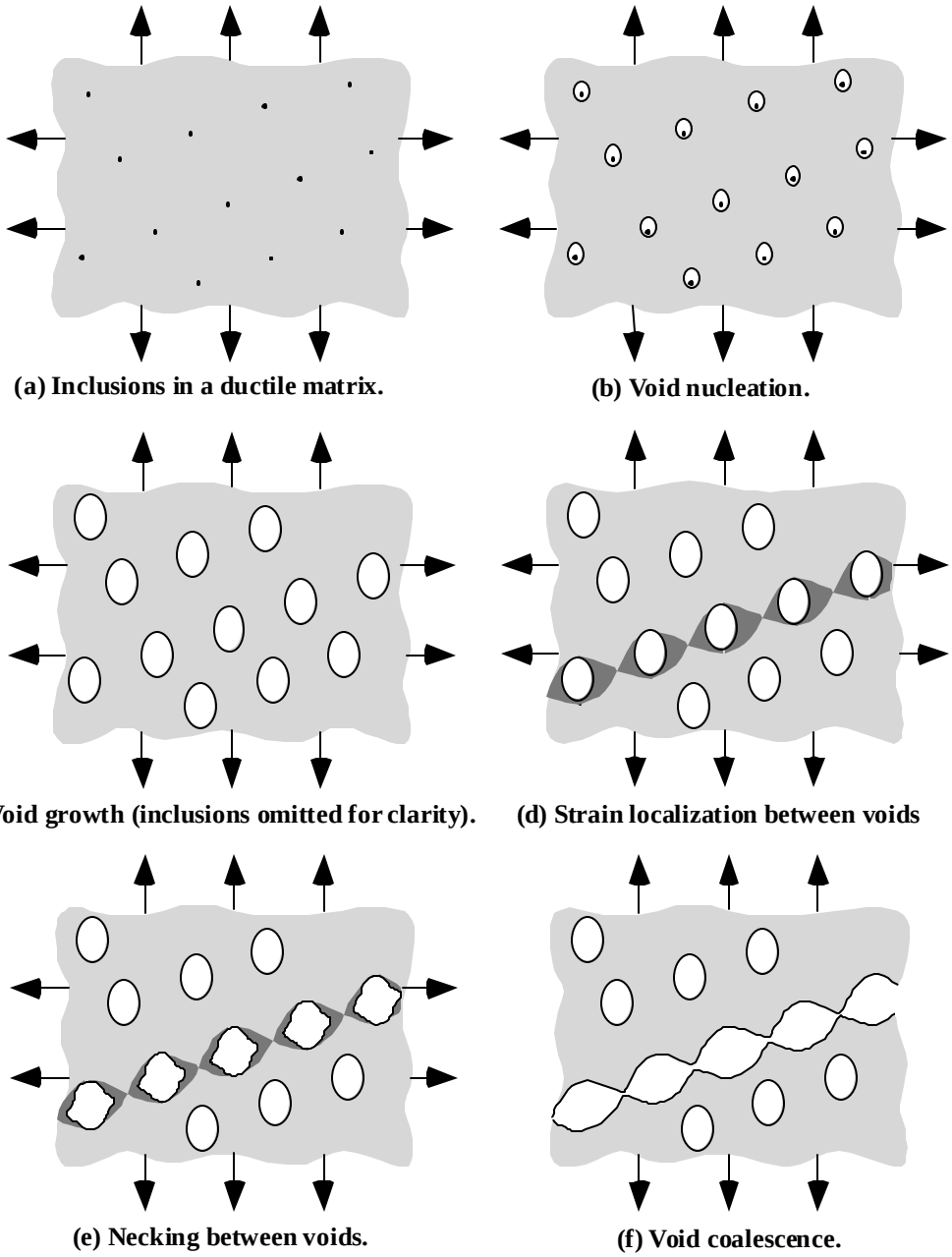

(a) Inclusions in a ductile matrix.

(b) Void nucleation.

(c) Void growth (inclusions omitted for clarity).

(d) Strain localization between voids

(e) Necking between voids.

(f) Void coalescence.

FIGURE 2.6 Void nucleation, growth, and coalescence in metals [6].

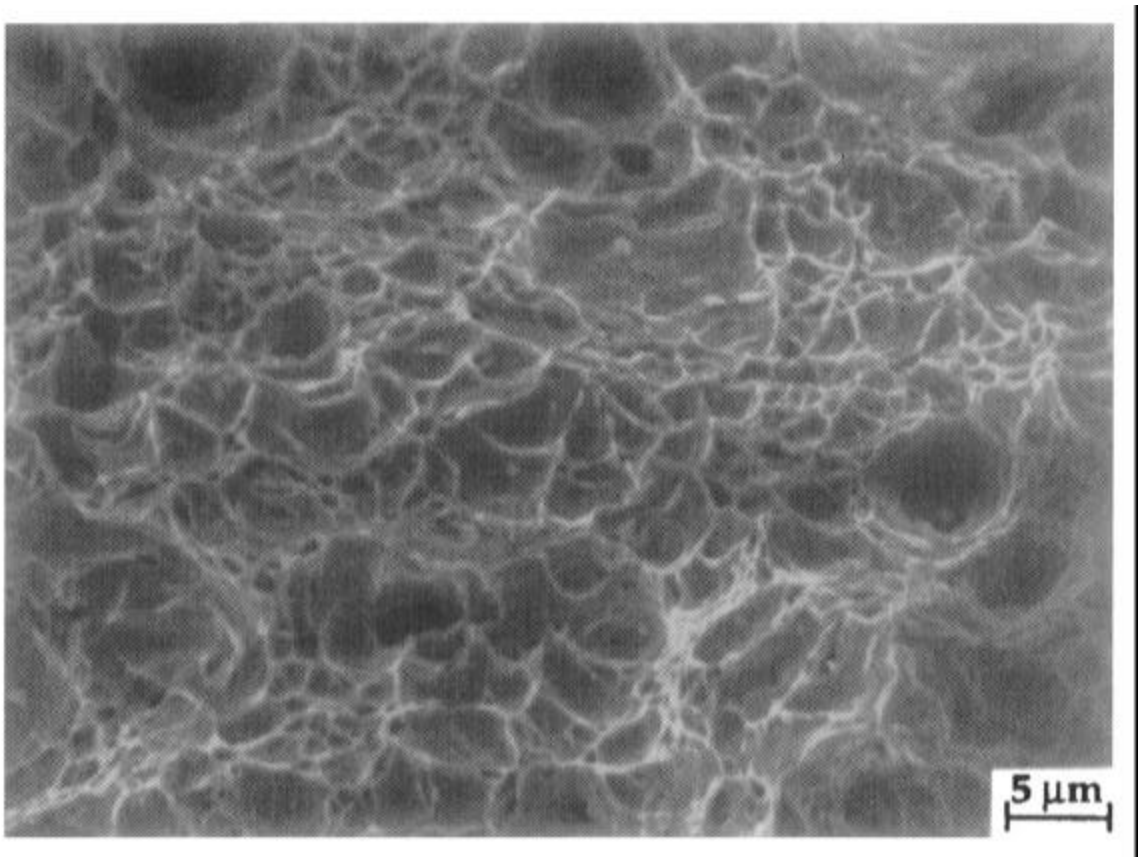

FIGURE 2.7 SEM photograph of microvoid coalescence in steel.

FIGURE 2.8 Ductile fracture in an anhydrous ammonia tank car that derailed near Minot, ND [1].

2.1.3 The Ductile-Brittle Transition

Carbon steels exhibit a transition from to ductile to brittle behavior as temperature decreases. Figure 2.9 illustrates the temperature dependence of toughness in steels. At high temperatures, the material is on the upper shelf, where the fracture mechanism is microvoid coalescence. On the lower shelf, the toughness is low and the fracture mechanism is cleavage. A mixture of cleavage and microvoid coalescence is typically observed in the transition region between the lower and upper shelves.

2.2 Effect of Steel Chemistry and Microstructure

A number of metallurgical variables affect a steel's resistance to cleavage fracture and microvoid coalescence. Figure 2.10 illustrates the most important parameters that influence toughness. Beginning with a baseline steel, its toughness properties can be improved through a variety of means. Refinement of ferrite grain size results in a downward shift in the ductile-brittle transition curve. Desulfurization and sulfide shape control increase the upper shelf toughness relative to the baseline.

Ferrite grain size refinement, which results in improved cleavage resistance and a downward shift in the transition temperature, can be achieved through a variety of means. Normalization, where steel is air cooled from approximately 1700°F, is the traditional method for grain refinement. Modern steelmaking procedures such as microalloying and thermomechanical controlled processing (TMCP) can produce ultra-fine grain structures with excellent strength and low-temperature toughness.

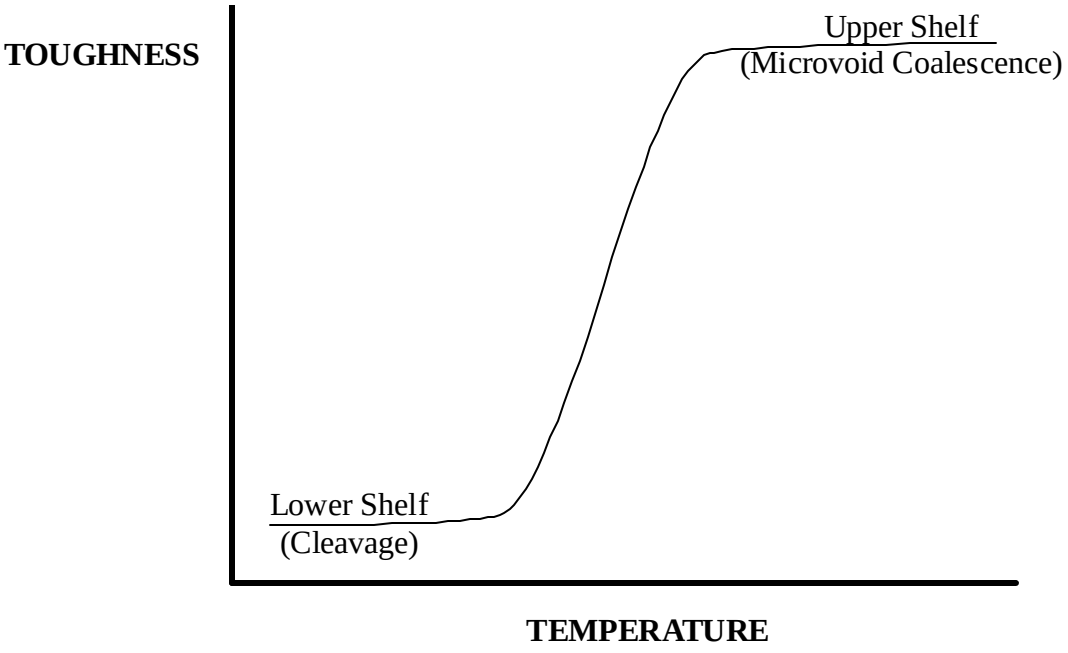

FIGURE 2.9 The ductile-brittle transition in steels.

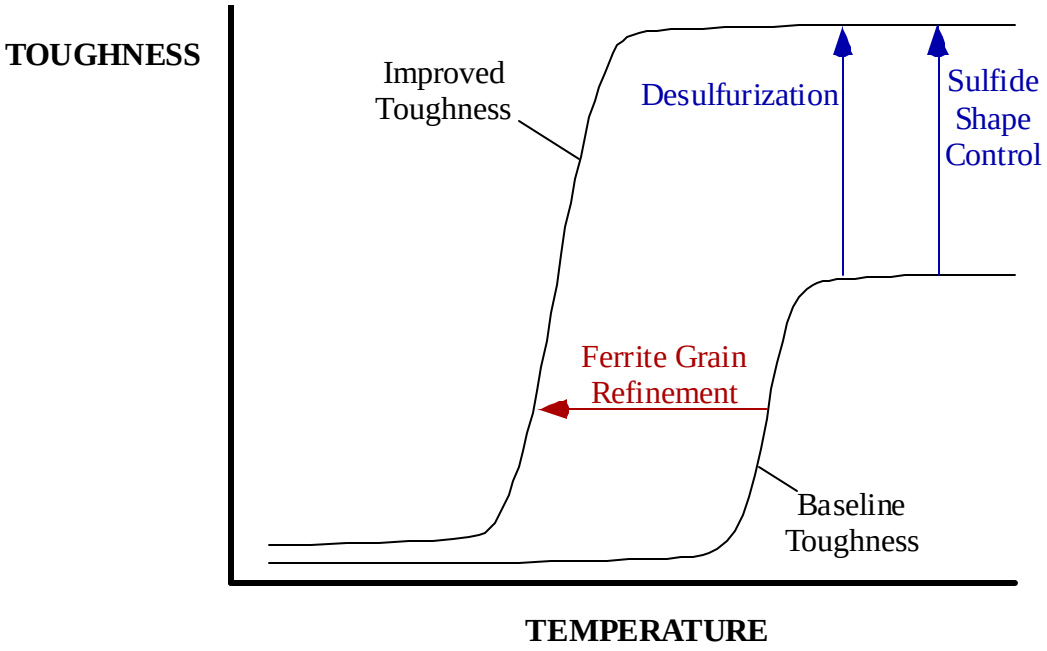

FIGURE 2.10 Effect of microstructure on the toughness of steel.

Over the past 30 years, efforts to improve the toughness of tank car steels have focused almost exclusively on low-temperature properties (i.e., downward shifts in the transition temperature) [7-10]. However, it is the *upper shelf* toughness that dictates puncture resistance, as discussed in Section 2.3 below. In steels, microvoid coalescence nucleates predominately at MnS inclusions. Therefore, reductions in sulfur content directly translate to increased upper-shelf toughness. Moreover, the *shape* of MnS inclusions has a pronounced effect on ductile fracture behavior.

Figure 2.11 illustrates two inclusion morphologies in steel. When a steel plate is hot rolled, inclusions tend to elongate into sulfide stringers, as the upper sketch in Fig. 2.11 illustrates. The goal of sulfide shape control is to create spherical inclusions, as illustrated in the lower sketch. In the past, sulfide shape control was accomplished by adding small amounts of rare earth metals to the molten steel. This practice tended to result in weldability problems, however. More recently, sulfide shape control has typically been achieved through CaSi additions, which have the added benefit of reducing the sulfur content in the steel.

In the absence of sulfide shape control, the upper shelf toughness can be highly anisotropic. That is, the Charpy V-notch (CVN) energy is affected by the notch orientation relative to the rolling direction. Figure 2.12 illustrates CVN specimens with longitudinal and transverse orientation. Figure 2.13 compares the transverse and longitudinal CVN transition curves for an anhydrous ammonia car that sustained a 360-degree shell fracture during the Minot derailment [2]. Figure 2.14 is a photograph of the fracture surface from this car. The crack propagated circumferentially in the shell, which corresponds to the rolling direction. This low-energy ductile fracture has a “woody”

appearance because the crack ran along sulfide stringers. A wood analogy is apt here: just as it is easier to split wood along the grain than against the grain, less energy is required to propagate a crack in the longitudinal direction in a steel plate with sulfide stringers.

As a result of the Minot derailment, a total of 7 anhydrous ammonia cars lost all of their lading due to punctures and fractures through the head and/or shell. Each of these cars was built in the 1970s. Testing on head and shell samples extracted from the damaged cars indicated that the steel met the tensile and chemistry requirements of the TC 128B specification that existed at the time of construction [1, 2]. The current TC 128B specification limits the sulfur content to 0.015%, while the limit was 0.040% when the Minot cars were built. Another substantial change in the specification for tank car steels over this period occurred in 1989, when a requirement to normalize the head and shell steel was introduced. To this day, the TC 128B specification does not require sulfide shape control in the steelmaking process.

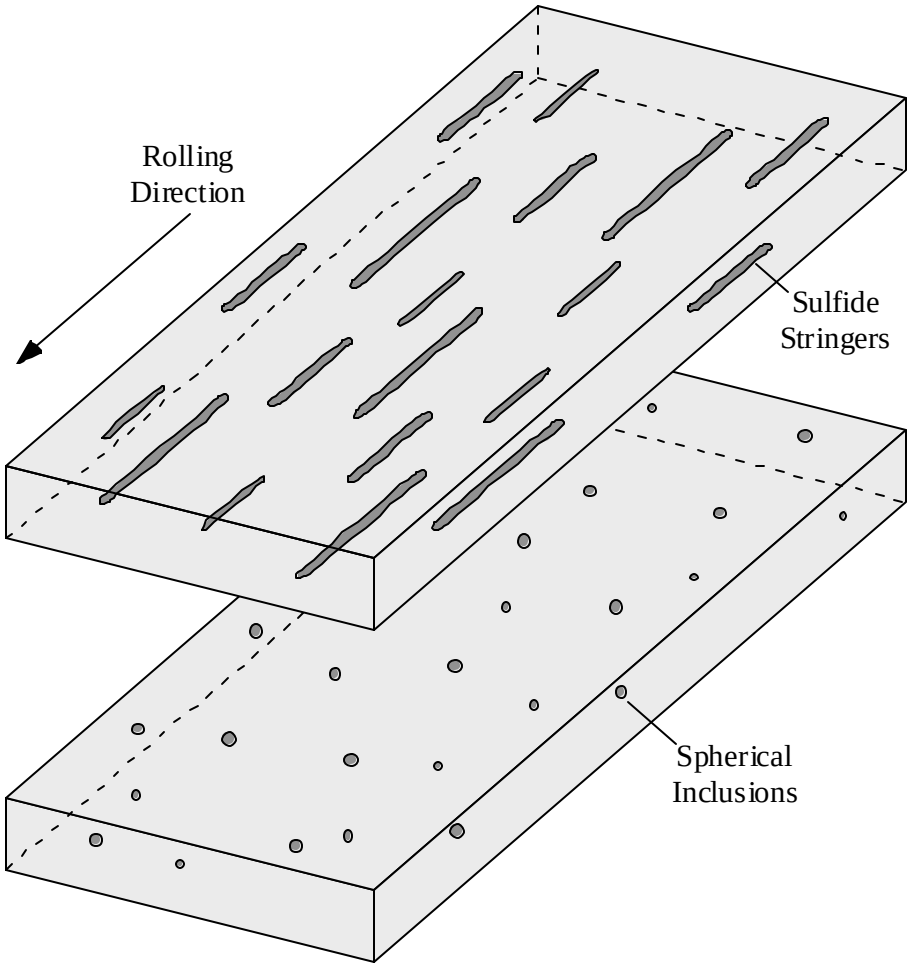

FIGURE 2.11 Sulfide shape control results in spherical inclusions instead of sulfide stringers.

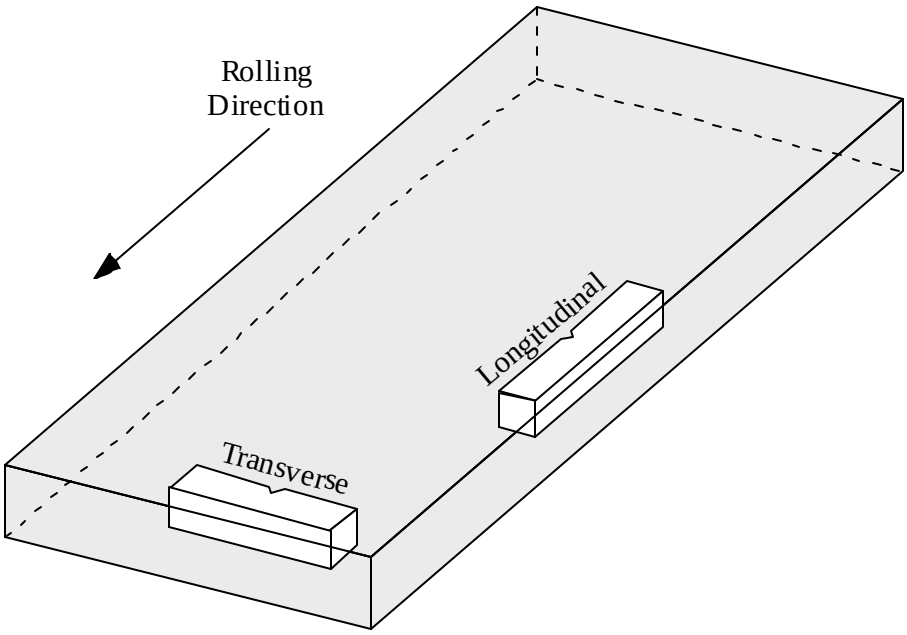

FIGURE 2.12 Orientation of Charpy specimens relative to the rolling direction.

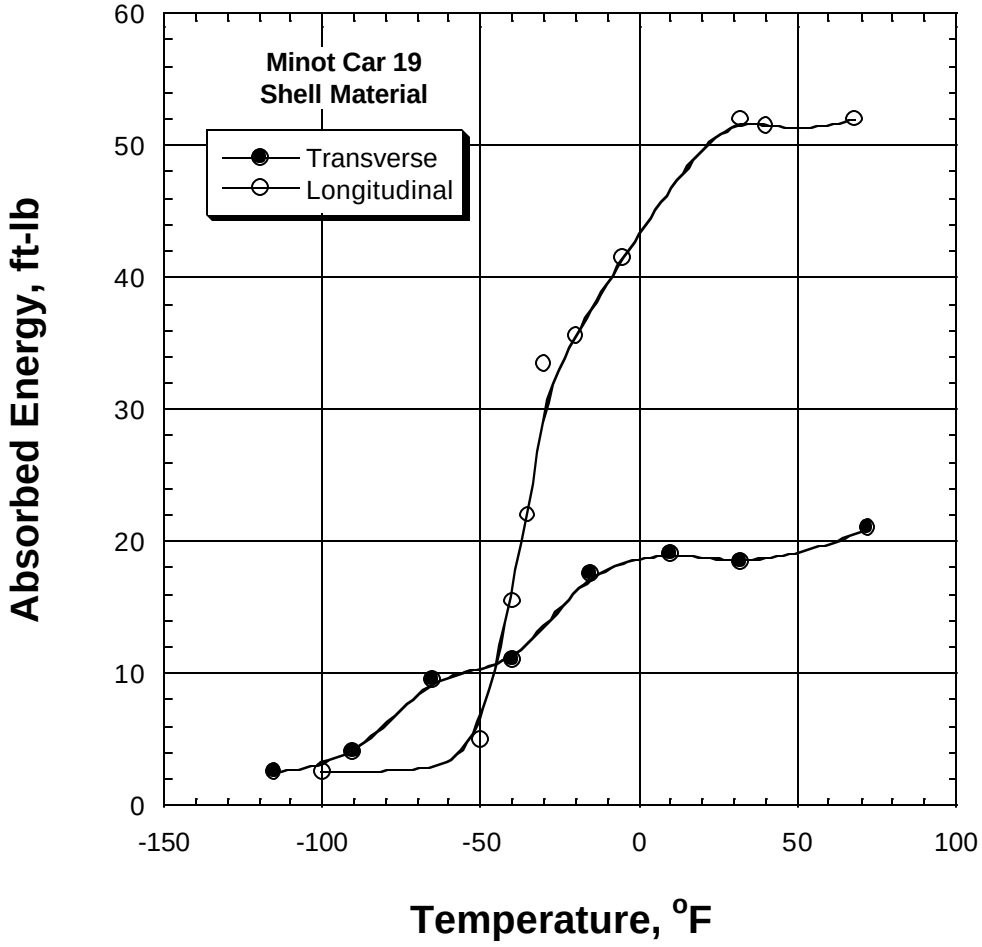

FIGURE 2.13 Effect of CVN specimen orientation on toughness in an ammonia tank car that derailed near Minot, ND [2].

FIGURE 2.14 Low-energy ductile fracture in Minot Car 19 [1]. The fracture propagated in the longitudinal direction, along sulfide stringers, which resulted in a "woody" appearance.

During the Minot investigation, various tests were performed on steels from the subject cars, as well as on exemplar tank car steels. One of the exemplar materials was a 1999 vintage normalized TC 128B plate. Figures 2.15 and 2.16 compare the microstructures of a 1970s vintage steel from the Minot derailment with the modern steel plate. The most obvious difference is that the modern normalized plate has a finer ferrite grain size than the older steel, as expected. The modern plate also has a lower sulfur content than the older steel. Apparently, neither plate was manufactured with sulfide shape control, as discussed below.

The Minot testing program included high-rate fracture mechanics tests, which were performed at Southwest Research Institute in San Antonio [11]. Figures 2.17 and 2.18 compare the fracture surfaces of specimens extracted from the two plates whose microstructures are shown in Figs. 2.15 and 2.16, respectively. The crack propagation direction was longitudinal in both cases. The fracture surface in Fig. 2.17 has a "corrugated roof" appearance. Fracture along sulfide stringers created troughs, which reflect the light in the photograph. The fracture surface of the modern plate (Fig. 2.18) also shows troughs, which are indicative of sulfide stringers. There are fewer such features on Fig. 2.18 than on Fig. 2.17, which is due to lower sulfur content in the former case. Nevertheless, the upper-shelf toughness of modern tank car steels could be significantly improved through sulfide shape control.

In order to demonstrate the effect of normalization on toughness, the NTSB heat treated a sample extracted from one of the cars damaged in the Minot derailment [1, 2]. The resulting toughness comparison is plotted in Fig. 2.19. There is a difference in upper-shelf toughness between longitudinal and transverse CVN specimens, as was the case in Fig. 2.13. When this plate was subject to a normalizing heat treatment, the expected leftward shift in the transition curve occurred. Moreover, there was a slight improvement

in the upper shelf toughness. Since normalization does not affect MnS inclusions, this improvement in upper shelf toughness is likely due to a grain size strengthening effect, which is described below.

Figure 2.20 schematically illustrates the effect of grain refinement on a material's stress-strain curve. Assuming ductility remains constant, the fracture energy, which is proportional to the area under the stress-strain curve, would be higher for the fine-grained material. However, the trend in Fig. 2.19 does not prove that normalized TC 128 B has better upper shelf toughness than as-rolled TC 128 B plates in general. The strength requirements for both normalized and as-rolled plates are the same, and steelmakers are given substantial latitude in how they meet the minimum tensile properties. In normalized plate, a steelmaker can take advantage of grain size strengthening by reducing the amount of certain alloying elements that contribute to strength. Given the same sulfur content and tensile properties, there should be no systematic difference in the upper-shelf toughness of as-rolled versus normalized TC 128 B plates. Normalization per se does not result in improved upper shelf toughness.

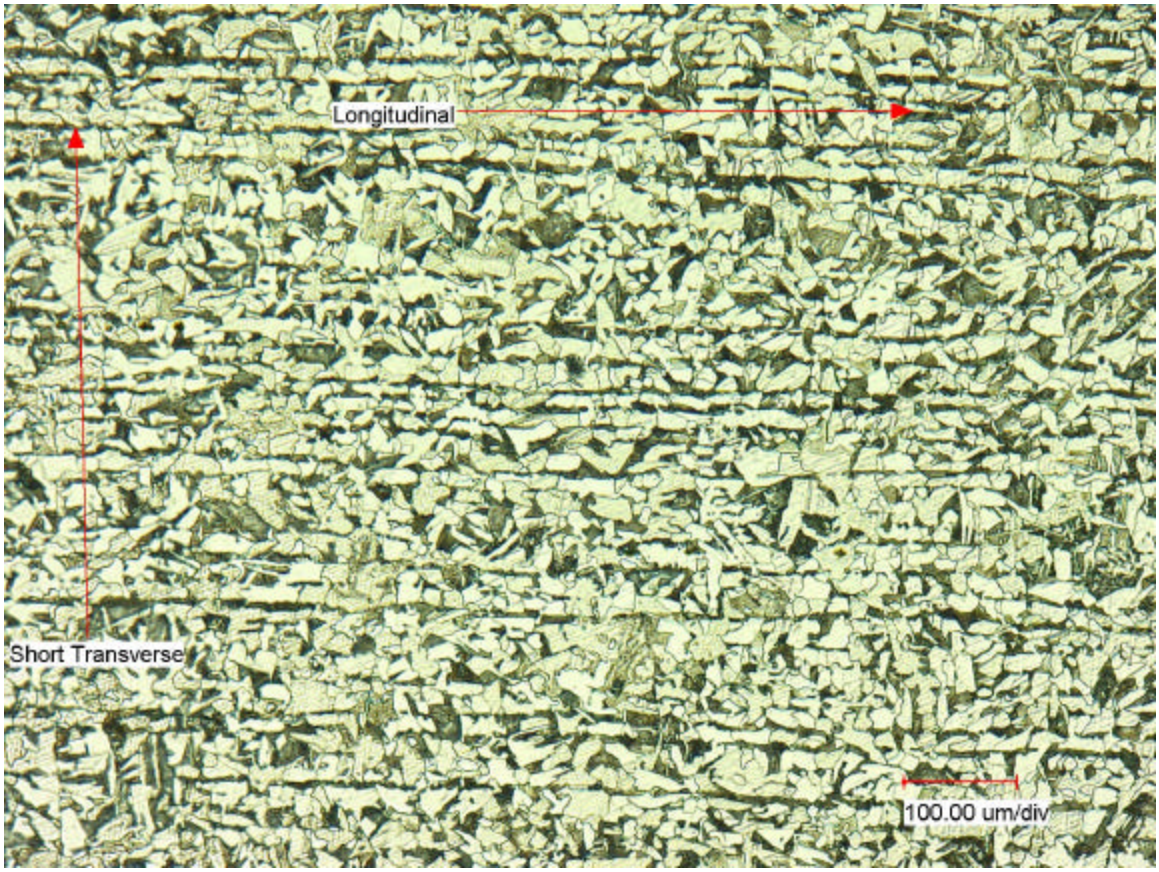

FIGURE 2.15 Microstructure of a 1970s vintage TC 128 B steel sample taken from the shell of Minot Car 22 [11].

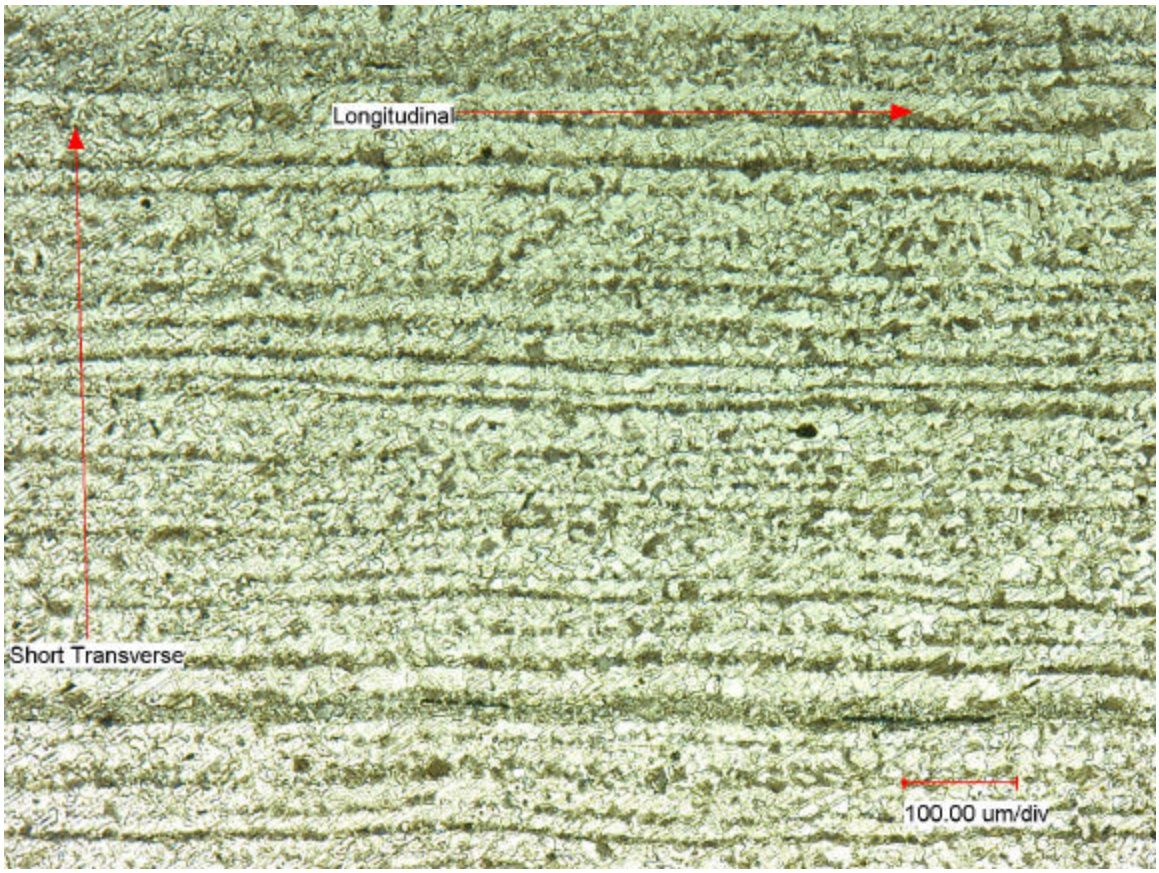

FIGURE 2.16 Microstructure of a 1999 vintage normalized plate of TC 128B steel [11].

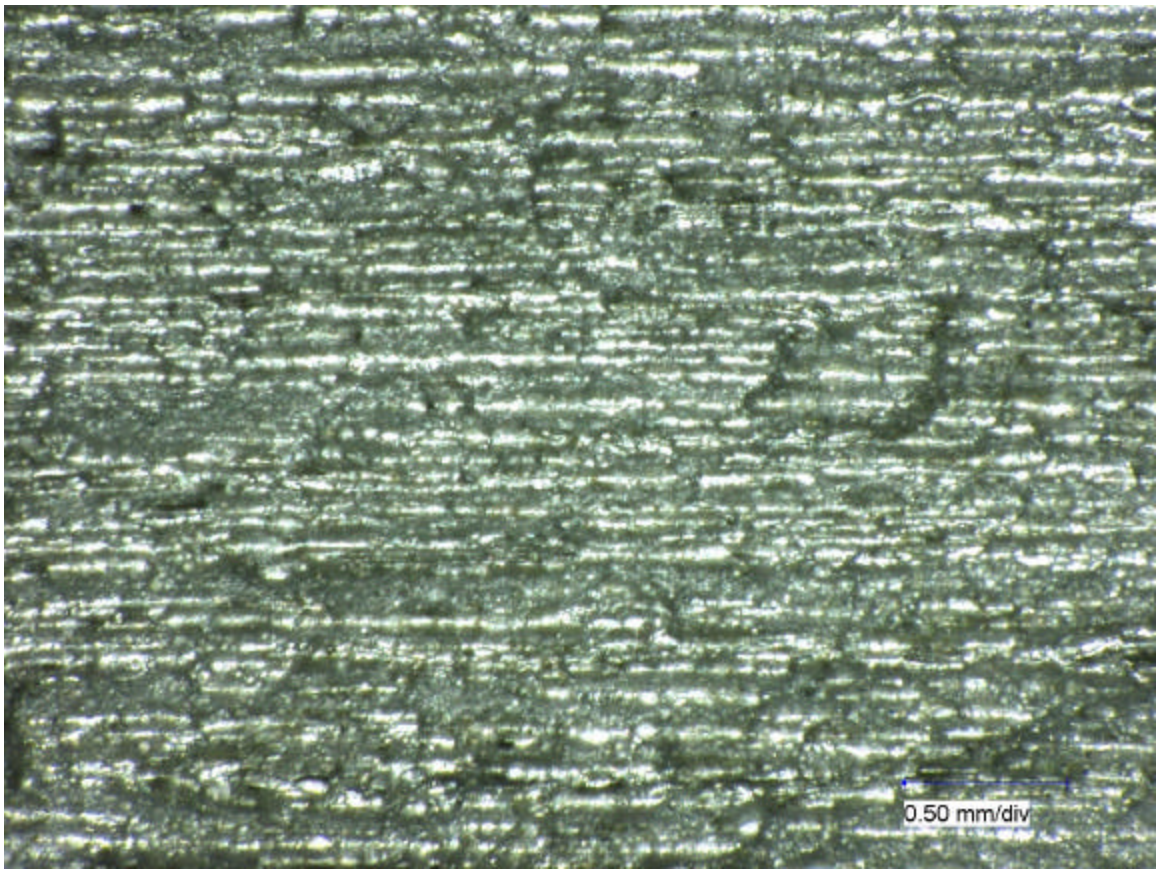

FIGURE 2.17 Fracture surface from a high-rate toughness test on the shell steel from Minot Car 22 (Fig. 2.15), tested at 37°F [11]. The shiny areas correspond to troughs that formerly contained sulfide stringers.

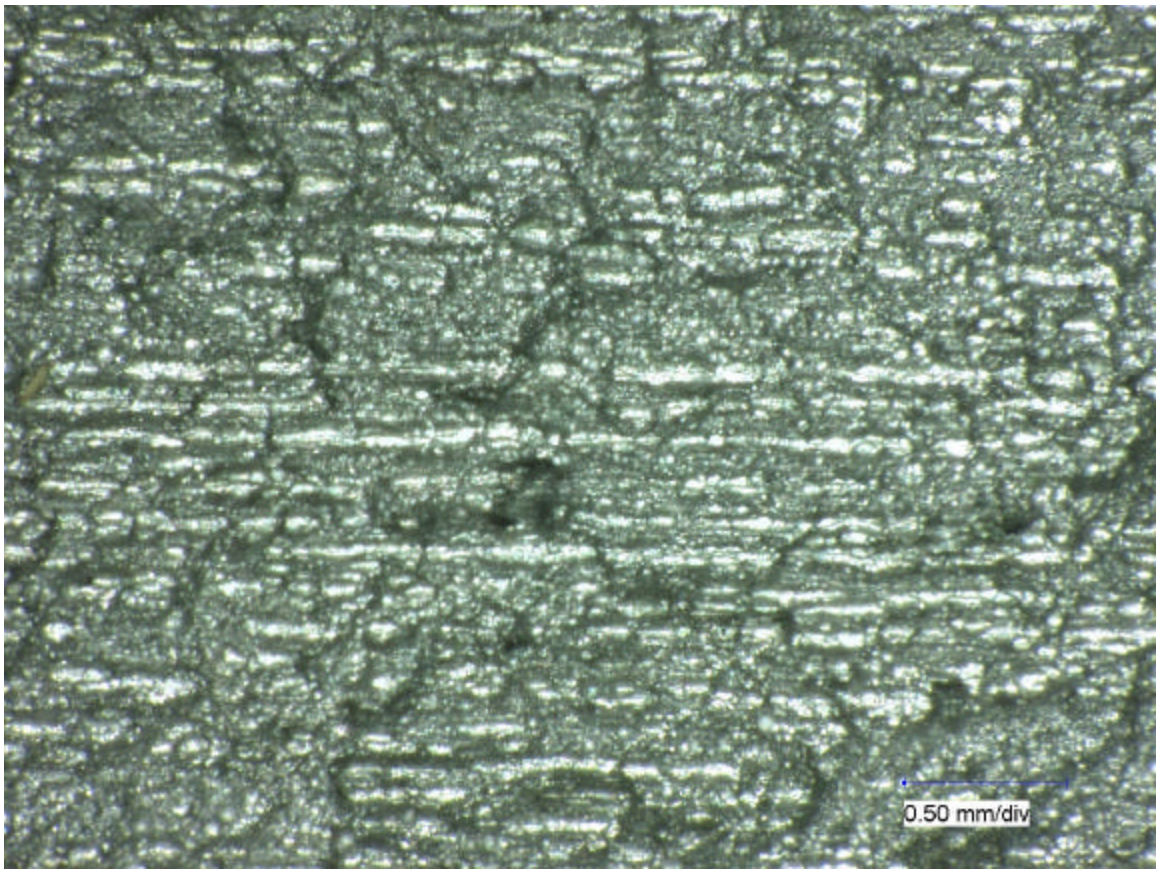

FIGURE 2.18 Fracture surface from a high-rate toughness test on a modern normalized TC 128B plate (Fig. 2.16), tested at ambient temperature [11]. Although the sulfur content is lower than in the 1970s vintage steel from Minot Car 22, numerous sulfide stringers are evident. Currently, the TC 128 B specification does not require sulfide shape control.

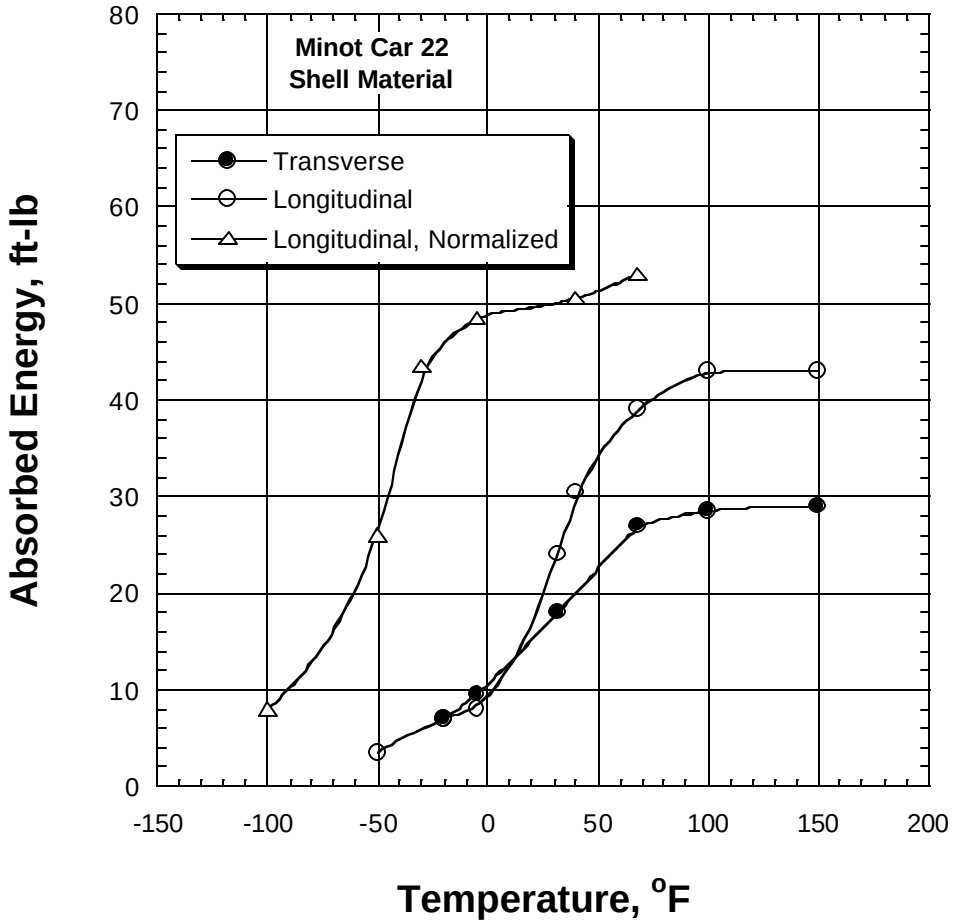

FIGURE 2.19 Effect of specimen orientation and normalization on impact toughness in a 1970s vintage TC 128B steel from an ammonia tank car that derailed near Minot, ND [1].

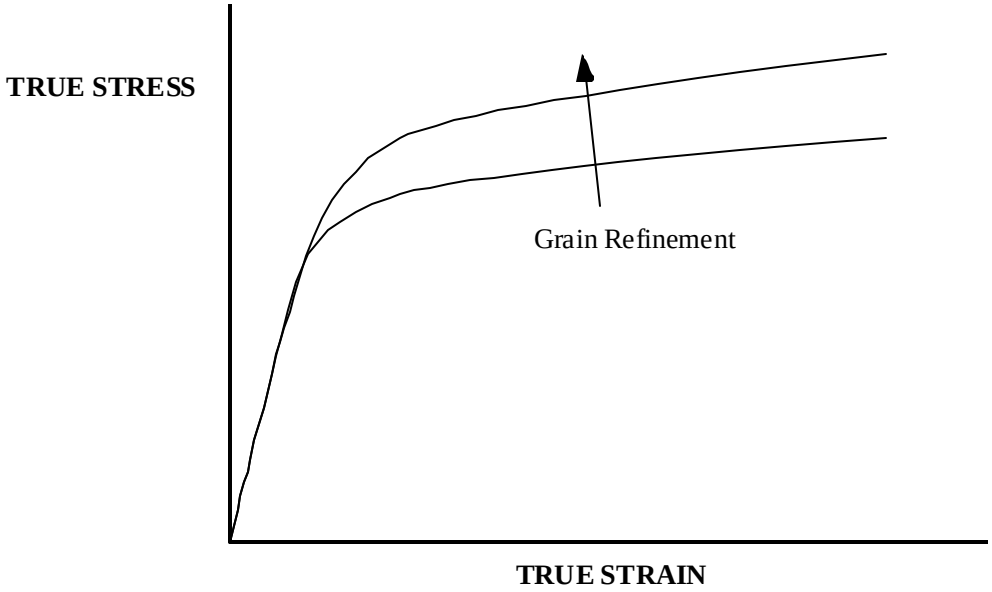

FIGURE 2.20 Strengthening due to grain refinement, which can also improve upper shelf toughness.

2.3 Steels for Improved Tank Car Performance

Given the desire of the rail industry to reduce the frequency of lading loss resulting from accidents, it is useful to consider which material properties are most important in reducing lading loss through head and shell failures. This then leads to a discussion of possible replacements for the current TC 128B steel specification in future tank car construction.

Figure 2.21 is a schematic plot of the energy required to puncture or fracture a steel plate as a function of temperature. The fracture energy is substantially reduced when there is a pre-existing notch-like feature. Moreover, the fracture mode transitions from ductile to brittle at much lower temperatures for the unnotched case. Therefore, failure in unnotched steel plates is initiated through ductile puncture over a wide temperature range, including temperatures where notched plates exhibit lower-shelf behavior.

The effect of a pre-existing notch on fracture behavior is demonstrated in Figs. 2.22 and 2.23. During the Minot investigation conducted by the authors, Charpy testing was performed on exemplar steels taken from two retired tank cars that were built in 1967 and 1971 [11]. Standard CVN specimens tested at -36°F absorbed energies ranging from 3 to 6 ft-lb, and all fracture surfaces were 100% brittle. Figure 2.22 is a photograph of the broken specimens. Figure 2.23 is a photograph of two unnotched specimens impact tested at -36°F in a Charpy machine with a 300-ft-lb capacity. Both specimens bent but did not break, which indicates that the fracture energy for the unnotched specimens is at least two orders of magnitude higher than for notched specimens at this temperature. These specimens absorbed a significant amount of energy without fracturing, despite being at a temperature that is on the lower shelf of the CVN toughness curve.

When a tank car is subject to an impact load during a rail accident, the head and shell are analogous to the unnotched condition in Figs. 2.21 and 2.23, aside from the rare instances where the impact occurs at a significant pre-existing weld flaw. In the absence of a pre-existing notch, a puncture must form at a smooth surface. This requires a substantial amount of energy concentrated over a small area. Moreover, the puncture will form by ductile rupture (microvoid coalescence) unless the steel is at a *very* low temperature (i.e., cryogenic conditions well below ambient temperatures in Antarctica).

Once a ductile puncture forms, one or more cracks may emanate from the puncture if sufficient kinetic energy remains from the impact event. Such a crack may be ductile or brittle, depending on the metal temperature relative to its transition region (in the presence of a notch or crack). Figures 2.24 and 2.25 are photographs of a puncture and subsequent brittle crack propagation that occurred in an anhydrous ammonia tank car as a result of the Minot derailment. Figure 2.26 is a photograph of another anhydrous ammonia car that was taken at the site of the Minot derailment. In this case, a 360-degree shell fracture initiated from a puncture. Figure 2.14 is a photograph of the fracture surface of the car in shown Fig. 2.26. Recall from the previous section that this failure propagated as a low-energy ductile fracture. The woody appearance of the fracture surface is due to a significant number of sulfide stringers.

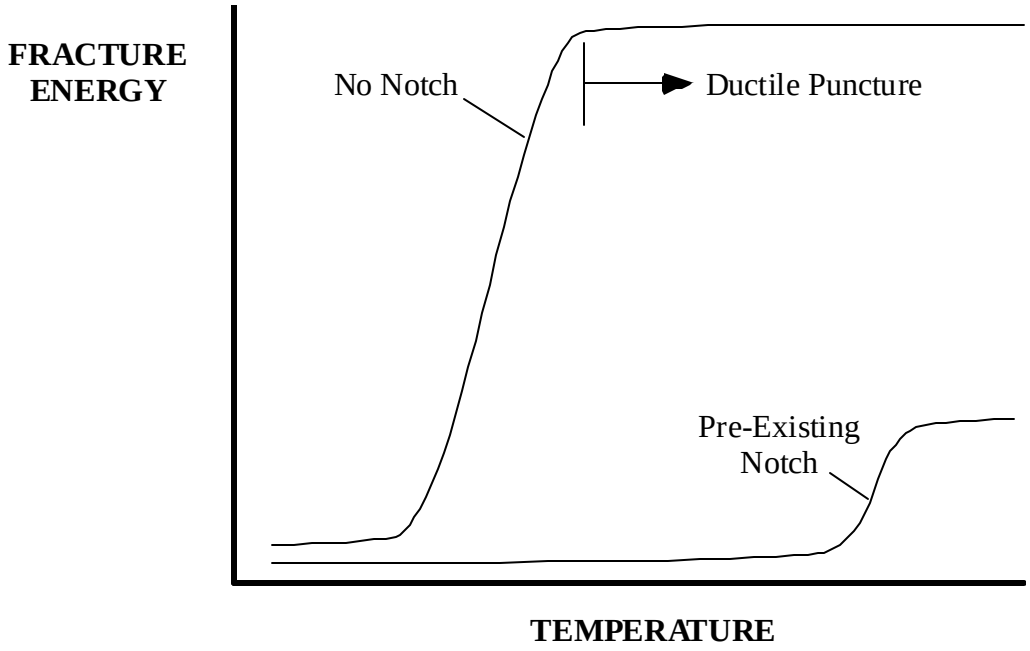

FIGURE 2.21 Effect of a pre-existing notch on fracture energy.

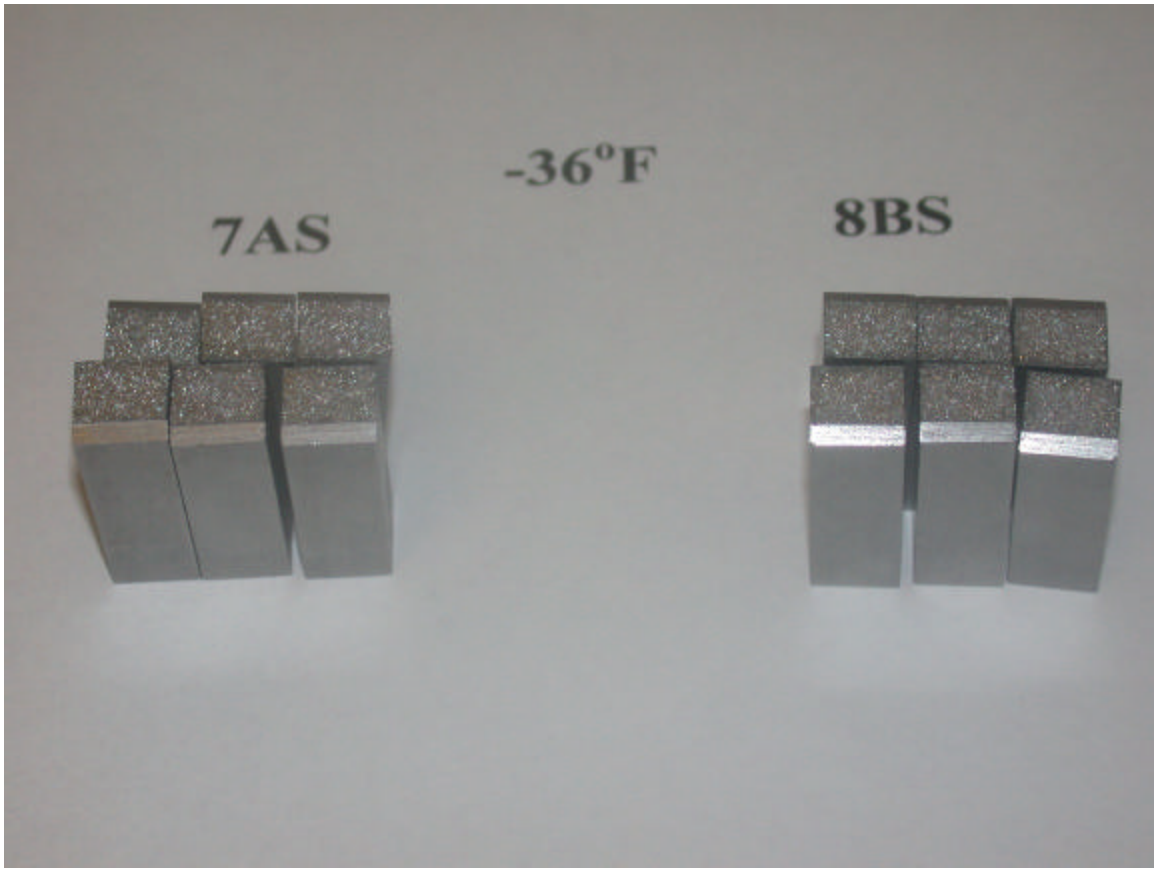

FIGURE 2.22 Charpy specimens tested at -36°F, where the fracture is 100% brittle. Coupons 7AS and 8BS were taken from retired tank cars built in 1967 and 1971, respectively.

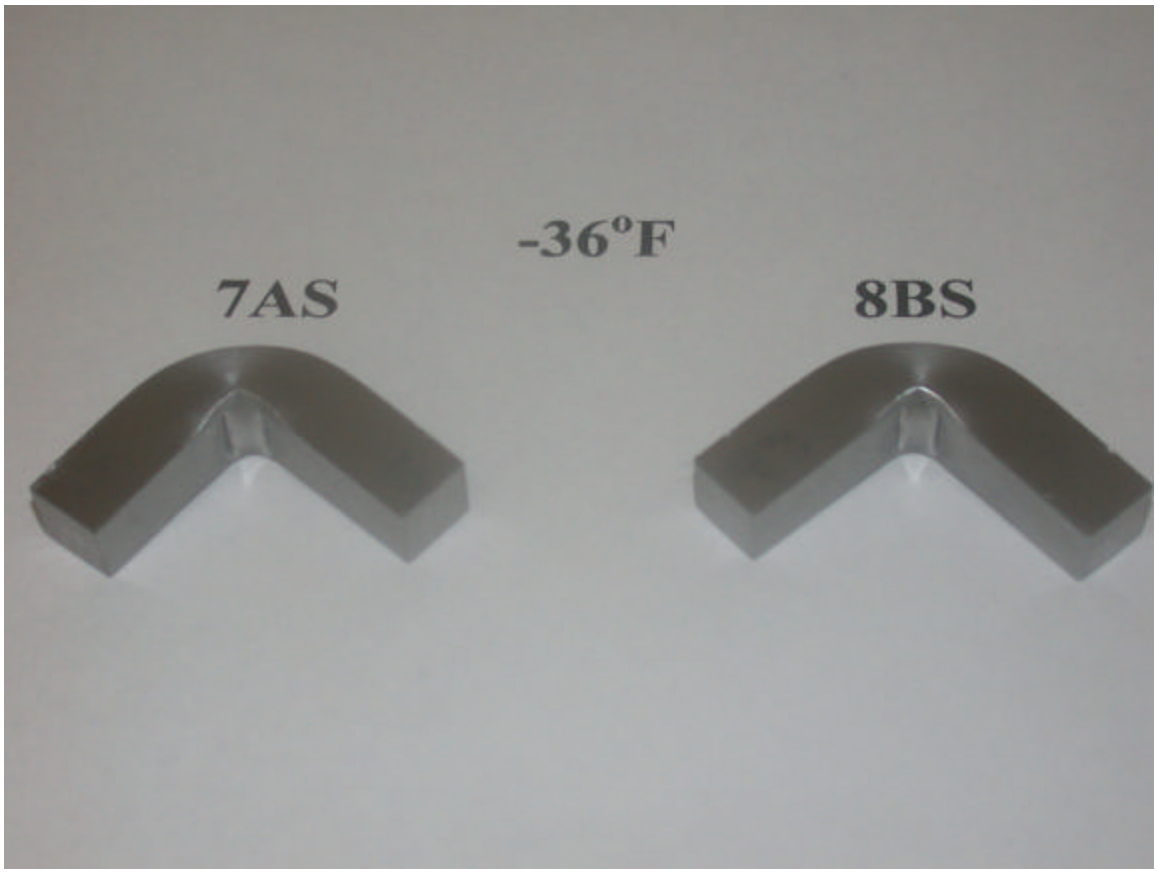

FIGURE 2.23 Unnotched Charpy specimens for Coupons 7AS and 8BS tested at -36°F. The Charpy test machine has a 300 ft-lb capacity.

FIGURE 2.24 Puncture and brittle fracture in an anhydrous ammonia tank car that derailed near Minot, ND [1].

FIGURE 2.25 Close-up of the puncture in Fig. 2.24.

FIGURE 2.26 Puncture and 360-degree shell fracture in an anhydrous ammonia car, which derailed near Minot, ND. Crack propagation from the puncture was by a low-energy ductile fracture mechanism (Fig. 2.14).

Over the past 30 years, nearly all research and discussion about improving the toughness of tank car steels has focused on brittle fracture resistance [7-10]. The 1989 requirement to construct tank car shells from normalized TC 128B plate was intended to reduce or eliminate brittle fracture during accidents. Studies of modern microalloying steels as possible replacements to TC 128B have largely been motivated by the superior low-temperature toughness properties that can, in theory, be achieved in these materials.

We contend that the preoccupation with brittle fracture avoidance has not resulted in the most prudent use of time and resources. Our reasoning is as follows:

- Two separate studies of past accident data [4, 5] indicated that brittle fracture comprises a small fraction of total lading loss incidents. Moreover, these studies concluded that preventing brittle fracture would have a very small effect on the overall probability of lading loss because in most cases where brittle fracture occurs, derailment forces were sufficient to cause ductile failure.

- In order for brittle fracture to occur in a tank car, it must initiate from a notch-like feature. Aside from the rare cases where there is a significant pre-existing flaw at

the impact location, brittle fracture must be preceded by ductile puncture. Prevention of brittle fracture is, at best, a second line of defense. Preventing the puncture that initiated brittle failure would seem to be a more sensible goal.

- The 1989 requirement to use normalized TC 128 B steel tank car shells has largely eliminated the risk of brittle fracture in tank cars built since this requirement went into effect. Therefore, pursuing even better low temperature properties that are potentially available in microalloyed steels does not appear to make sense. If improved low-temperature toughness is the only reason for considering microalloyed steels, then this is an option with a high cost and virtually no benefit.

That is not to say that modern microalloyed steels should not be considered for use in future tank car construction, but the low-temperature toughness properties should not be the primary motivation. The real potential benefit in certain modern grades of steel lies in their superior upper shelf toughness, which is achieved largely through desulfurization and sulfide shape control.

Given that making tank cars more puncture resistant is a desirable goal, improved steel properties must play a crucial role in achieving that goal. Design modifications such as increased wall thickness can be beneficial (Chapter 3), but are not sufficient to prevent major releases such as occurred at Minot and Graniteville. Another suggested remedy entails accelerating the retirement of pre-1989 tank cars and replacing them with normalized TC 128B steel cars. Normalization does not affect the resistance to ductile puncture, so such a massive capital investment would produce a minimal benefit. Moreover, an accelerated replacement program using current steel specifications would result in a missed opportunity. If a large number of TC 128B cars are built in the next few years, these new cars will not be replaced for a long time. When and if the industry decides that improved steel properties are beneficial, they will be not be in a position to take advantage of new steels if they have already spent substantial sums to replace the pre-1989 fleet with cars made from TC 128B.

There are two options for improving the properties of steel for tank car construction:

1. Modify the TC 128B or other C-Mn steel specification to reduce the maximum allowable sulfur content and require sulfide shape control.
2. Adopt a microalloyed steel with superior upper shelf toughness as well as acceptable formability and weldability.

The first option is worth considering. Conventional carbon-manganese steels are capable of very high upper shelf toughness (> 200 ft-lb CVN) when sulfur levels are very low and sulfide shape control is part of the melting practice [12]. Desulfurization through the addition of calcium compounds is commonplace in the steel industry. Sulfur levels have declined over the years despite the fact that many steel specifications still allow relatively high amounts. For example, the A 516-70 specification currently allows 0.035%. Sulfur contents of 0.008% or lower are readily attainable with current melting practices. Sulfide shape control must also be applied along with desulfurization in order to obtain the

maximum benefit in upper shelf toughness, and hence puncture resistance. The current TC 128B specification limits sulfur to 0.015%, but this limit could be reduced to 0.010% or below. Apparently, Mittal steel currently manufactures TC 128 B steel with sulfide shape control [13], but it is not part of the AAR requirement. Further work is necessary to quantify the upper shelf toughness levels that are achievable in TC 128B steel, both with the current specification and the proposed refinements.

An ongoing project at Southwest Research Institute [14] is evaluating the properties of various generations of tank car steels. Figure 2.27 is a plot of transverse Charpy energy at +50°F as a function of sulfur content. There is considerable scatter, and a well-defined trend in the data is not readily apparent. However, the data for pre-1989 shells correspond to steels that have not been normalized, so the Charpy energies do not necessarily reflect upper shelf behavior. Figure 2.28 is a re-plot of the data with these points removed. The trend of increasing upper shelf toughness with decreasing sulfur content is much clearer, although there is still significant scatter. Two data points for pre-1989 heads have Charpy energies below 25 ft-lb, so these materials are probably not on the upper shelf at +50°F. Much of the scatter in upper-shelf transverse toughness is likely caused by variability in the sulfide stringer shape. Sulfide shape control should reduce this scatter and improve the toughness in the transverse orientation.

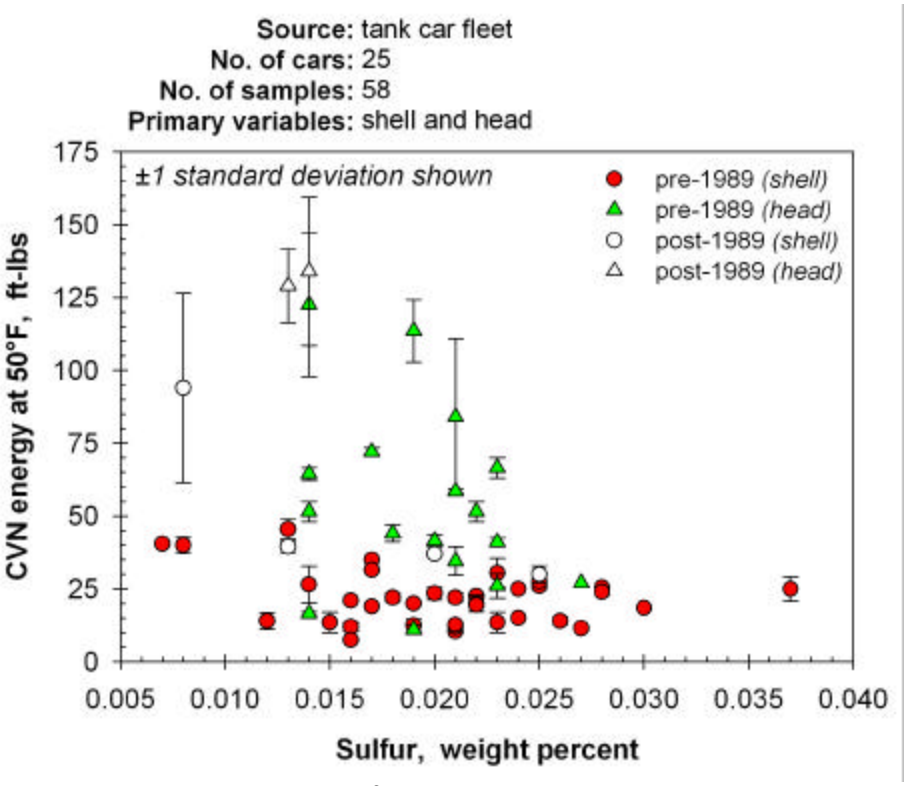

FIGURE 2.27 Charpy energy at +50°F versus sulfur content for tank car steels [14].

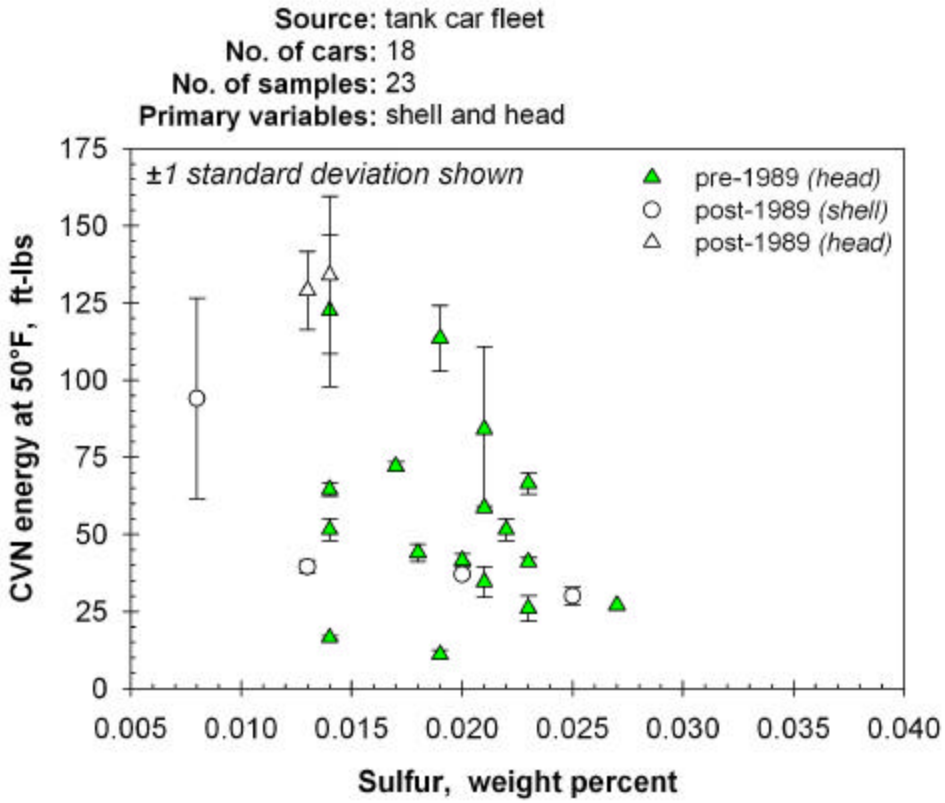

FIGURE 2.28 Same as Fig. 2.27 but with data points removed for non-normalized shell material [14].

Before discussing the merits of modern microalloying steels (Option 2 above), a brief overview of these material might be beneficial to the reader. Microalloyed steels, also known as high strength low alloy (HSLA) steels, have small additions of alloying elements such as columbium, vanadium, and titanium. These steels achieve high strength and toughness through a very fine grain structure. The microalloying elements form carbide and nitride precipitates, which provide additional strengthening. Some HSLA steels are manufactured with a thermomechanical controlled process (TMCP), which entails controlled rolling and accelerated cooling. The finishing temperature for rolling is in the austenitic range, but below the recrystallization temperature for austenite. Upon accelerated cooling, a very fine ferritic structure forms on deformed austenite grains. Some HSLA steels are normalized rather than manufactured with the TMCP method.

The AAR previously commissioned a two-part study of HSLA steels for possible tank car use. The reports of the Phase I and Phase II programs were issued in 1987 and 1991, respectively [9, 10]. A proposed steel specification, TC-135, was developed during Phase I. Although the test results on HSLA steels were largely encouraging, two problems were identified in the AAR research. First, the good toughness properties produced as a result of controlled rolling are lost when the material is heated to a hot-forming temperature. Second, the weldability of the HSLA steels considered was not as good as hoped. Both of these difficulties have been addressed in recent years [15]. Good formability can be

achieved in normalized HSLA plates, and the weldability of HSLA steels has improved due to lower carbon content and other factors.

Table 2.1 lists the existing ASTM standards for HSLA steel plate. The proposed AAR TC-135 specification is also shown for comparison. Since upper shelf toughness is the key factor in puncture resistance, the steel grades that allow up to 0.035% sulfur (A 633, A 656, and A 737) are not ideal for future tank car construction. The only ASTM specifications in Table 2.1 that include low sulfur limits are A 841 and A 945. The former is not suitable for hot-formed heads because it is exclusively produced by the TMCP method. Paragraph 1.3 of A 841 limits forming and post-weld heat treatments to 1200°F because higher temperatures adversely affect the toughness and microstructure of TMCP steels. The A 841 specification could, however, be considered for tank car shells and cold-formed heads. The A 945 specification allows plate to be produced by the TMCP method, but it is not a requirement. The title of A 945, "Standard Specification for High-Strength Low-Alloy Structural Steel Plate with Low Carbon and Restricted Sulfur for Improved Weldability, Formability, and Toughness", indicates that is it is the best choice for hot-formed tank car heads among the available ASTM grades of microalloyed HSLA steel. Referring to Table 2.1, the chemical and tensile specifications of A 945 are similar to TC 135, but the former undoubtedly incorporates improvements in HSLA steelmaking technology that have occurred since 1991. Sulfide shape control is not specifically required by A 945, but it is routinely applied in the manufacture of this alloy. If an AAR specification equivalent to A 945 were developed, it should include an explicit requirement for sulfide shape control.

It remains to be seen whether Option 2 (microalloyed steel) is better than Option 1 (conventional normalized C-Mn steel with low sulfur and sulfide shape control) on a cost/benefit basis. A testing program and cost analysis is recommended to assess the relative merits of Options 1 and 2.

TABLE 2.1
Summary of chemical and strength requirements for HSLA steels.

Specification	Grade	% Carbon	% Manganese	% Sulfur	Yield Strength, ksi	Tensile Strength, ksi
A 633 – 01	A	0.18 max	1.00 – 1.35	0.035 max	42 min	63 – 83
	C	0.20 max	1.15 – 1.50	0.035 max	50 min	70 – 90
	D	0.20 max	0.70 – 1.35	0.035 max	50 min	70 – 90
	E	0.22 max	1.15 – 1.50	0.035 max	60 min	80 – 100
A 656 – 03	50	0.18 max	1.65 max	0.035 max	50 min	60 min
	60	0.18 max	1.65 max	0.035 max	60 min	70 min
	70	0.18 max	1.65 max	0.035 max	70 min	80 min
	80	0.18 max	1.65 max	0.035 max	80 min	90 min
A 737 – 99 (Reapproved 04)	B	0.22 max	1.07 – 1.62	0.035 max	50 min	70 – 90
	C	0.22 max	1.07 – 1.62	0.035 max	60 min	80 – 100
A 841 – 03a	A	0.20 max	0.70 – 1.35	0.030 max	50 min (Class 1) 60 min (Class 2)	70 – 90 (Class 1) 80 – 100 (Class 2)
	B	0.15 max	0.70 – 1.35	0.030 max		
	C	0.10 max	0.70 – 1.60	0.030 max		
	D	0.09 max	1.00 – 2.00	0.010 max	100 min (Class 3)	145-170 (Class 3)
	E	0.07 max	0.70 – 1.60	0.015 max	70 min (Class 4) 75 min (Class 5)	84 – 104 (Class 4) 88 – 108 (Class 5)
	F	0.10 max	1.10 – 1.70	0.020 max	70 min (Class 6) 75 min (Class 7) 80 min (Class 8)	82 – 102 (Class 6) 86 – 106 (Class 7) 90 – 110 (Class 8)
A 945 – 00	50	0.10 max	1.10 – 1.65	0.010 max	50 min	70 min
	65	0.10 max	1.10 – 1.65	0.010 max	65 min	78 min
TC 135	A	0.12 max	1.00 – 1.75	0.010 max	50 min	70 – 90
	B	0.16 max	1.00 – 1.75	0.010 max	60 min	81 – 100
	C	0.22 max	1.00 – 1.60	0.010 max	60 min	81 – 100

3 EFFECT OF TANK CAR DESIGN ON PUNCTURE RESISTANCE

3.1 Inferring Trends from Prior Accident Data

An extensive database of prior rail accidents and resulting lading loss, created and maintained by the RSI-AAR Railroad Tank Car Safety Research and Test Project, has been used in a number of projects over the years. This database has made it possible to correlate lading loss incidents with tank car design attributes such as wall thickness. Figure 3.1 was taken from a 1998 RPI-AAR report [5] in which a Monte Carlo probabilistic fracture model was calibrated to the accident data. There is a clear trend between the probability of lading loss through the head or shell and section thickness. Figure 3.1 has considerable scatter because the data points reflect raw data, where sample size is limited for a given thickness. Another limitation of this plot is that the "equivalent thickness" plotted on the horizontal axis corresponds to the combined thickness when a jacket or head shield is present. For example, a jacketed ½" shell is given an effective thickness of $^{5}/_{8}$" to account for a nominally $^{1}/_{8}$" jacket. When head shields were present, 0.5" was added to the head thickness. Any potential differences in the rupture behavior between two plates of a given combined thickness and a solid plate of that same thickness cannot be inferred from Fig. 3.1.

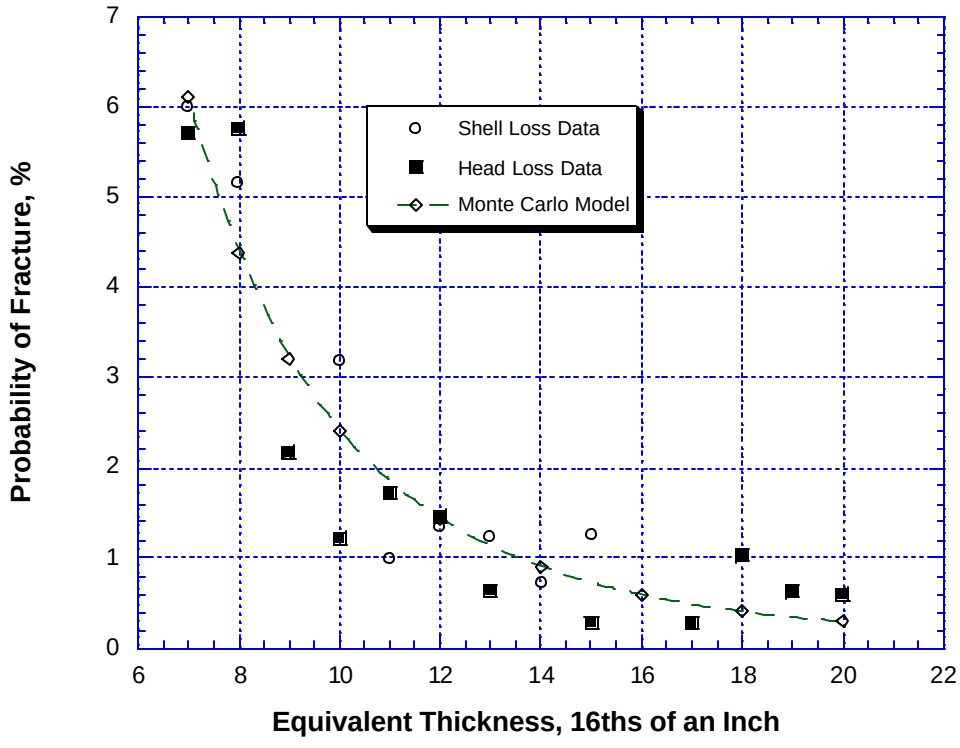

FIGURE 3.1 Results of an earlier study, where a Monte Carlo fracture model was calibrated to the accident database. RPI-AAR Report RA-03-6-62 [5].

A recent RSI-AAR study [16] took a more systematic look at tank car design parameters that affect lading loss probability. Statisticians from the University of Illinois performed multi-variable regression analysis on the accident data. This analysis had the effect of smoothing the data so that trends could be more readily discerned. The analysis separated the data into multiple populations, including:

- Head versus shell loss.
- Jacketed versus non-jacketed cars.
- Cars with and without head shields.

The investigators did, however, lump pressure and non-pressure cars into a single population for head and shell loss probability because they could not detect a statistically significant difference between the two car types at a given wall thickness. They adjusted the lading loss probability values downward to account for unreported accidents. The number of unreported accidents is, by definition, unknown, so the adjusted probability values in the AAR study are subject to uncertainty and error. However, the predicted *relative* trends of lading loss probability with section thickness and other variables should be reliable.

The results of the regression analysis are presented in tabular form in Ref. [16]. Figures 3.2 to 3.4 show several plots created by the present authors that were generated from this tabular data.

Figure 3.2 is a plot of head and shell lading loss probability versus thickness for non-jacked cars without head shields. Note that the lading loss probability through the shell is much more sensitive to thickness than the head loss probability.

Figure 3.3 compares the lading loss through the shell for jacketed and non-jacketed cars. In the former case, the jacket and shell thickness were added to obtain the combined thickness. The data are plotted in this manner in order to isolate the effect of the standoff between the jacket and shell. This plot indicates that a jacketed shell performs slightly better than a non-jacketed shell with the same total thickness. For example, a jacketed ½" shell, which has a combined thickness of approximately $^{5}/_{8}$", performs slightly better in an accident than a non-jacketed shell that is $^{5}/_{8}$" thick. Of course, a jacketed ½" shell performs significantly better than a non-jacketed ½" shell, with the benefit coming from a combination of the additional section thickness provided by the jacket as well as the standoff between the jacket and shell.

Figure 3.4 shows the relative effect of a jacket or head shield on the probability of lading loss through the head. As is the case in Fig. 3.3, the lading loss probability is plotted in terms of combined thickness. In a non-jacketed car, where the head shield is flush against the head, the performance for a given combined thickness is slightly better than a head with the same total thickness. That is, a laminated 2-piece head configuration performs slightly better than a 1-piece head with the same total thickness. In a jacketed car, however, the performance is far superior to a non-jacketed car. When there is a standoff

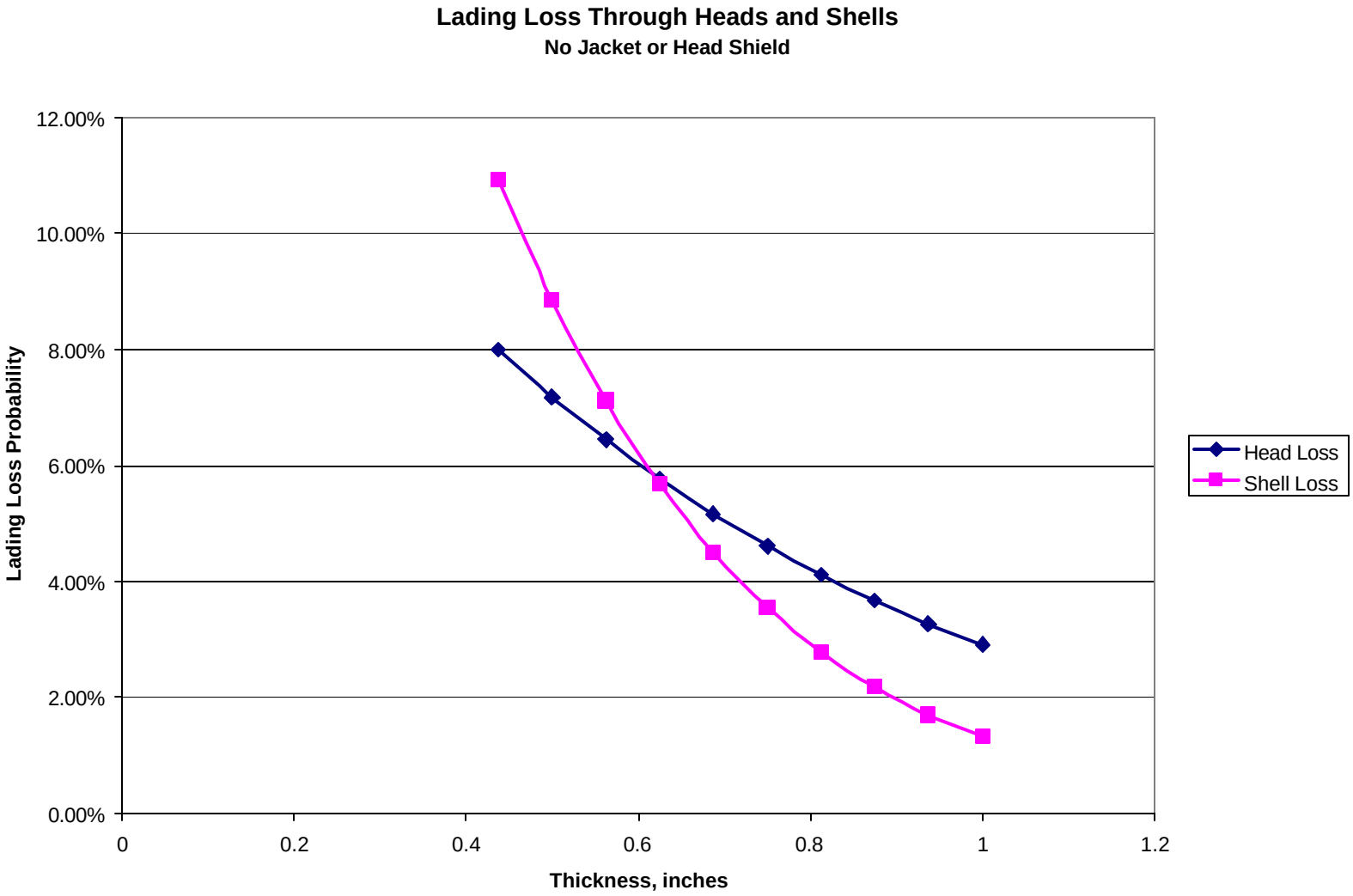

FIGURE 3.2 Lading loss probability curves obtained from tabular results in RSI-AAR Report RA-05-02 [16].

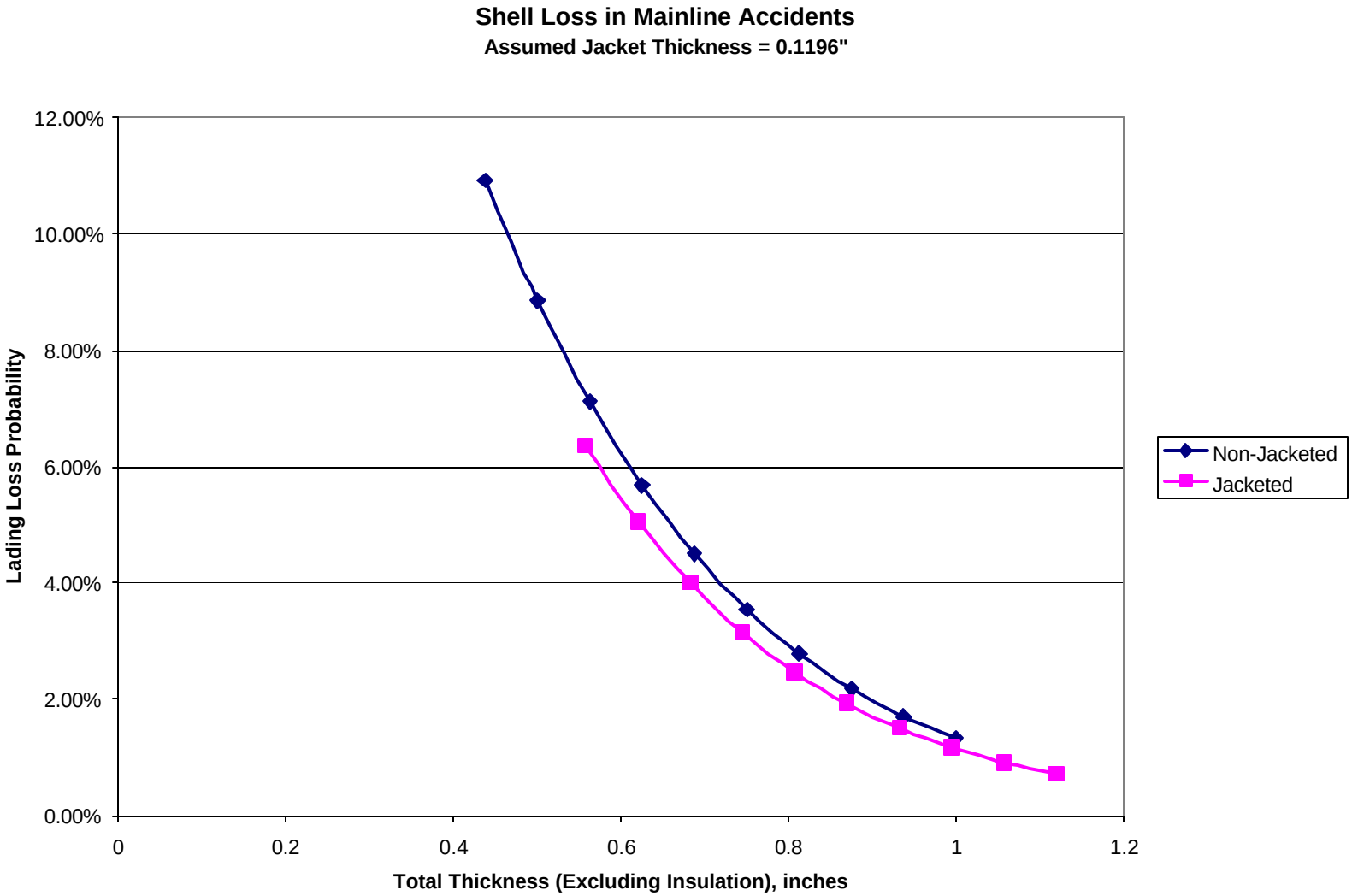

FIGURE 3.3 Effect of a jacket on lading loss through the shell. Data taken from RSI-AAR Report RA-05-02 [16].

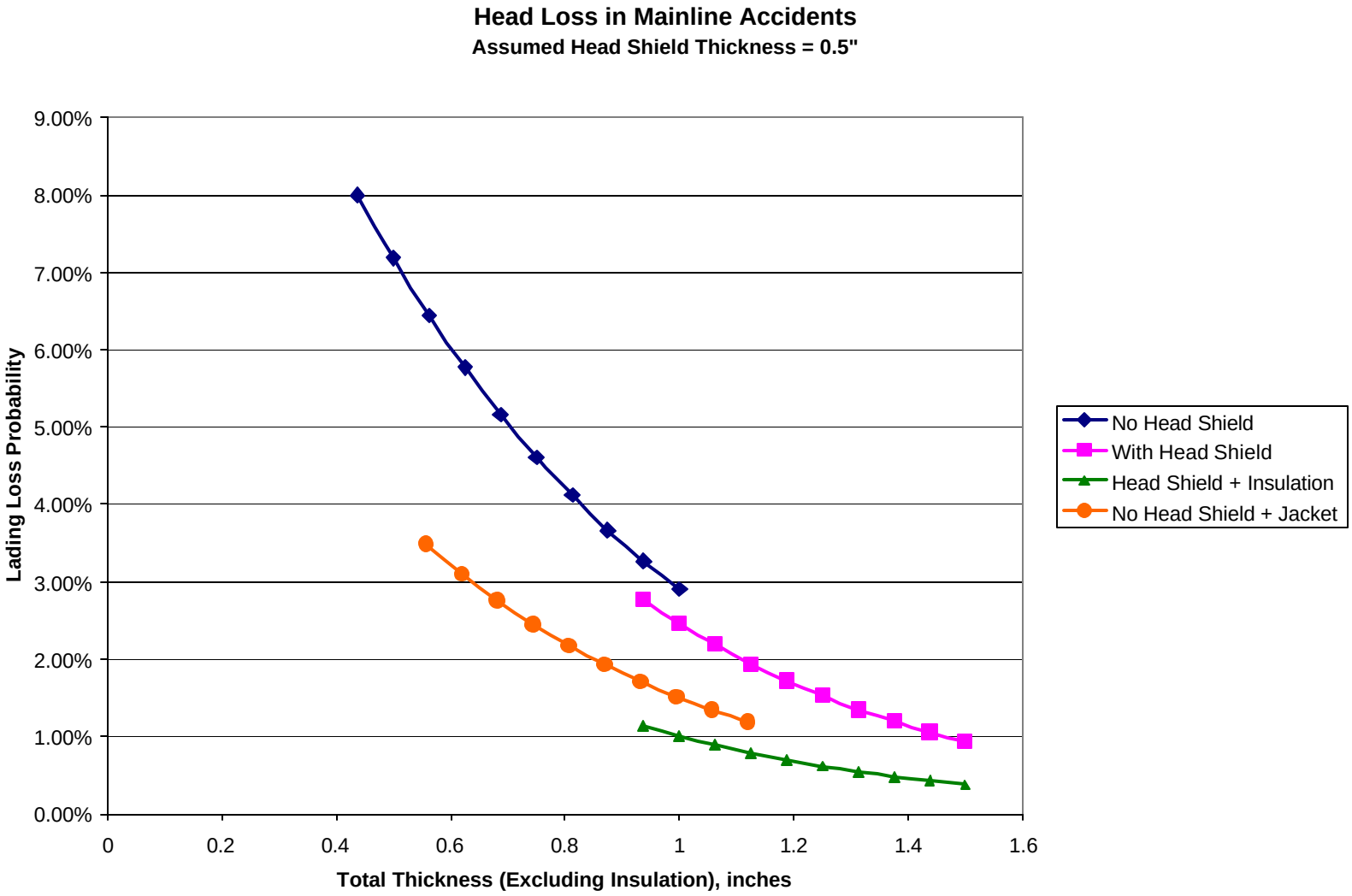

FIGURE 3.4 Effect of head shields and jackets on lading loss through heads. Data taken from RSI-AAR Report RA-05-02 [16].

between either a head shield or jacket and the head, the lading loss probability at a given combined thickness is significantly lower than for a solid head with the same total thickness. Note that although half-height head shields are included in the regression analysis in RSI-AAR Report RA-05-02 [16], they are not considered in the present study.

Clearly, the behavior of heads and shells in accidents are significantly different from one another. This behavior is explored further below.

3.2 Development of a Predictive Model

What follows is the presentation of a simple model that is intended to explain the trends in Figs. 3.2 to 3.4, as well as predict the effect of possible changes to the design and/or material properties.

Every rail accident is unique. A major derailment may result in multiple collisions, each of which is itself unique and highly complex. Let us assume that the complexities of a collision event can be captured with a single driving force parameter, which we will call *puncture intensity*:

$$\text{Puncture Intensity } (I) = \text{ Impact Energy } \times f\left(G_1, G_2, G_3, \cdots\right) \tag{3.1}$$

where G_i are geometry factors, which could include the size and shape of the object that collides with the tank car, as well as the location and angle of the collision. Developing a detailed mathematical description of the function $f(G_i)$ is beyond the scope of this project, and may be not be feasible in any case. It is sufficient for our purposes to assume that I scales with the available impact energy.

Let us now define a *puncture resistance index*, I_R, which is a function of section thickness and material properties. Puncture will occur when the driving force exceeds the material resistance. That is,

$$I \geq I_R \tag{3.2}$$

The absolute values of I and I_R are arbitrary, so we can set $I_R = 1$ for a $^7/_{16}$" shell made from traditional tank car steel. Assuming the puncture resistance index exhibits a power-law dependence on shell thickness results in the following expression:

$$I_R = \left(\frac{t}{0.4375} \right)^n \tag{3.3}$$

Now suppose that we decide to increase the shell thickness by Δt. The new puncture resistance index is given by

$$I_R = \left(\frac{t + \Delta t}{0.4375} \right)^n \tag{3.4}$$

assuming the power-law dependence in Eq. (3.3). On the other hand, suppose that instead of increasing the shell thickness, we add a jacket of thickness Δt. If there is a significant standoff between the jacket and shell, they should each respond to the impact event independently[1], so the respective puncture resistance values would be additive:

$$I_R = \left(\frac{t}{0.4375} \right)^n + \left(\frac{\Delta t}{0.4375} \right)^n \tag{3.5}$$

For the special case of $n = 1$, both of the above examples will result in the same puncture resistance. The physical significance of an exponent of unity is that the puncture energy of the shell plate scales linearly with thickness. If this were the case, there would be no net benefit of a jacket relative to a increasing the shell thickness by the amount of the jacket thickness. In reality, there is a modest benefit to the standoff between the jacket and shell, as Fig. 3.3 illustrates. Therefore, n must be slightly less than 1 for the shell.

The effect of the jacket on puncture resistance can be predicted from Eq. (3.5) if n is known. However, in order to translate puncture resistance into lading loss probability (Fig. 3.3), a statistical distribution function for the puncture intensity is needed.

The lading loss probabilities for the shell can be used to infer a statistical distribution of the puncture intensity in past mainline accidents. For example, the probability of lading loss through the shell is approximately 11% for $^7/_{16}$" wall thickness, where $I_R = 1$. In order for puncture to occur, I must reach or exceed I_R. Therefore, an impact event where $I = 1$ is in the 89th percentile, meaning that $I \leq 1$ in 89% of accidents. For shell thicknesses greater than $^7/_{16}$", I_R was computed from Eq.(3.3) assuming $n = 0.95$. This exponent was arrived at through trial and error. The cumulative probability of the I values corresponding to the various shell thicknesses were determined in the same manner as the $^7/_{16}$" case. The results of this exercise are listed in Table 3.1

The data in Table 3.1 were fit to a Weibull distribution:

$$F = 1 - \exp\left\{ -\left[\left(\frac{I}{q} \right)^b \right] \right\} \tag{3.6}$$

where F is the cumulative probability, and b & q are fitting constants. For the purpose of curve fitting, Eq. (3.6) can be linearized:

[1] That is, if the jacket and shell do not interact with one another during impact, the total puncture resistance is equal to the sum of the respective puncture resistances of the two plates. For example, if a projectile is fired at a pair of parallel plates of equal thickness, where there is significant gap between the plates, the energy required to penetrate both plates would be twice the energy necessary to penetrate a single plate.

TABLE 3.1
Puncture resistance and lading loss probability as a function of shell thickness. The puncture resistance index was computed from Eq. (3.3) assuming $n = 0.95$.

Shell Thickness, inches	Puncture Resistance Index (I_R)	Lading Loss Probability	Cumulative Probability on I
0.4375	1.000	10.92%	89.08%
0.5	1.135	8.86%	91.14%
0.5625	1.270	7.12%	92.88%
0.625	1.403	5.68%	94.32%
0.6875	1.536	4.50%	95.50%
0.75	1.669	3.55%	96.45%
0.8125	1.801	2.79%	97.21%
0.875	1.932	2.18%	97.82%
0.9375	2.063	1.70%	98.30%
1	2.193	1.33%	98.67%

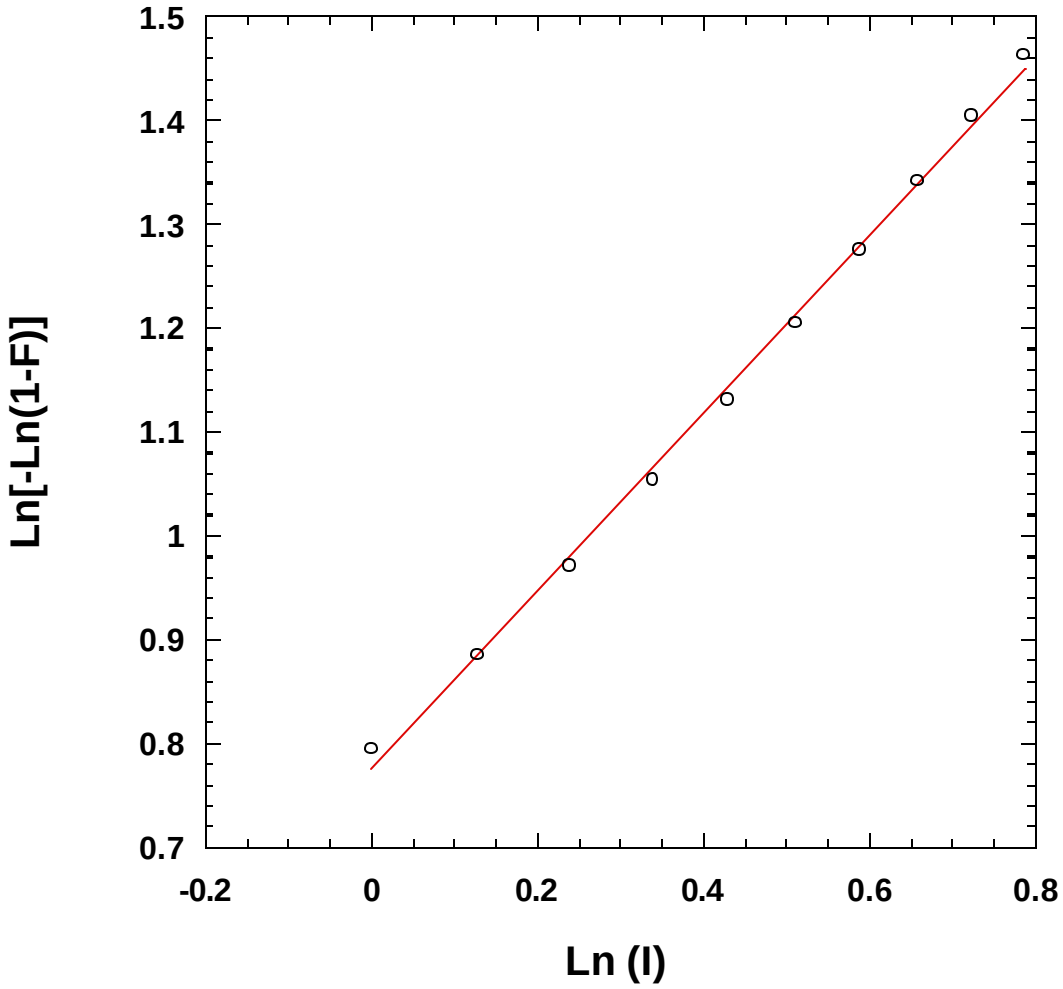

FIGURE 3.5 Weibull fit of the puncture intensity at tank car shells for mainline accidents.

$$\ln\left[-\ln\left(1-F\right)\right] = b\,\ln\left(I\right) - b\,\ln\left(q\right) \tag{3.7}$$

Figure 3.5 shows the fit of the data in Table 3.1 to Eq. (3.7). The data points follow a linear trend, which indicates that the Weibull distribution provides a good fit. The following constants were obtained from the curve fit:

$\beta = 0.858$

$q = 0.405$

In order to compute the lading loss probability for a jacketed shell, the combined puncture resistance index as a function of shell thickness was inferred from Eq. (3.5). These I_R values were substituted into Eq. (3.6) to obtain the cumulative probability of the puncture intensity, F. Note that the probability of lading loss = $1 - F$.

Figure 3.6 compares the predicted and actual lading loss probabilities for jacketed shells. Note the value of n was chosen such that the prediction would match the curve inferred from the regression analysis of accident data.

The behavior of tank car heads during accidents is clearly different than for shells, as Figs. 3.2 and 3.4 illustrate. Heads and shells exhibit a different thickness dependence, and the relative benefits of a jacket are much greater for a head than for a shell. Given the simple model for the shell outlined above, there are two ways to handle the head:

1. Assume the same thickness dependence for I_R in both the head and shell, and infer the puncture intensity distribution for the head.
2. Assume the same puncture intensity distribution for the head and shell and infer I_R versus thickness for the head.

The first approach is not consistent with the observed trends. For example, the behavior of jacketed heads cannot be explained in terms of a different distribution of puncture intensity. Heads and shells definitely exhibit different relationships between puncture resistance and thickness. Some might quibble with the assumption that heads and shells are subject to identical populations of impact events, but we believe that this assumption is a reasonable approximation of reality. Overall, the rate of head and shell punctures are comparable in cars that do not have head shields. If there was a systematic difference between impact events for heads and shells, we would expect to see significantly more losses in one than the other.

Figure 3.7 compares the puncture resistance index of heads and shells based on Assumption #2 above. The I_R values for the shell were computed from Eq. (3.3) assuming $n = 0.95$. The head puncture resistance was inferred from the lading loss probabilities in Fig. 3.2 along with Eq. (3.6). The data point for the thickness of 0.112 inch corresponds to the jacket puncture resistance on the head. This data point was inferred from the analysis described below.

The inferred puncture resistance for a tank car head does not follow a simple power-law dependence on thickness, as Fig 3.7 indicates. However, it is still possible to predict the

relative effect of head shields and jackets. For example, when the head and head shield are separated by a layer of insulation, they should behave independently of one another, in which case the total puncture resistance is additive:

$$I_{R(tot)} = I_{R(head)} + I_{R(shield)} \tag{3.8}$$

At the other extreme, suppose that the head shield is completely fused to the head, such that the head is now thicker by 0.5 inch. In this case, the head and head shield are completely interdependent, and the puncture resistance corresponds to that of the combined thickness:

$$I_{R(tot)} = I_R\left(t_{head} + t_{shield}\right) \tag{3.9}$$

Equations (3.8) and (3.9) are generalizations of Eqs. (3.5) and (3.4), respectively.

Figure 3.8 shows the actual and predicted lading loss for heads with head shields or jackets. In jacketed cars with head shields, there is a standoff between the head and head shield. In this case the head and head shield appear to behave independently, and Eq. (3.8) accurately predicts the puncture resistance. In non-jacketed cars where the head shield is flush against the head, the behavior falls somewhere between independent and completely interdependent (Eqs. (3.8) and (3.9), respectively). There is definitely some interaction between the head and head shield in this case, but the performance in an accident is slightly better than would be achieved by increasing the head thickness by 0.5 inch.

When the head is protected by a thin jacket and a layer of insulation, there is a significant improvement in puncture resistance. A puncture resistance index of 0.49 was inferred for the jacket head using Eq. (3.8). This value is plotted on Fig. 3.7

This model can be used to predict the impact of proposed tank car design changes. For example, the proposed 600-lb chlorine car has a shell thickness of 0.981 inch and a head thickness of 1.136 inches. The current nominal shell and head thicknesses in chlorine cars is 0.777 and 0.81 inch, respectively. Both car designs are jacketed and insulated, but the proposed design includes a 0.5-inch head shield. Using the above model and regression fits, the current chlorine car design has a lading loss probability of 1.9% due to shell puncture and 2.5% due to head puncture. This translates to 19 shell punctures and 25 head punctures for every 1000 cars involved in a mainline accident, or a total of 44 punctures per 1000 cars. The proposed design modification would reduce this number to 12 punctures per 1000 cars, which is a 73% decrease. However, improving the material properties can have an even greater effect than increasing thicknesses. Suppose, for example, that improved upper shelf toughness in the next generation of tank car steels results in a doubling of the puncture resistance index. That is, assume that the puncture energy for a given tank car geometry doubles compared to traditional tank car steels. Given the current chlorine car design, the predicted number of punctures per 1000 cars involved in a mainline accident would decrease from 44 to 2, which is a 95% reduction. If the improved material properties are combined with the proposed design modification, the number of predicted punctures would decrease to 2 per 10,000 cars.

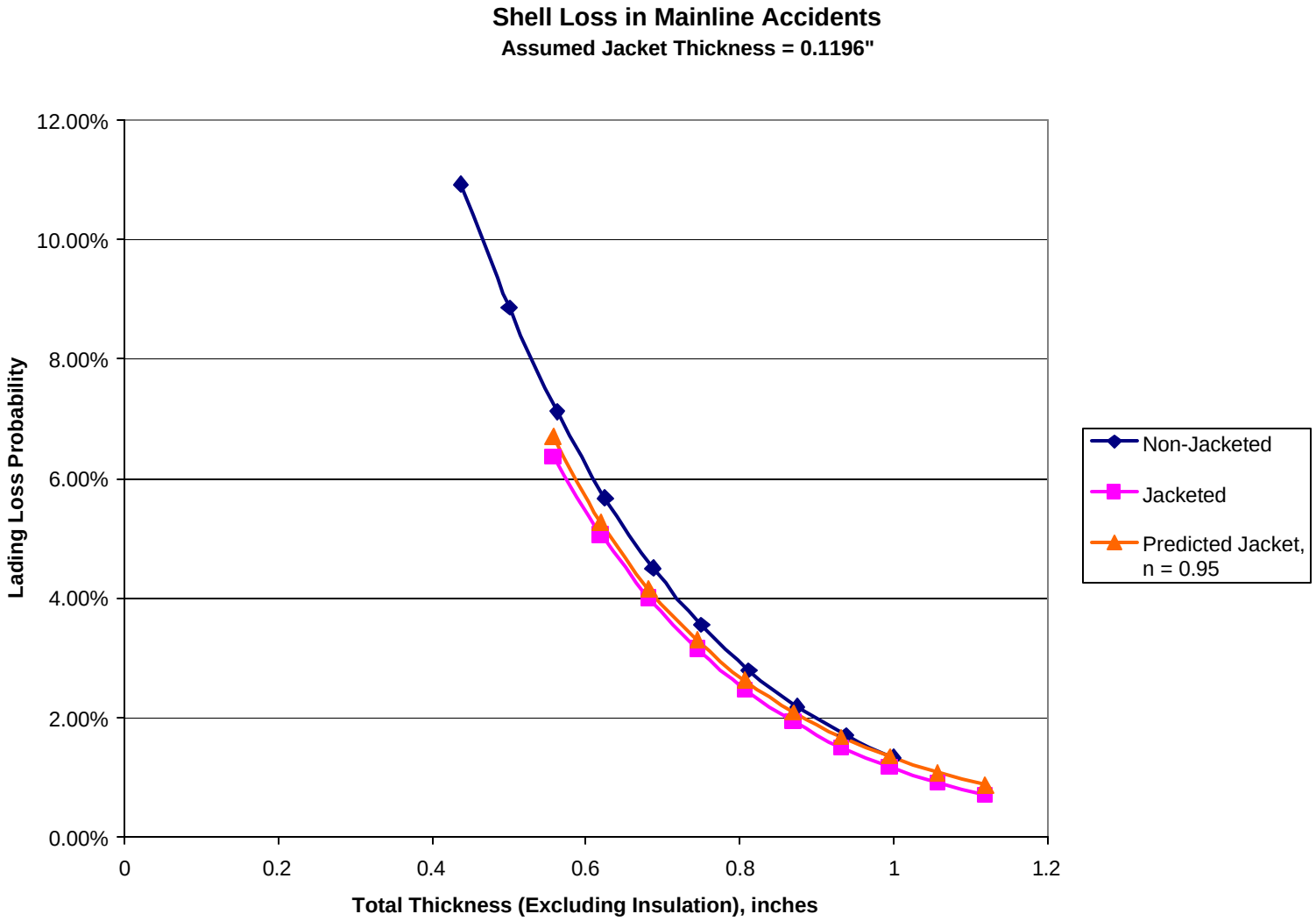

FIGURE 3.6 Prediction of the effects of a jacket on lading loss through the shell. Data taken from RSI-AAR Report RA-05-02 [16].

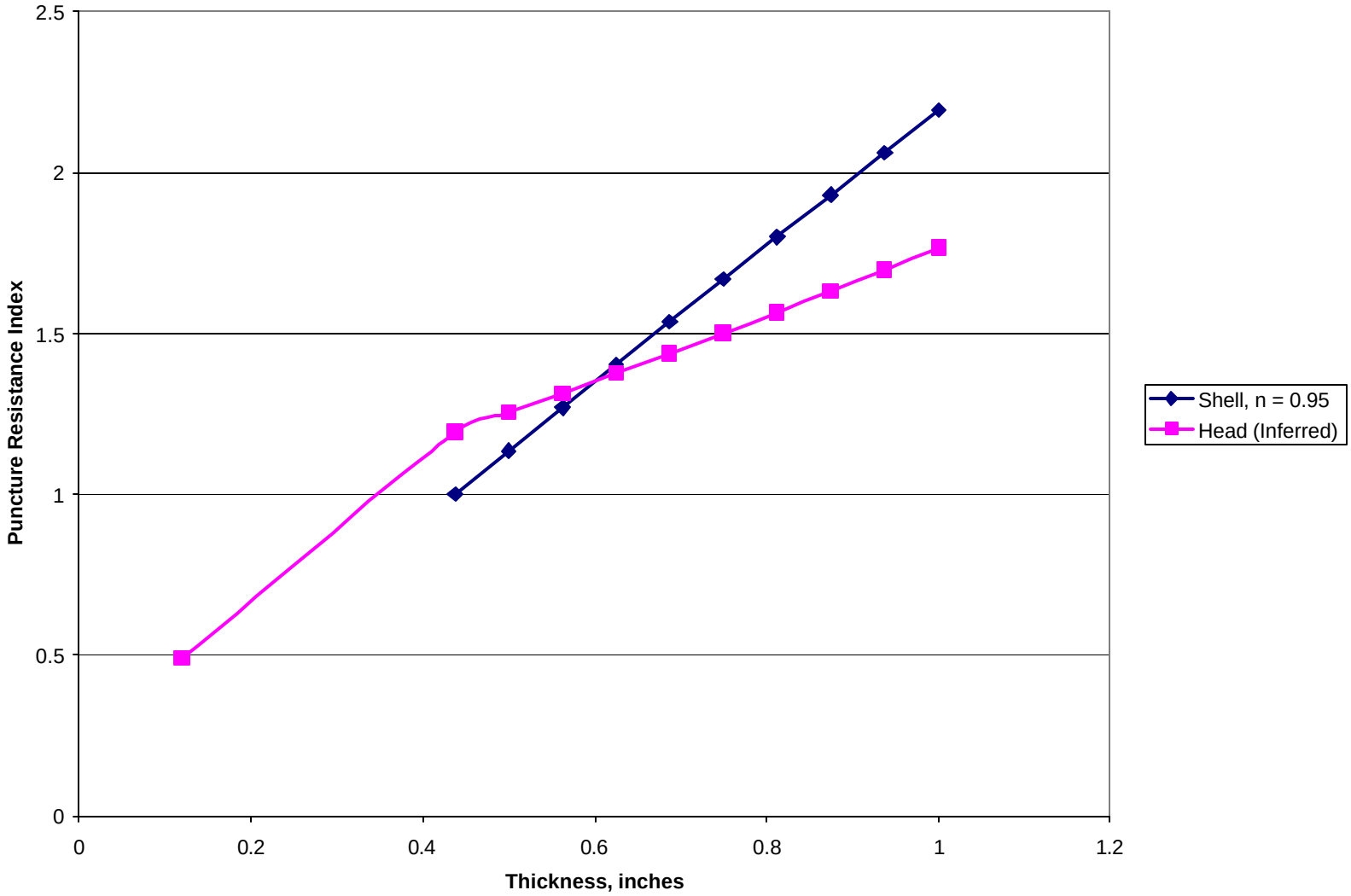

FIGURE 3.7 Puncture resistance index versus thickness for heads and shells.

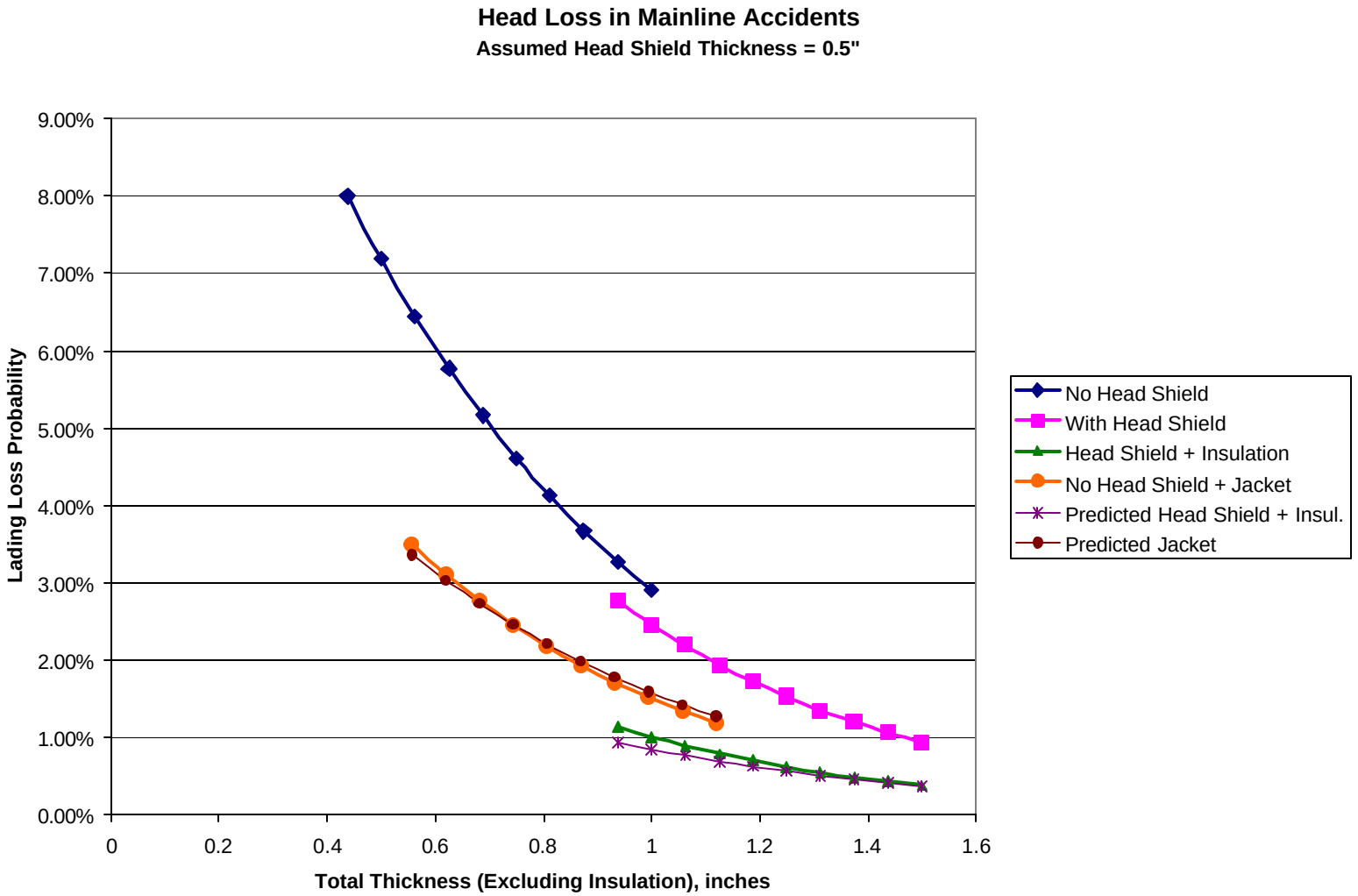

FIGURE 3.8 Predicted effect of head shields and jackets on lading loss through heads. Data taken from RSI-AAR Report RA-05-02 [16].

4 DYNAMIC COLLISION SIMULATION

During the Minot investigation, the present authors performed a series of computer simulations that were geared toward understanding the relationship between material properties and catastrophic rupture of tank cars [11]. These analyses combined detailed nonlinear dynamic collision simulation with a material model that incorporates ductile fracture. This work is summarized here because much of the computer modeling methodology developed in the Minot investigation can be used to study the effect of tank car design and material properties on puncture resistance.

4.1 Material Model for Ductile Fracture

The Gurson-Tvergaard model [17-20] simulates void growth and ductile fracture through a strain-softening constitutive law. Strain softening is captured through a void volume fraction, which increases with plastic flow. Fracture occurs when the void volume fraction reaches a critical value. This material model is implemented in some commercial finite element codes, including ABAQUS Explicit and LS-DYNA, both of which were used in the Minot investigation.

The Gurson-Tvergaard yield condition is given by:

$$\Phi = \left(\frac{q}{s_y} \right)^2 + 2q_1 f \cosh\left(-q_2 \frac{3p}{2s_y} \right) - \left(1 + q_3 f^2\right) = 0 \tag{4.1}$$

where q is the effective Mises stress, p is the hydrostatic pressure, σ_y is the yield stress of the fully dense material, q_1, q_2, q_3 are porosity material parameters, and f is the void fraction.

The void growth and void nucleation rate gives the total change in the void volume fraction, $\dot{f}$:

$$\dot{f} = \dot{f}_{gr} + \dot{f}_{nucl} \tag{4.2}$$

where $\dot{f}_{gr}$ is from the existing void growth, and $\dot{f}_{nucl}$ is from the nucleation of new voids. The growth of existing voids is given by:

$$\dot{f}_{gr} = (1 - f)\dot{e}^{pl} \tag{4.3}$$

and the growth of new voids due to nucleation is given by:

$$\dot{f}_{nucl} = A\dot{\bar{e}}_m^{pl}$$
$$A = \frac{f_N}{s_N\sqrt{2p}}\exp\left[-\frac{1}{2}\left(\frac{\bar{e}_m^{pl} - e_N}{s_N}\right)^2\right] \tag{4.4}$$

The nucleation strain is assumed to follow a normal distribution with a mean value of ε_N, and a standard deviation s_N. f_N is the void volume fraction of the new voids; which are nucleated only in tension.

For a numerical analysis, the initial void volume fraction, f_0, is defined for the material. The porous failure criteria is given by the critical void volume fraction, f_c. When $f \geq f_c$ at all the material points (integration points) of a finite element, the stress carrying capacity of the material is reduced to zero and the finite element is removed from the model. The progressive failure of elements results in crack growth across the mesh.

4.2 Calibration of Material Model with Charpy Impact Tests

In order to apply the Gurson-Tvergaard model to a particular problem, the model must first be calibrated to experimental results. In this instance, we chose to calibrate the material model to Charpy impact results. A series of finite element simulation of Charpy tests were performed, and the material model was adjusted to achieve various values of absorbed energy.

Figure 4.1 shows the finite element model used for Charpy simulations, which were performed with ABAQUS Explicit. The anvil and striker were treated as contact surfaces, so the specimen is free to move relative to the test machine during fracture. The initial velocity of the striker was 235.9 in/sec (13.4 mph), which is equivalent to being dropped from a height of 6 ft. The velocity of the striker decreased as it imparted its kinetic energy to the specimen. This effect is handled automatically in the analysis through energy conservation. The weight of the striker was 49.15 lb, so the total available energy was 295 ft-lb. The fracture energy is equal to the total internal energy absorbed by the specimen. This quantity is output by ABAQUS Explicit.

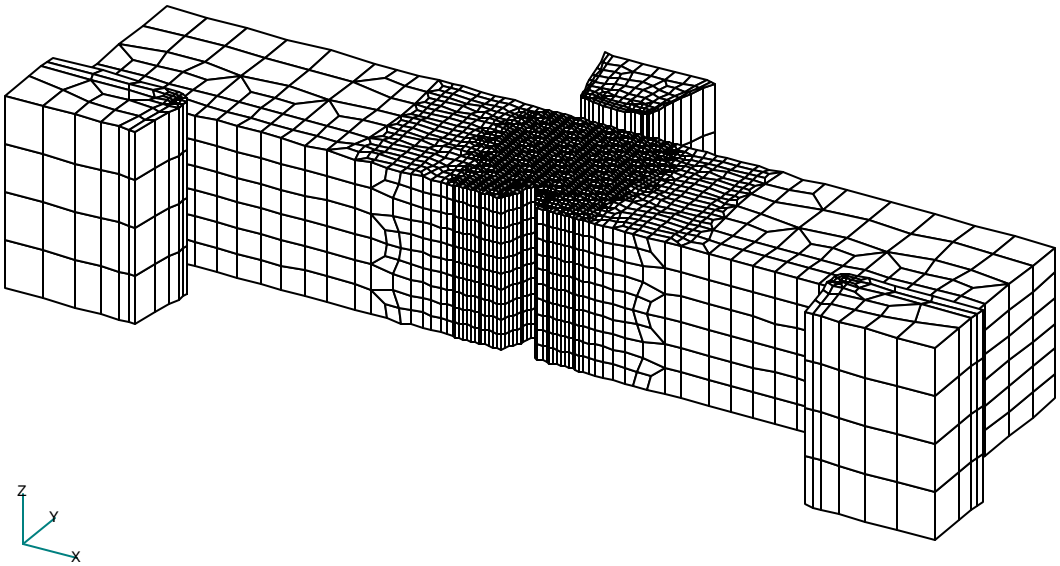

FIGURE 4.1 Finite element model for simulation of the Charpy test.

The stress-strain curve used in the analysis is shown in Fig. 4.2 and Table 4.1. This curve is representative of TC 128 B steel at 37°F, which is the estimated metal temperature at the time of the Minot derailment. The following Gurson parameters were assumed, based on the published literature:

Gurson parameter $q_1 = 1.81$
Gurson parameter $q_2 = 0.82$
Gurson parameter $q_3 = 3.2761$
Nucleation strain mean value $\varepsilon_N = 0.30$
Nucleation strain standard deviation $s_N = 0.10$
Void nucleation initial void volume fraction $f_N = f_0$
Critical void fracture $f_c = 0.15$

The initial void fraction, f_o, was used as a fitting parameter in the model

Figure 4.3 is a plot of absorbed energy versus initial porosity. It was decided to perform the full-scale collision simulations with a Charpy energy of 100 ft-lb, which corresponds to an initial porosity of 0.0144. Figure 4.4 shows the specimen near the end of the test for a 100 ft-lb material.

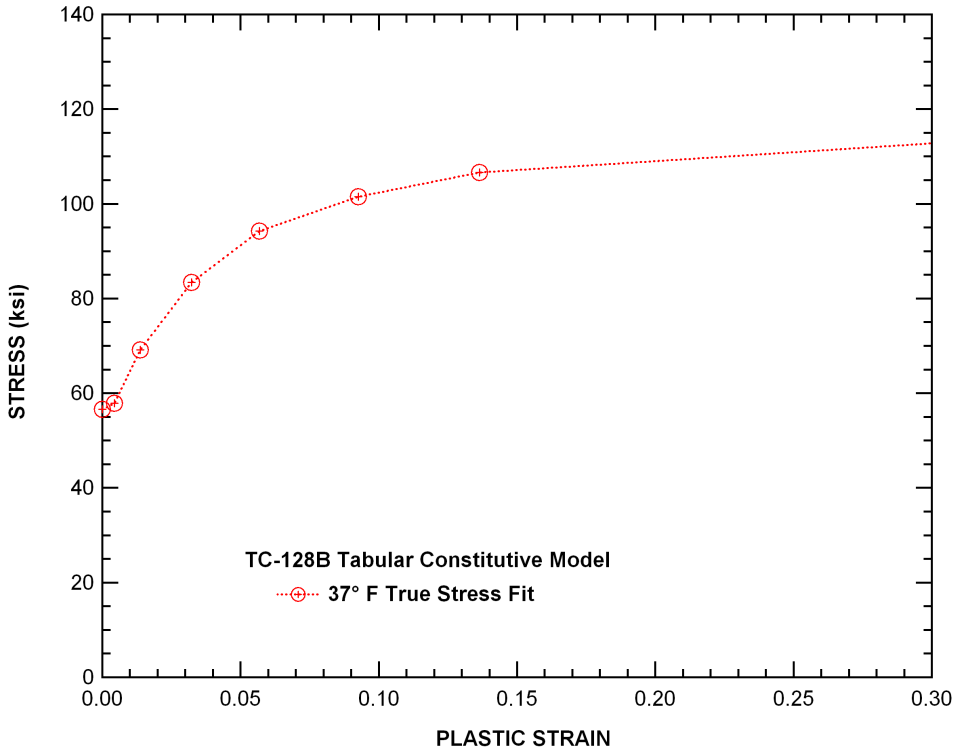

FIGURE 4.2 Stress-strain curve used for all finite element analyses.

TABLE 4.1
Tabular TC128B stress-strain curve values (37° F)

Point No.	Plastic Strain (in/in)	True Stress (ksi)
1	0.00E+00	56.6
2	4.37E-03	57.9
3	1.37E-02	69.2
4	3.22E-02	83.4
5	5.69E-02	94.3
6	9.26E-02	102.0
7	1.36E-01	107.0
8	5.96E-01	124.0

The material parameters determined from the Charpy simulation cannot be used directly in a full-scale simulation. The appropriate material parameters for a given toughness value are mesh sensitive. That is, the results change as the element size changes. The reason for this is that fracture in real materials is governed by microstructural length scales such as grain size and inclusion spacing. Finite element analysis is based on continuum theory, so the element size becomes the de facto material length scale.

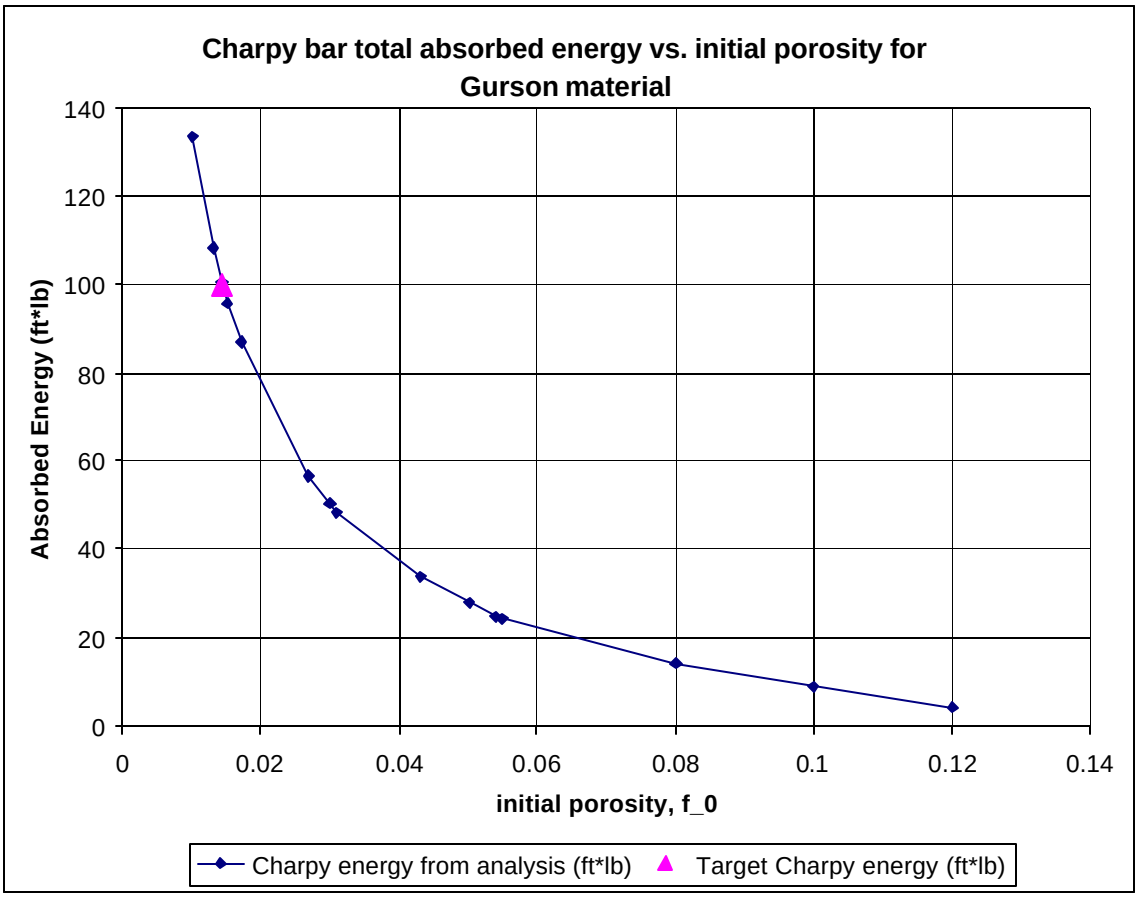

FIGURE 4.3 Effect of initial porosity on Charpy energy. Element size = 0.01 inch.

The simulation of tank car failures used shell elements in the collision zone with a 2-inch length in each direction in the plane of the tank wall. The Charpy simulation used 0.01-inch elements in the fracture zone. Refinement of the full-scale tank car to the level of the Charpy model is impossible with existing computational resources. Consequently, the material parameters for a 100 ft-lb steel had to be adjusted for the 2-inch element size. This was accomplished by gradually increasing element size in a benchmark problem and re-calibrating the material model at each step.

4.3 Full-Scale Simulation of Tank Car Collisions and Rupture

A series of tank car impact analyses were performed to analyze the conditions for which a puncture or rupture response is obtained. The tank car model used in these analyses was based on a previous finite element model of a DOT 112A340W pressure tank car was generated to analyze the loads and stresses in the tank car as a result of service and salvage operating conditions [21-23]. The LS-DYNA finite element code was used for the tank car modeling [24]. LS-DYNA is developed and maintained by the Livermore Software Technology Corporation (LSTC). LS-DYNA is an explicit nonlinear three-

dimensional finite element code for analyzing the large deformation dynamic response of solids and structures. It has many features ideally suited to analysis of vehicle collisions. As a result, LS-DYNA is widely used and well accepted in the crashworthiness community as a state-of-the-art code. Equipment manufacturers commonly use LS-DYNA in the design of passenger rail car and automotive crash safety. The model for the tank car was developed using the TrueGrid preprocessor code [25].

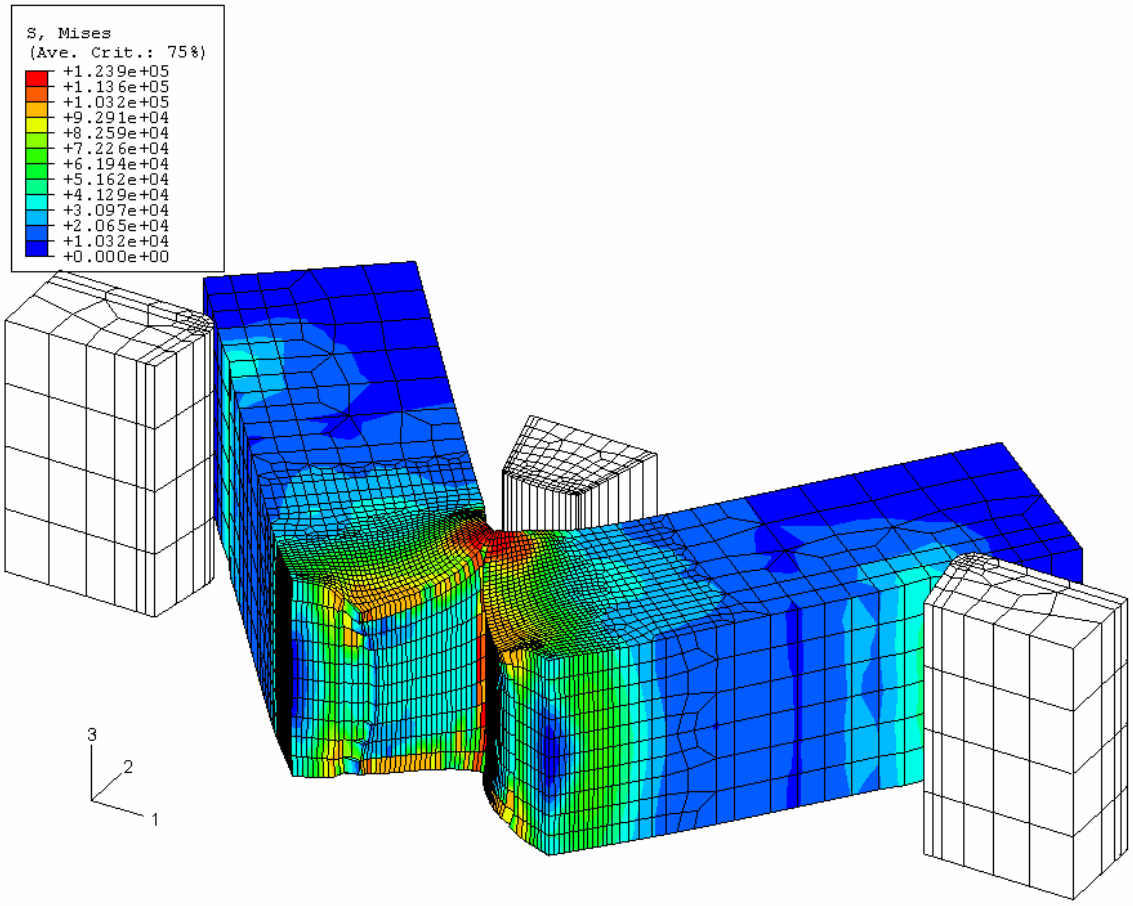

FIGURE 4.4 Simulated Charpy test on a 100 ft-lb material.

Two external views of the original DOT 112A340W tank car model are shown in Fig. 4.5. The structure includes the tank with ellipsoidal heads, manway, stub sill, bolster, and bogie structures. The geometry of the tank car structures in the model were based on a design originally developed by Union Tank Car. Figure 4.5(b) gives a detailed view of the original model car end structures and the associated model mesh resolution.

For the impact analyses described here, the model was modified to include greater fidelity in the modeling of the draft gear and stub sill geometry as well as improved mesh refinement. In addition, the tank wall thickness was modified to 0.6875 inch, corresponding to the values measured and reported in the NTSB Materials Laboratory Factual Report [2]. The external insulation and jacket were not included in the model. The stub sill geometry was also modeled in greater detail to allow for the inclusion of a

model for the coupler and draft gear. The final modification made to the model was to significantly increase the mesh resolution in the impact zone. The model was refined to have approximately 2 inch elements in the impact zone to resolve the damage distributions caused by impact.

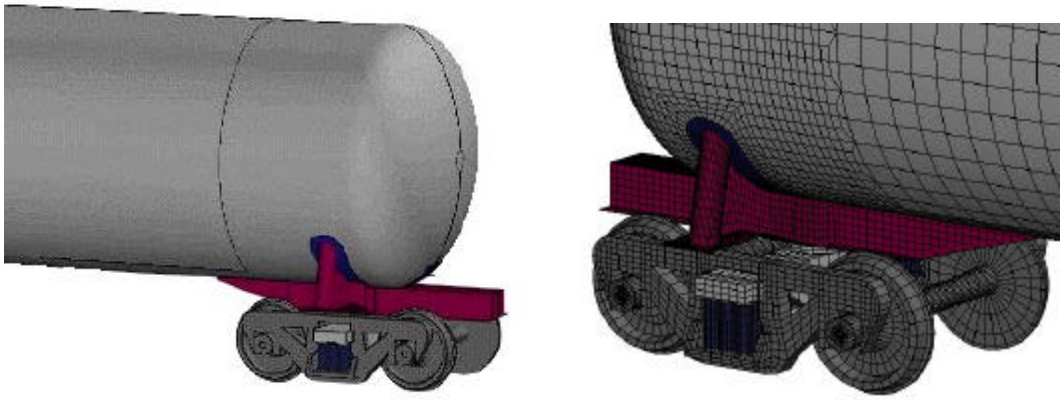

(a) Tank car model **(b) Detail of the tank car mesh**

FIGURE 4.5 Original model generated for a 112A340W pressure tank car.

A 55 psi pressure was applied on the inside of the tank to model the pressure stresses from the anhydrous ammonia at 37°F. The mass of the lading was included in the tank car model using an increased mass of the tank shell. The inertial effects of the lading were important for developing the full collision forces and resulting motions of the vehicles in the simulations. Gravitational accelerations are also significant for the collision behavior and were included in the simulations. The collision analyses were used to investigate the impact conditions that result in either a puncture or an unstable tank rupture. Different impact scenarios and speeds were used that are representative of the conditions expected from derailment kinematics analyses performed as part of the Minot Investigation. Two simulations are described here that are representative of the impact behaviors.

The overall impact orientation used for these example impact simulations is shown in Fig. 4.6. Two derailed tank cars are resting on their sides with the primary target tank car oriented at 40 degrees from normal to the original direction of travel. The second target tank car behind the target has an increased mass to be more representative of a set of equipment stacked behind the target car. The mass increase is representative of a car that is between 3 and 4 times the weight of a single car. Similarly, a pair of coupled tank cars is used as the impactor (bullet cars). Again, the trailing bullet car has an increased mass (3-4 X) to provide some of the inertial effects of the train cars behind the derailment.

The calculated impact response for the above impact scenario and an impact speed of 25 mph is shown in Fig. 4.7. The impact behavior results in a puncture of the target tank car by the impact of the coupler and stub sill on the side wall. The subsequent blunt impact by the bullet tank car head on the target tank pushes the target tank cars out of the path of the bullet cars. A more detailed view of the calculated impact damage (puncture) to the target tank is shown in Fig. 4.8.

FIGURE 4.6 Impact scenario used to investigate tank car response.

The corresponding calculated impact response for the above impact scenario with an increased impact speed of 30 mph is shown in Fig. 4.9. The impact behavior results in a rupture behavior of the tank where a fracture propagates around the circumference of the tank and the end of the tank and tank head are removed as a couple of large debris fragments. The fracture propagates from the site of the coupler head impact and puncture of the tank wall in the early stages of the impact response. A more detailed view of the damage to the tank during the rupture response is shown in Fig. 4.10.

During the inspection of some of the recovered tank car debris by the various parties involved in the Minot investigation, a concern was raised that there appeared to be an absence of massive collision/derailment damage in the immediate vicinity of some of the catastrophic ruptures. The implication was that the lack of denting or other collision damage was evidence of inferior material in the tank cars involved in the Minot incident. However, statements such as this were made without examining all of the remnants from a given tank car fracture.

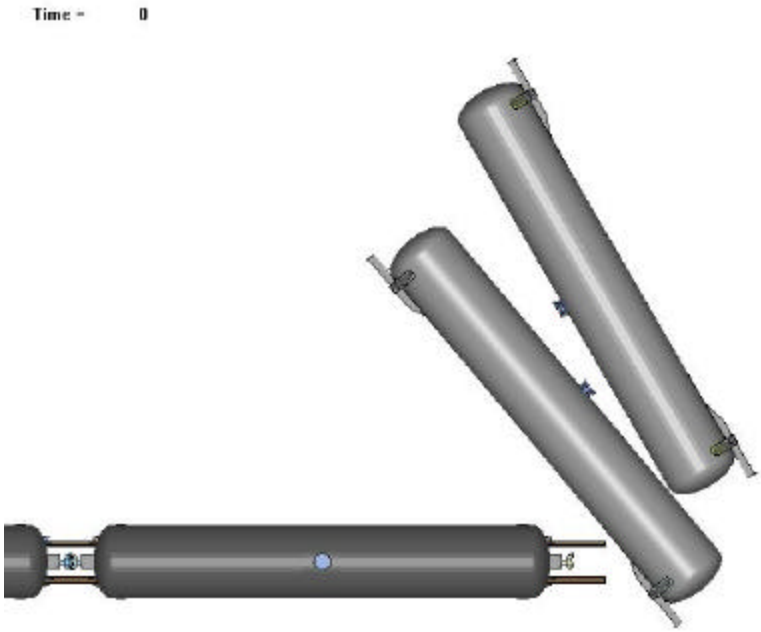

a) Initial Configuration

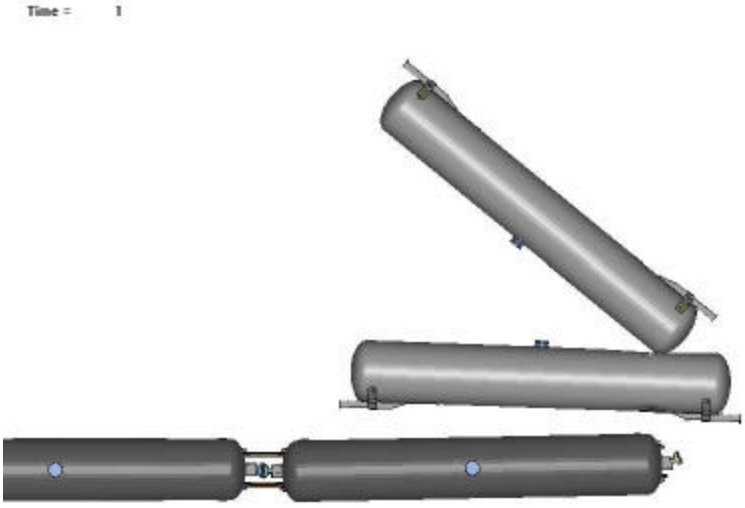

b) Impact Damage at 1.0 second (Punctured)

FIGURE 4.7. Impact response of the tank cars for a 30 mph impact.

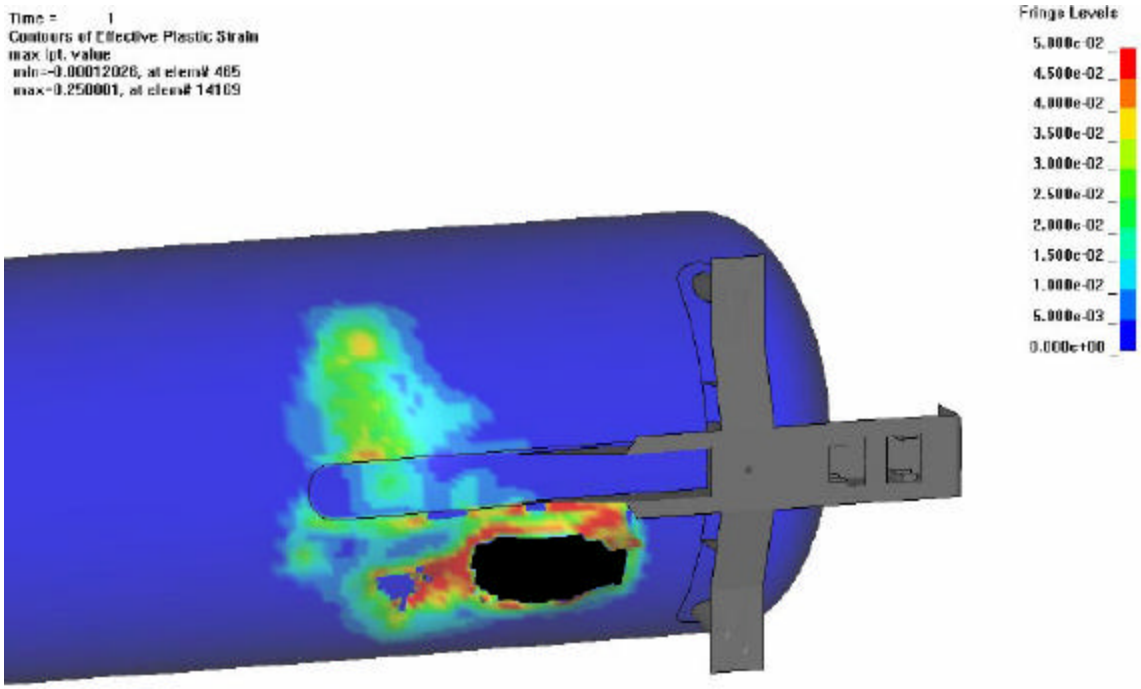

FIGURE 4.8 Impact damage to the target tank car for the 25 mph impact.

We performed a tank impact and rupture analysis to demonstrate that observations of the presence or lack of collision damage on a single remnant can be misleading. The impact conditions were a side impact of two tank cars into two stationary tank cars. The outer tank cars are increased in weight to include inertial effects of multiple cars. The impact occurred near the center of the target tank at 20 degrees from normal as shown in Fig. 4.11. The collision speed in this example was 25 mph and resulted in a catastrophic rupture.

The calculated intermediate damage states at 0.35 seconds and 0.50 seconds are shown in Fig. 4.12. At 0.35 seconds the coupler head has punctured through the outer shell and by 0.5 seconds the tank head of the bullet tank car has impacted the target car resulting in extensive impact damage. The subsequent catastrophic rupture behavior at a time of 1.0 seconds is shown in Fig. 4.13. The rupture has two main circumferential fractures. The resulting major debris produced in the rupture are the large A-end and B-end sections and additional tank wall debris that is between 3 and 6 feet wide between the two circumferential fractures.

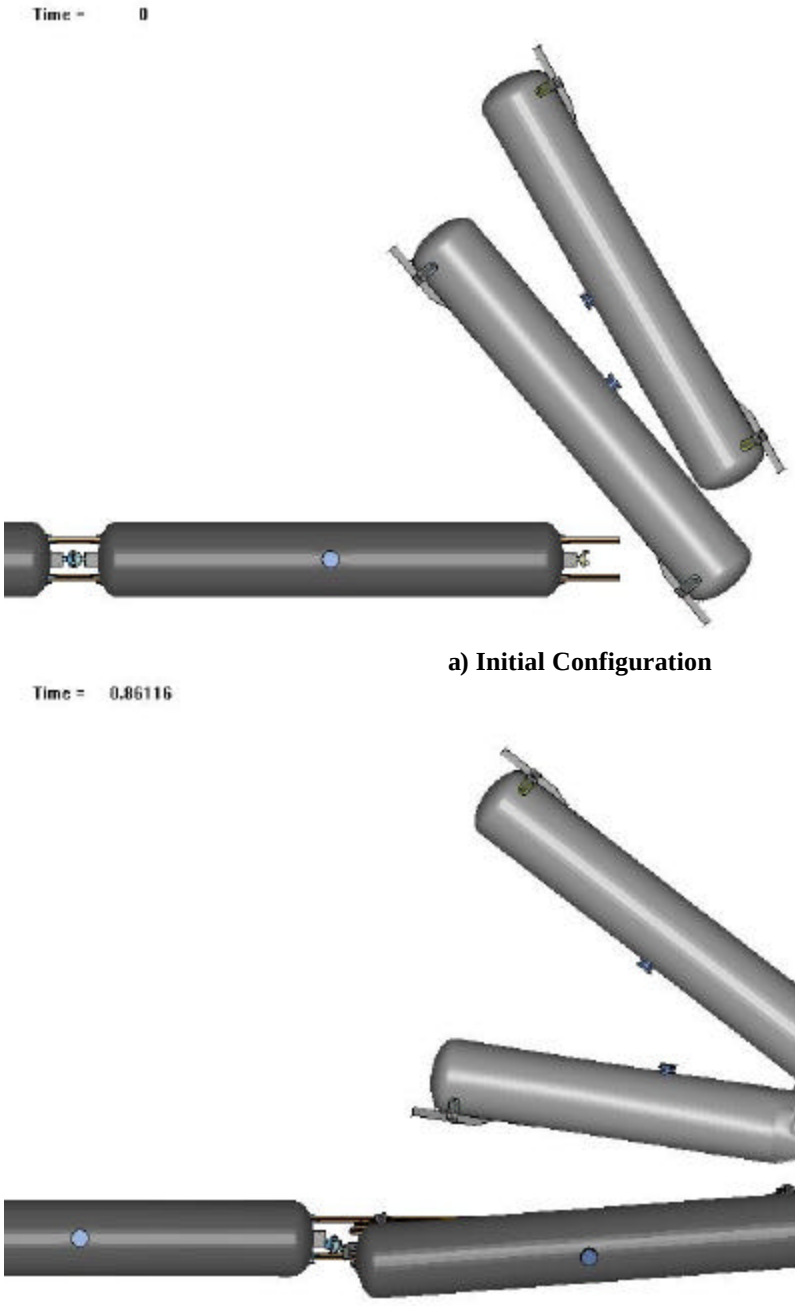

a) Initial Configuration

b) Impact damage at 0.86 second (Ruptured).

FIGURE 4.9 Impact response of the tank cars for a 30 mph impact.

The calculated final damage to one end of the tank car is shown in Fig. 4.14. The tank section has little residual evidence of the extensive impact damage in this section of the tank. Without gathering all of the debris from this tank and reconstructing the rupture process, much of the evidence of the original impact damage would be carried away by the central tank wall debris.

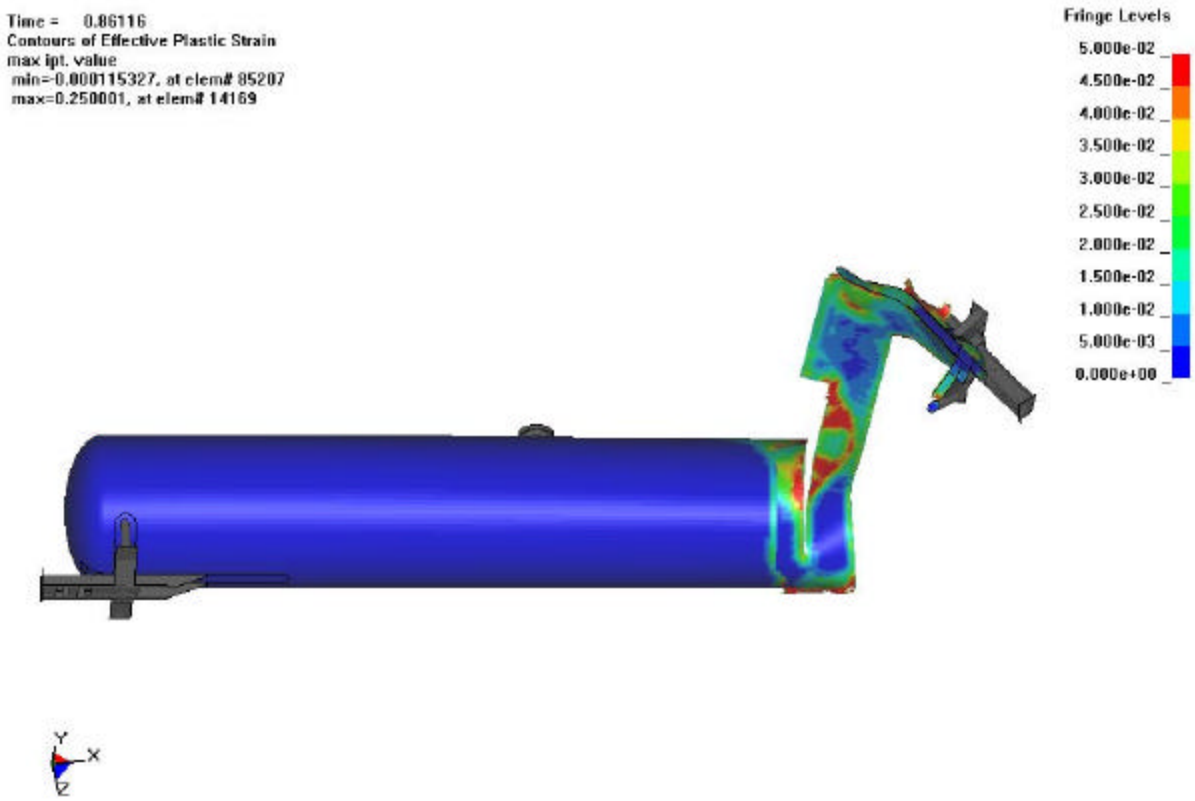

FIGURE 4.10 Impact damage to the target tank car for the 30 mph impact.

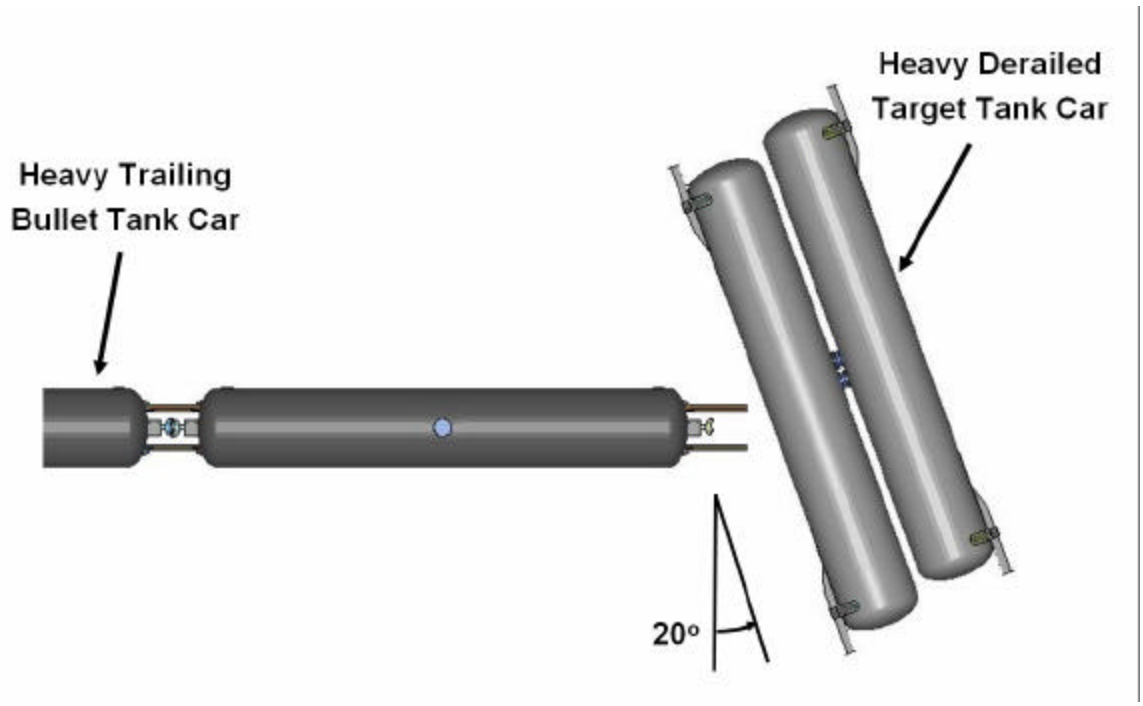

FIGURE 4.11 Impact scenario for the tank car impact and rupture analysis.

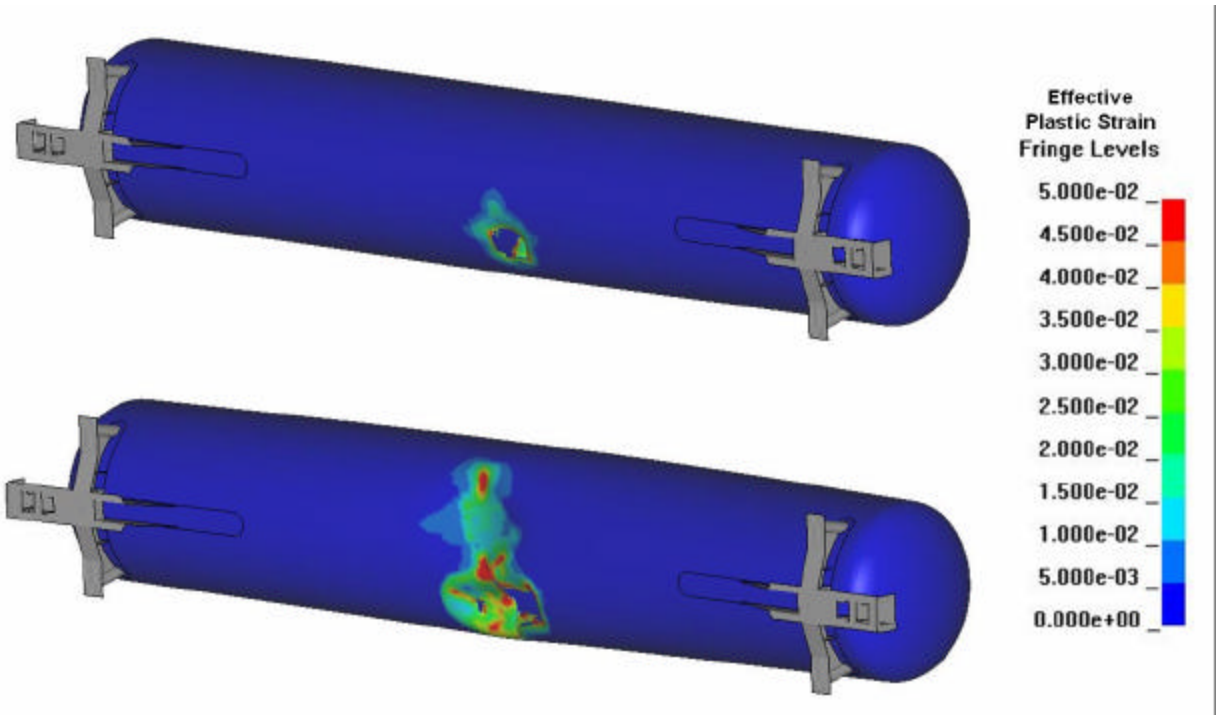

FIGURE 4.12 Calculated intermediate impact damage states (25 mph – Middle impact – 100 ft-lb shell material).

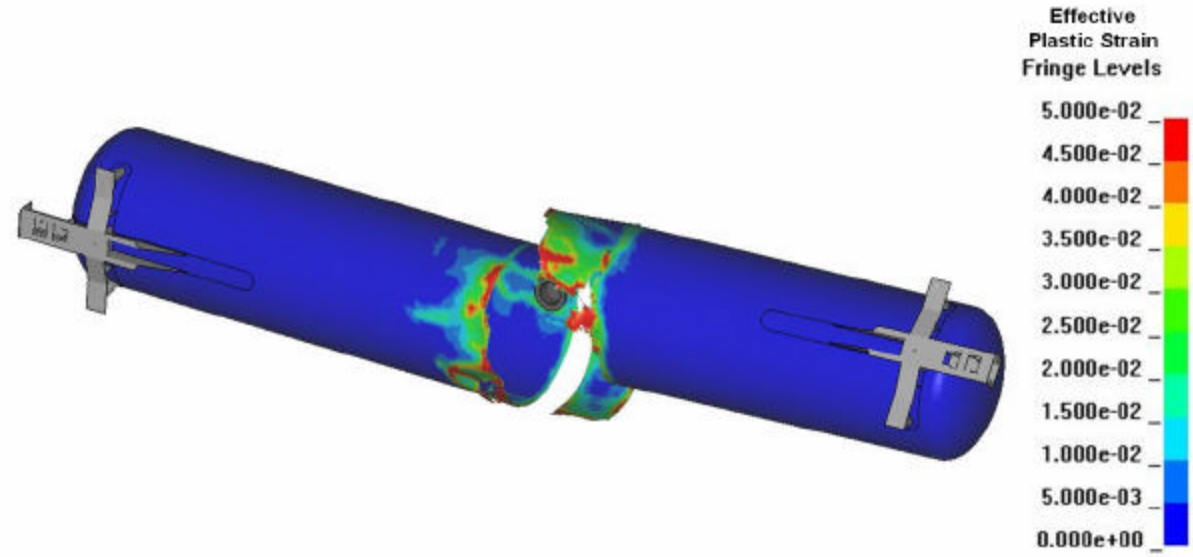

FIGURE 4.13 Calculated tank shell rupture response (25 mph – Middle impact – 100 ft-lb shell material).

The computational procedures described in this section will need to be modified to be applied to a study on puncture resistance. The mesh will need to be significantly refined in the impact zone in order to model puncture with sufficient resolution. The models

used in the Minot analysis had relatively coarse meshes because we were analyzing catastrophic rupture, and the initial puncture event was less important. Although a puncture study will require significantly more local mesh refinement, it will not be necessary to model detailed collision scenarios with multiple tank cars. For example, puncture by a coupler can be addressed with a model of the target car and the impacting coupler. The mass of the cars impacting the target can be incorporated into the coupler.

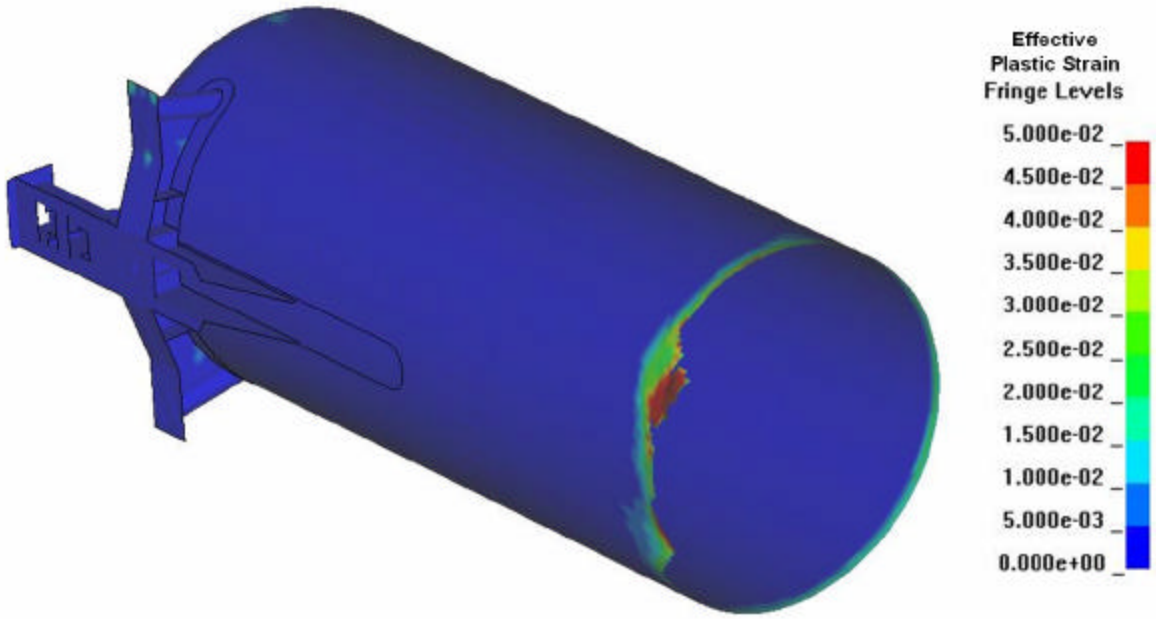

FIGURE 4.14 Residual tank section with minimal evidence of impact damage (25 mph – Middle impact – 100 ft-lb shell material).

5 DYNAMIC PUNCTURE SIMULATION

The computational methods described in the previous chapter can be used to study puncture resistance, provided some modifications are made. The models shown in Chapter 4 were optimized to study catastrophic rupture due to collision forces that were likely present at the Minot derailment. In a puncture study, the goal would be to quantify the relative effect of variables such as wall thickness and material toughness on puncture resistance.

An earlier study [26] attempted to evaluate puncture resistance using finite element analysis. This study was of limited value because the finite element analyses were two-dimensional, quasi-static, and assumed a very simplistic material failure criterion. Nevertheless, these analyses predict that puncture resistance should increase with thickness, which is broadly consistent with the trends shown in Chapter 3.

A major advantage of the analysis approach described in Chapter 4 is that the material model can quantify the effect of upper-shelf toughness on puncture resistance. Full-scale dynamic simulation of tank car punctures is beyond the scope of the present study, but should be undertaken in a follow-up phase. Some preliminary results from small-scale models are presented below.

Standard test methods to quantify puncture resistance of a tank car do not exist at present, so two candidate experiments are considered here. In the first example, an unnotched rectangular bar is struck by a pendulum. The second experiment involves a cylindrical bar with a rounded tip that pierces a plate that is clamped on its edges.

5.1 Charpy Calibration

The Gurson-Tvergaard material model, which is described in Section 4.1 above, was calibrated to Charpy impact toughness, as was the case in the Minot analysis. In this case, however, the element size was fixed at 0.0394 inch (1 mm) so that the material model did not have to be re-calibrated for difference element sizes. All analyses in this Chapter used the same element size in the fracture zone.

Figure 5.1 shows the finite element model for the Charpy simulation. The same material properties were used in the present study as were used in the analysis described in Chapter 4. Figure 5.2 is a plot of initial porosity versus energy absorbed. This calibration differs slightly from Fig. 4.3 because of different element sizes on the notch plane.

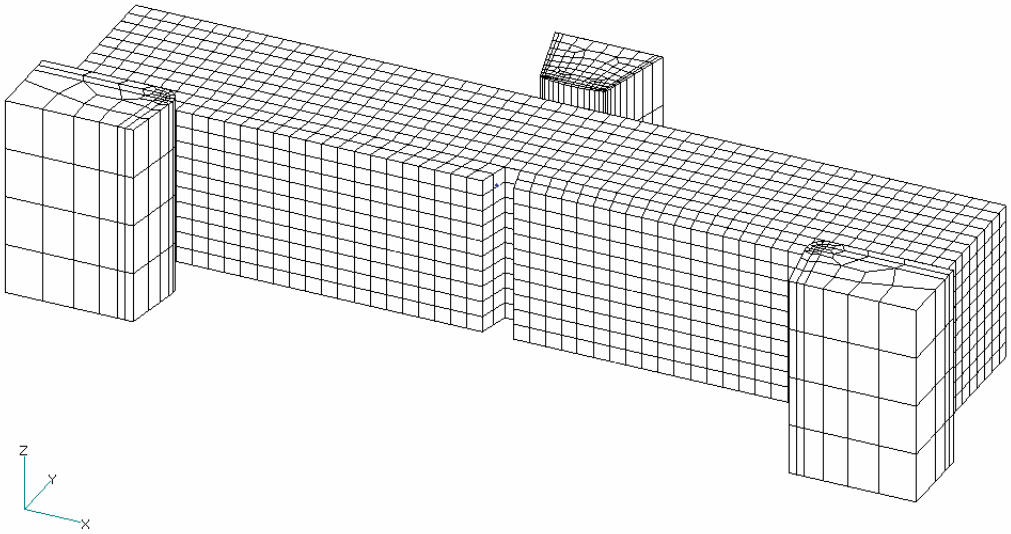

FIGURE 5.1 Charpy simulation with 0.0394-inch (1 mm) elements on the notch plane.

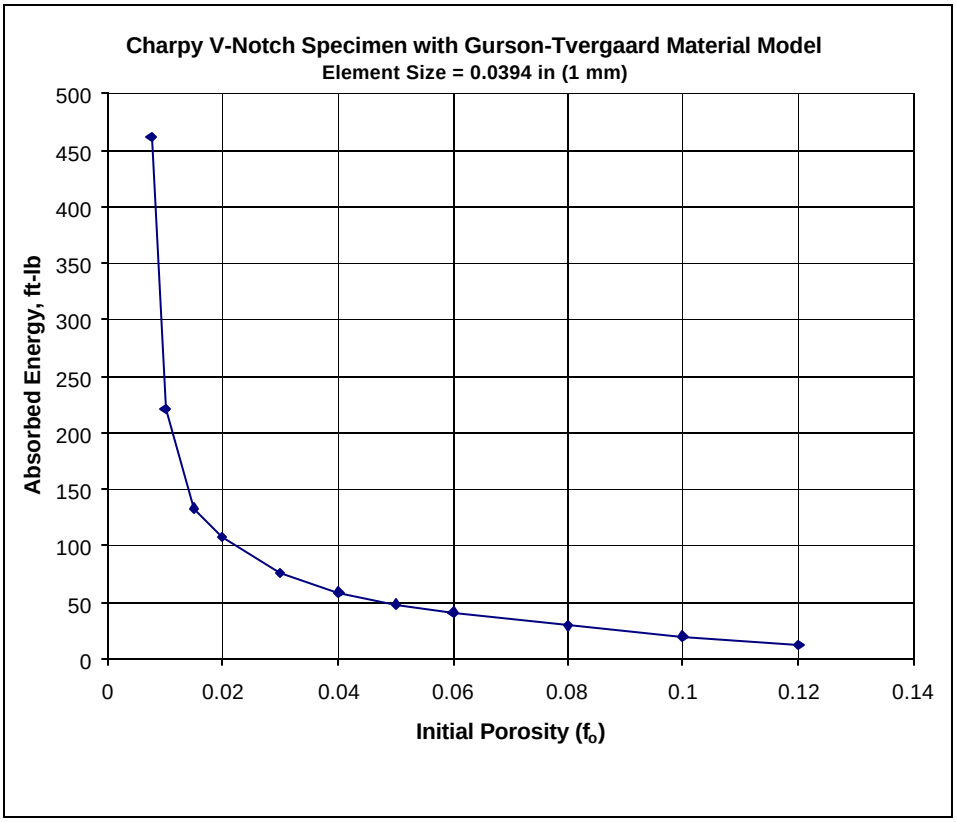

FIGURE 5.2 Calibration of Charpy energy with initial porosity.

5.2 Fracture Simulation of Unnotched Bars

An overall view of an impact test on an unnotched bar is shown in Figure 5.3. The bar is 12-inches long and fixed at both ends. It is impacted with a Charpy striker, and the energy absorbed is computed. This experiment could not be performed in a standard Charpy machine because there is not sufficient energy available to break the sample. For example, refer to Fig. 2.23, which is a photograph of two unnotched Charpy specimens that failed to break in a 300 ft-lb machine.

Three bar sizes were considered, which are shown in Figs 5.4 to 5.6. The baseline geometry has a 0.394 x 0.394-inch (10 x 10 mm) square cross section, which is the same as an unnotched Charpy specimen. Specimens with reduced thickness were also considered. Figures 5.5 and 5.6 show specimens with 70% and 50% of the baseline thickness, respectively. The energy required to fracture these bars were computed at various initial porosity values, which correspond to specific Charpy toughness values.

A test such as this, whether it is a computer simulation or an actual experiment, is merely qualitative. However, it can be used to assess relative trends. For example, assume the fracture energy exhibits a power-law dependence on thickness:

$$E = l\, t^{n} \tag{5.1}$$

It should be possible to measure the exponent n by varying specimen thickness. Recall Section 3.2, where an n value of 0.95 for shell puncture resistance was inferred from the accident database.

Figure 5.7 is a plot of fracture energy versus thickness on a logarithmic scale. The computed n values range from 0.89 to 1.0, which is consistent with the value of 0.95 inferred from the accident database for shell punctures.

The relative effect of toughness on puncture resistance can also be inferred from qualitative experiments. Let us assume a different power-law relationship between fracture energy in the unnotched bar and upper-shelf Charpy energy:

$$E = g\left(CVN\right)^{m} \tag{5.2}$$

Figure 5.8 is a plot of fracture energy in the unnotched bar versus absorbed energy in CVN specimens with the same initial porosity. The exponent m is approximately 0.5 in this case. Therefore, if these trends translate to tank cars, it will take a four-fold increase in upper-shelf toughness to double the puncture resistance. Such an increase in toughness is achievable with sufficient reductions in sulfur content in conjunction with sulfide shape control (Chapter 2).

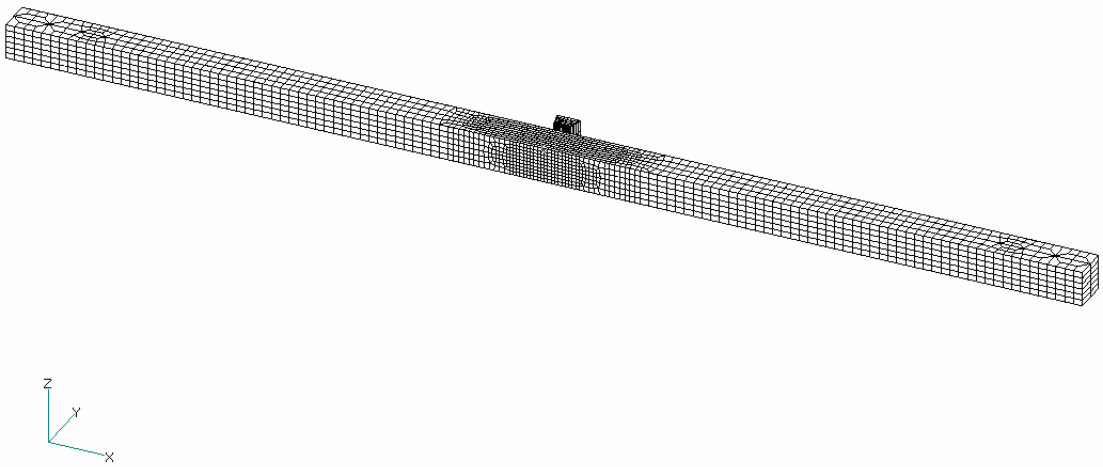

FIGURE 5.3 Impact test on a 12-inch long unnotched bar using a Charpy striker.

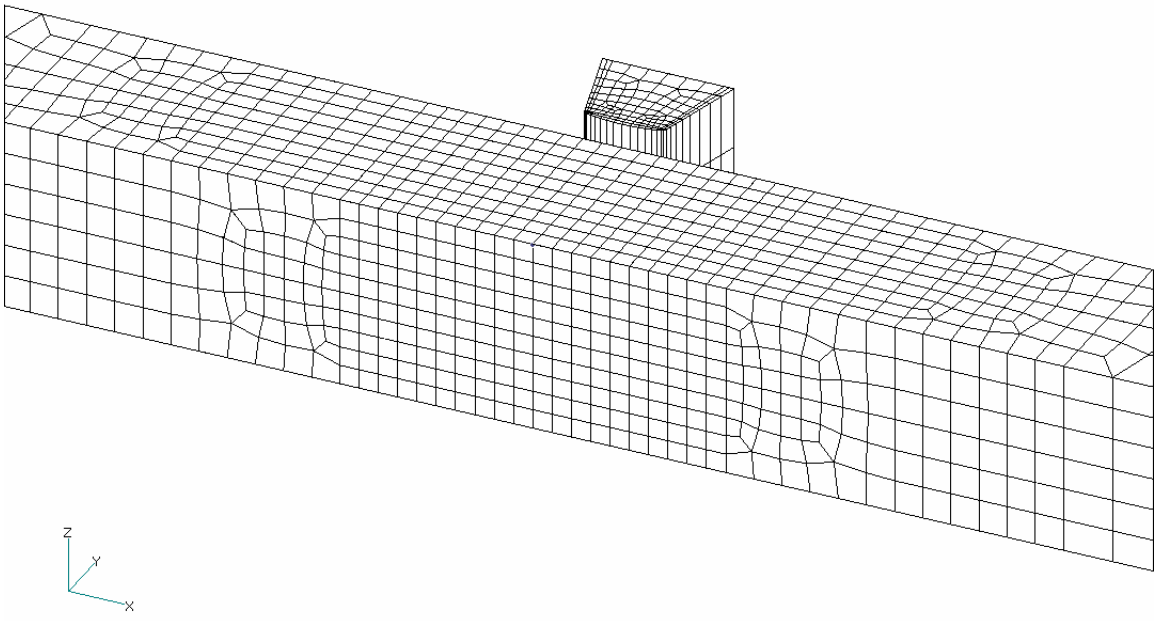

FIGURE 5.4 Full-size specimen with a square cross section.

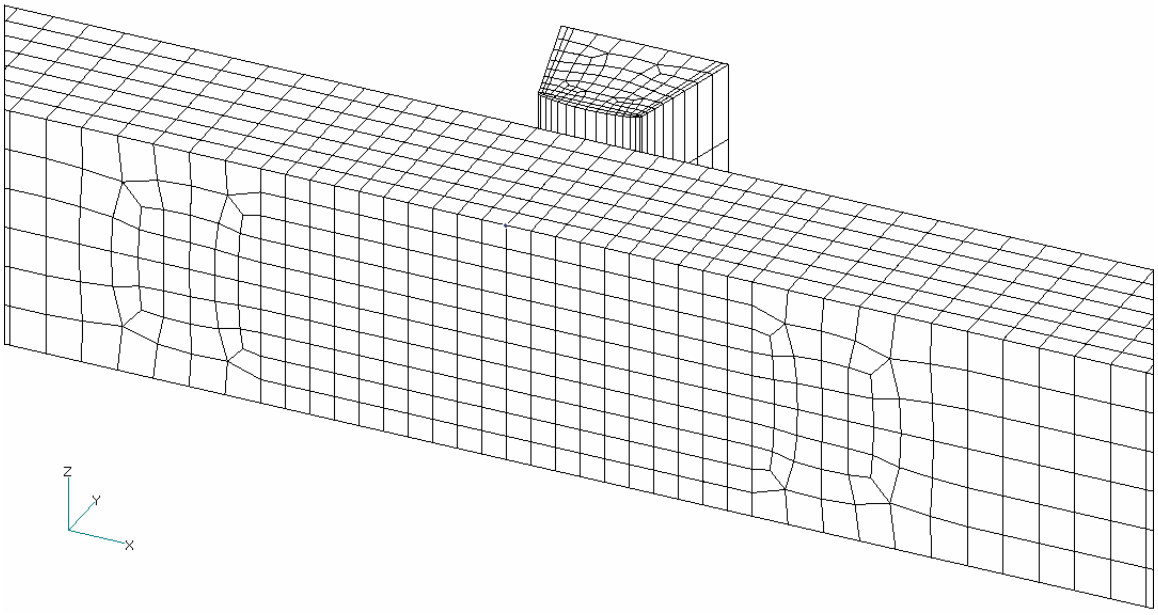

FIGURE 5.5 Bar thickness reduced to 70% of the baseline size.

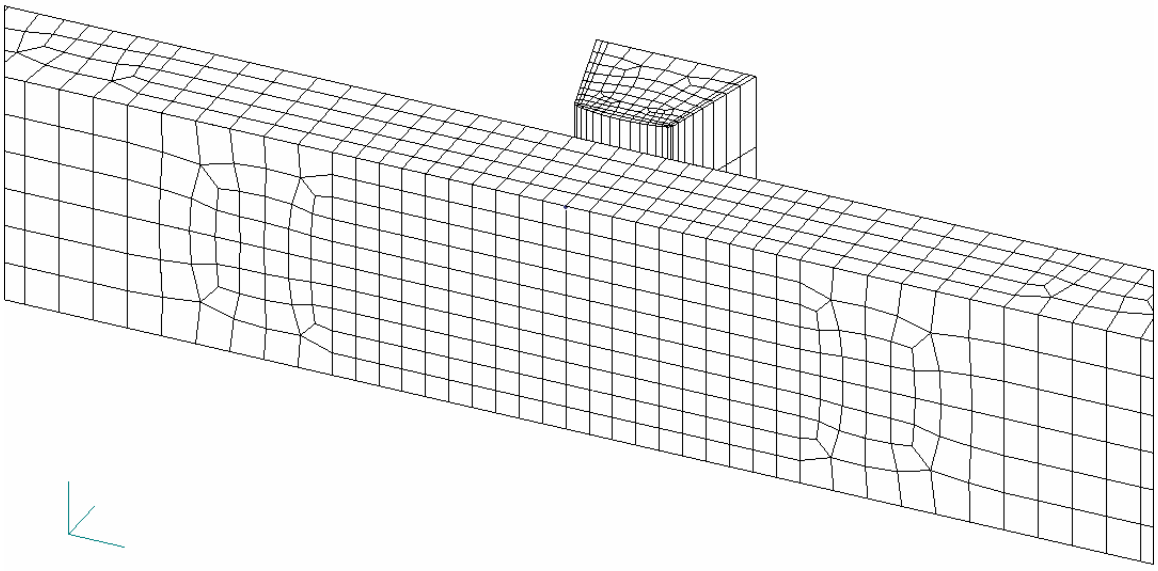

FIGURE 5.6 Bar thickness reduced to 50% of the baseline size.

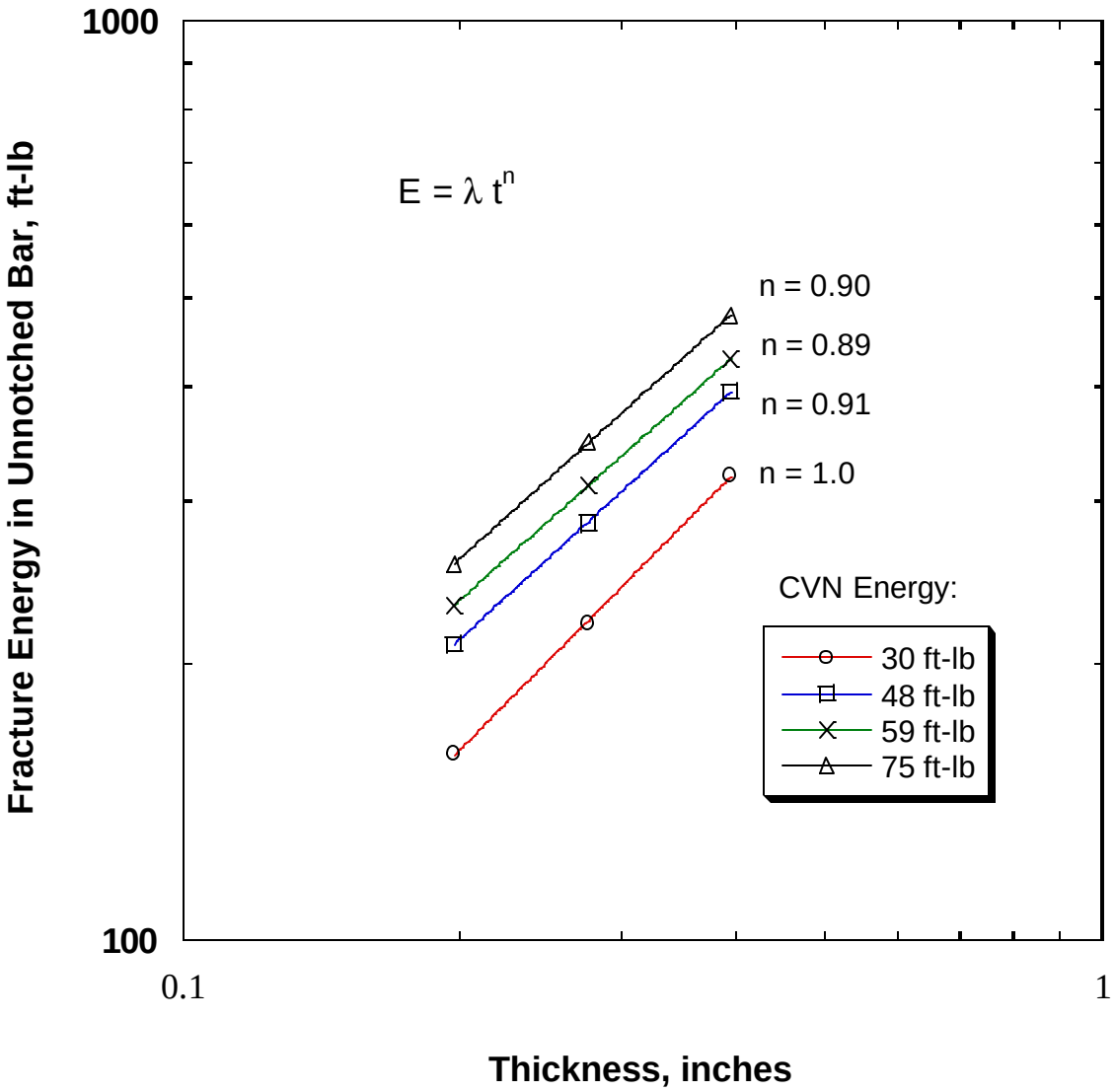

FIGURE 5.7. Relationship between fracture energy in the unnoched bar and thickness.

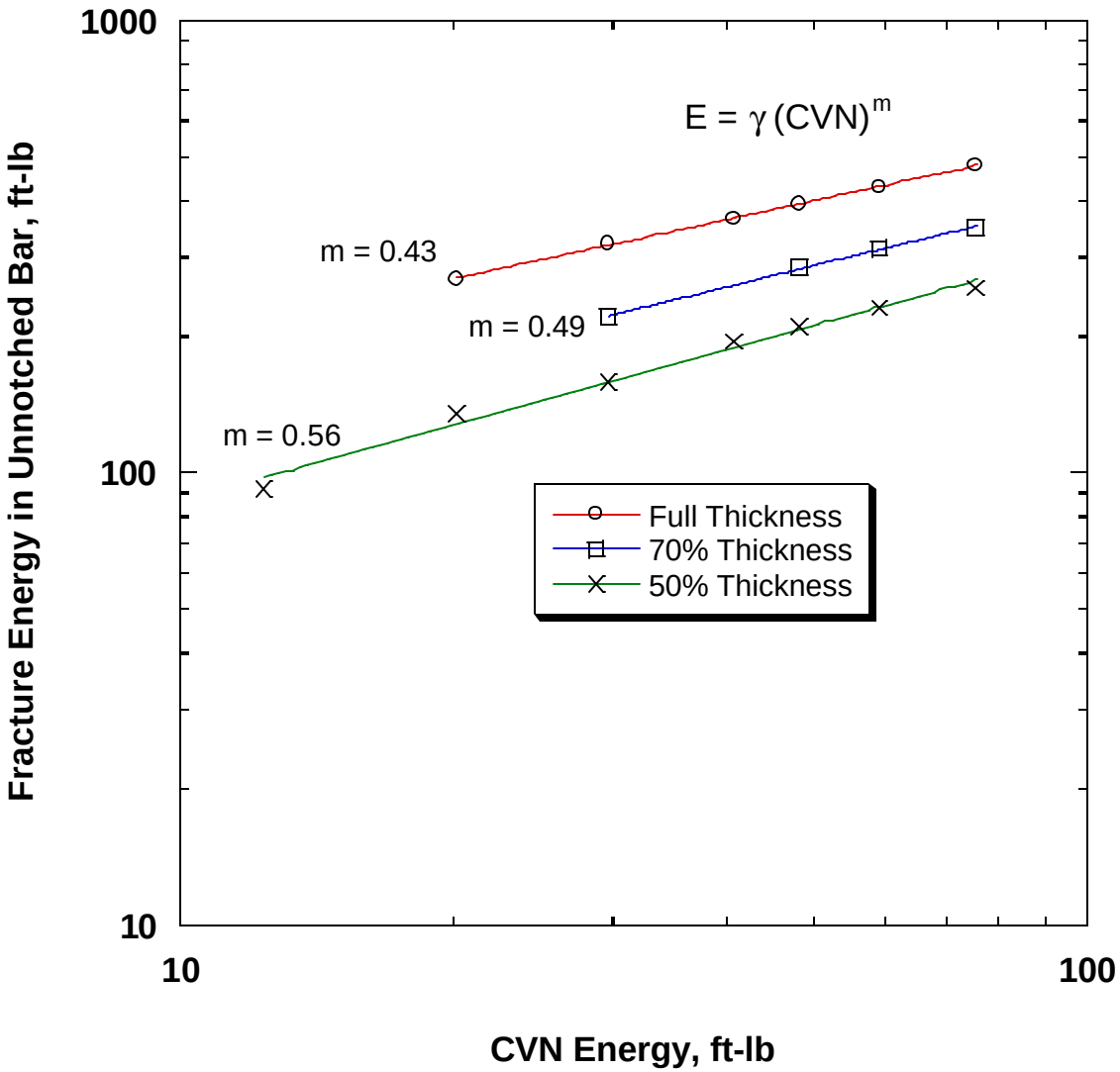

FIGURE 5.8. Relationship between fracture energy in the unnoched bar and Charpy energy.

5.3 Puncture of a Flat Plate

The configuration for the simulated puncture test on flat plates is shown in Figures 5.9 and 5.10. A 12-inch square plate is clamped around the edges, and a 1-inch diameter bar with a rounded end impacts the plate at 30 mph. The indenter was modeled with sufficient mass to puncture the plates. Puncture energy was measured as a function of plate thickness and initial porosity. The latter quantity was calibrated to Charpy energy, as shown in Fig. 5.2.

Figure 5.11 shows typical output from a simulated puncture analysis. At time = 0, the indenter contacts the plate and begins to impart its kinetic energy. The internal energy in the plate increases until the round indenter bar pierces through the plate, at which point

the internal energy reaches a plateau. This plateau represents the energy absorbed by the plate during puncture. Note that the indenter velocity decreases as it loses kinetic energy.

Figure 5.12 shows the plate puncture model at various time intervals. This particular run assumed an initial porosity of 0.0075, which corresponds to a Charpy energy of 461 ft-lb. While such a toughness is unrealistic for steels, these results help to illustrate a phenomenon that was apparent to a lesser degree in simulations of lower toughness materials. Namely, the material at the puncture location necks (i.e., thins) considerably. This behavior is not representative of tank car punctures that occur during accidents. This puncture simulation differs from a tank car puncture in two important respects:

- The plate is highly constrained, so it cannot bend significantly inward.
- The indenter size is on the order of the plate thickness, while the cross section of a coupler is an order of magnitude greater than plate thickness.

Both of these factors likely contribute to the observed necking in the simulated small-scale puncture test. The above limitations could be overcome with a wider plate and a larger indenter, but such a test would be cost prohibitive for routine material characterization.

Figure 5.13 is a plot of absorbed energy versus plate thickness in the simulated puncture test. The trend is approximately linear over the range of thicknesses considered, but the line does not pass through the origin.

Figure 5.14 shows the relationship between absorbed energy in the puncture test and absorbed energy in a Charpy test. The curve appears to be asymptotically approaching a maximum puncture energy. This trend can be explained by the observed necking behavior, as discussed below.

Figure 5.15 is a schematic illustration of tensile tests on two materials that have similar stress-strain curves but differing ductility. Material B fractures after more reduction in area than Material A. Note that both materials have similar elongation at fracture despite significantly different true fracture strains. The total energy absorbed by a tensile specimen is proportional to the area under the engineering stress versus elongation curve. There would be little difference in the measured energy to fracture in the two materials because the deformation prior to fracture is concentrated in a small volume. In a similar manner, the puncture energy in the small-scale test is insensitive to material toughness when significant local necking occurs.

Unfortunately, there appears to be no small scale laboratory puncture experiment that is truly representative of a typical tank car puncture. Even with a 1-inch diameter indenter, estimated puncture energies are on the order of 10,000 ft-lb, which would require a fairly large test rig. Performing larger-scale puncture tests with an indenter that is comparable in size to a coupler would probably be cost prohibitive.

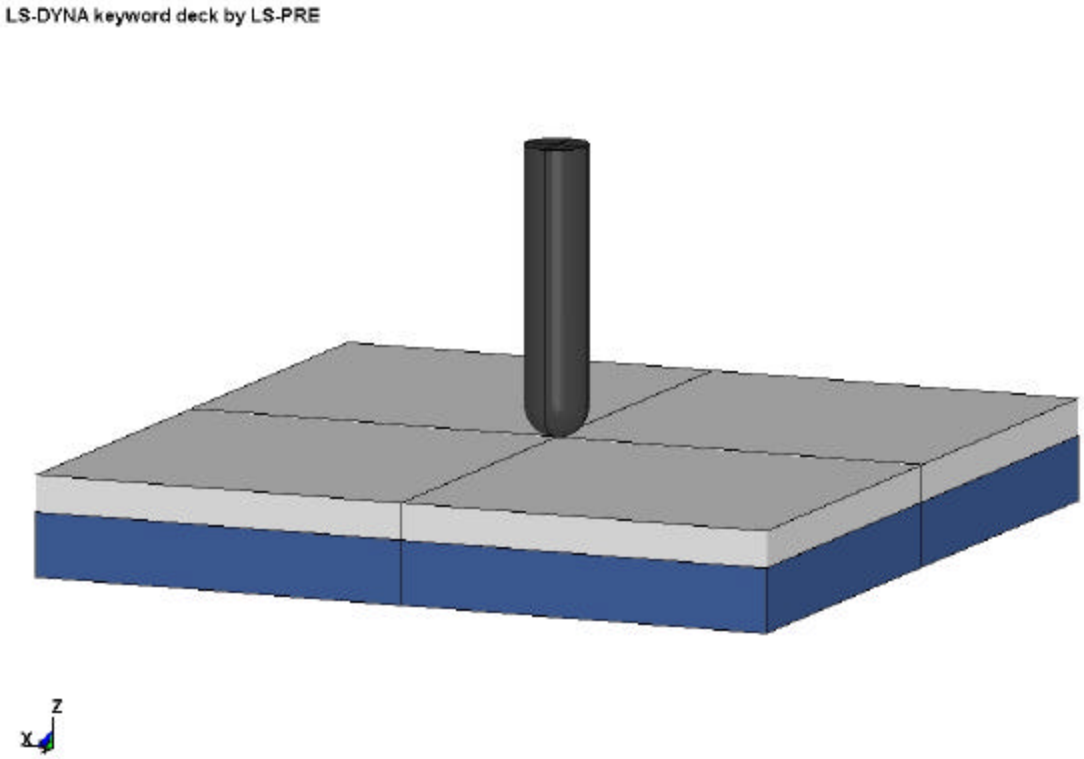

FIGURE 5.9 Model of a clamped plate with a 1-inch diameter indenter

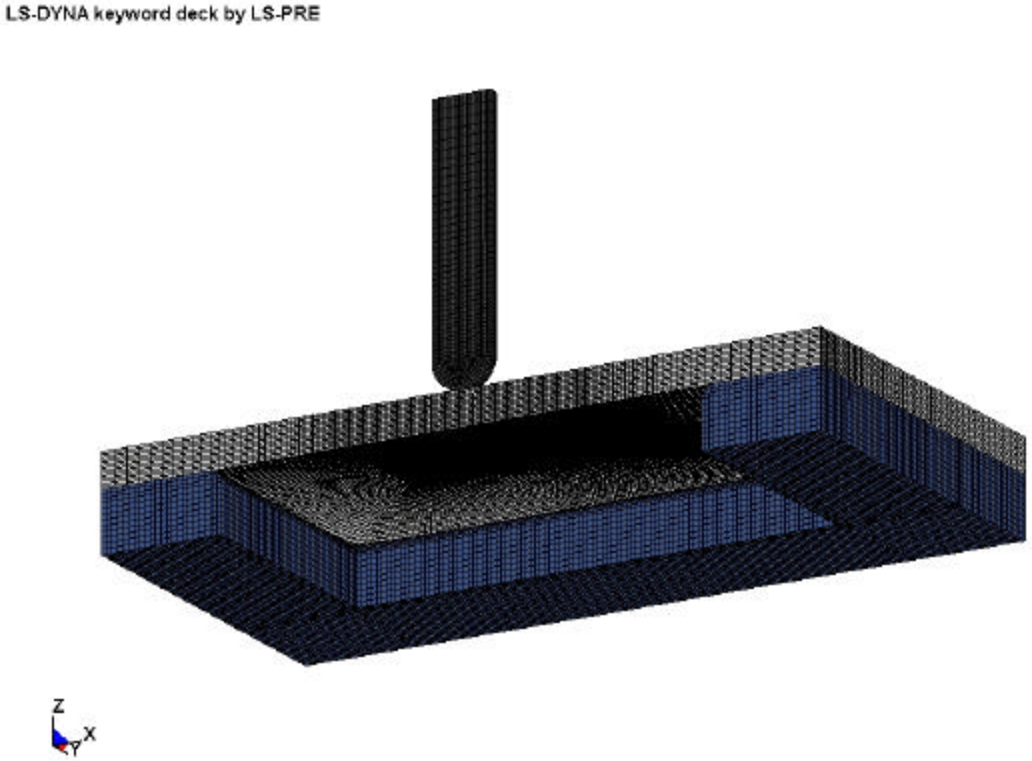

FIGURE 5.10 Half-symmetric model, which slows the finite element mesh.

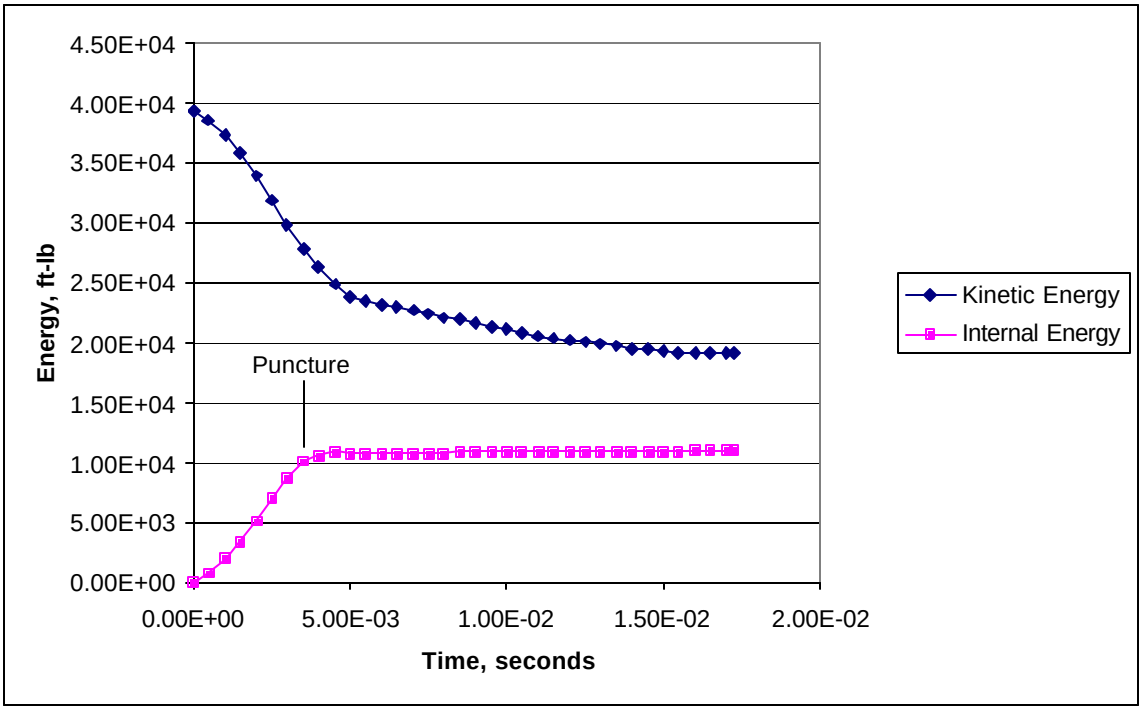

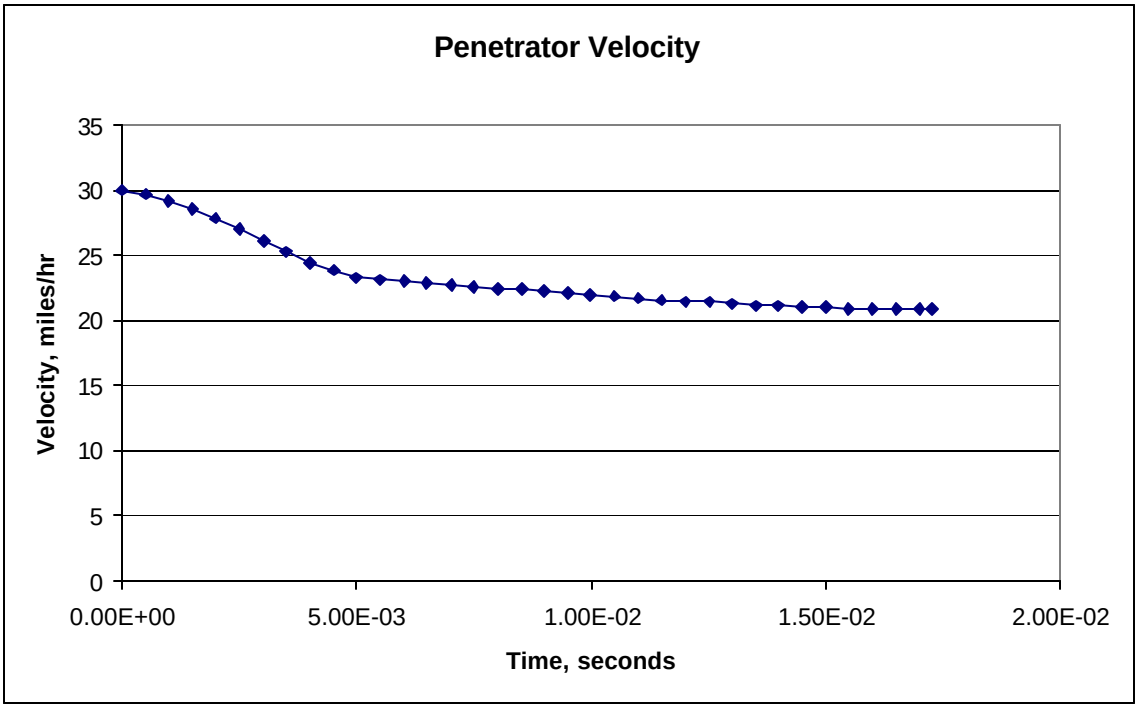

FIGURE 5.11 Typical results from the puncture simulation of a flat plate. Once the indenter pierces the plate, the internal energy (i.e., the energy absorbed by the plate) remains constant.

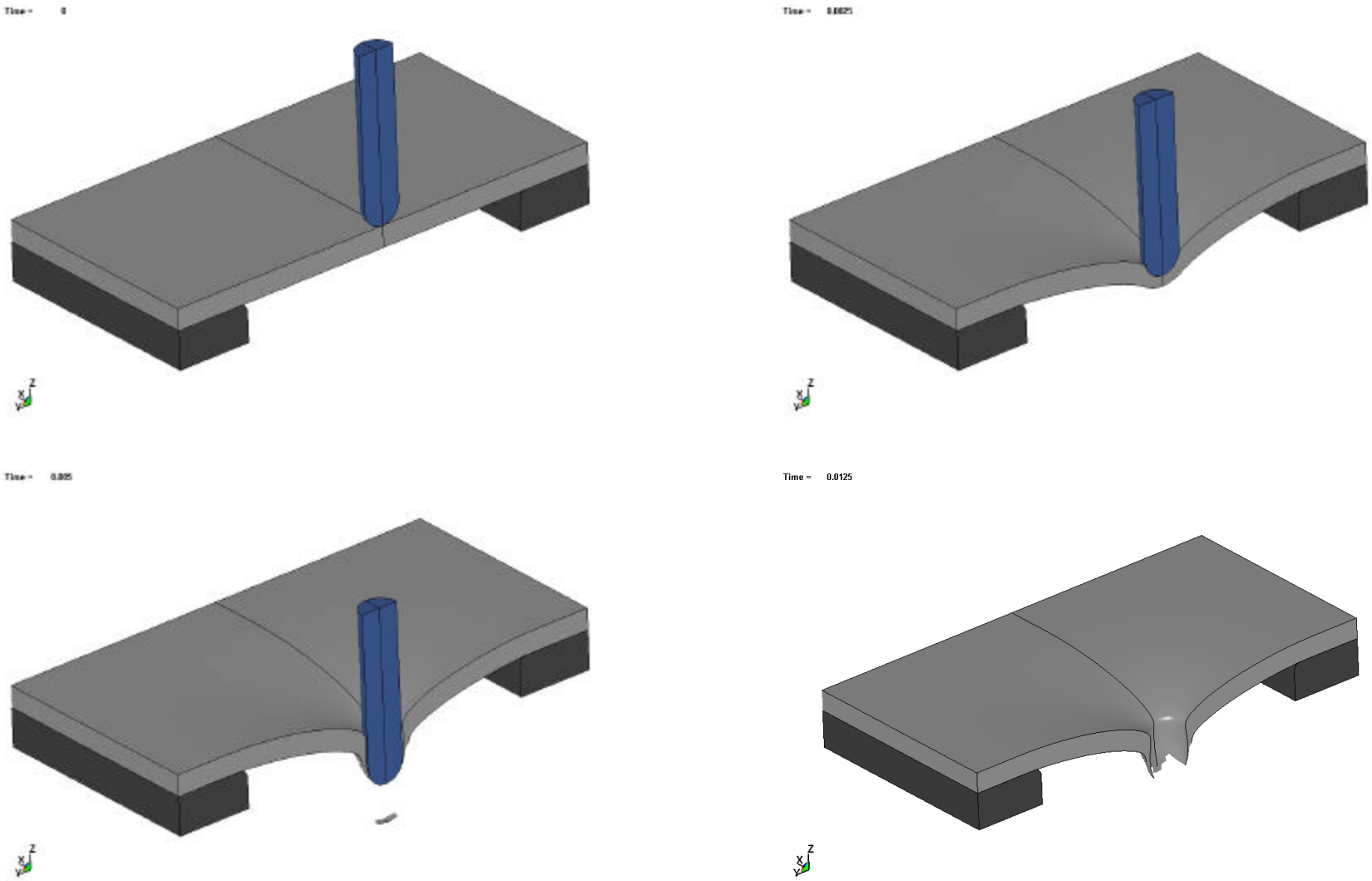

FIGURE 5.12 Simulated puncture test on a material with very high toughness. Note the significant necking at the puncture.

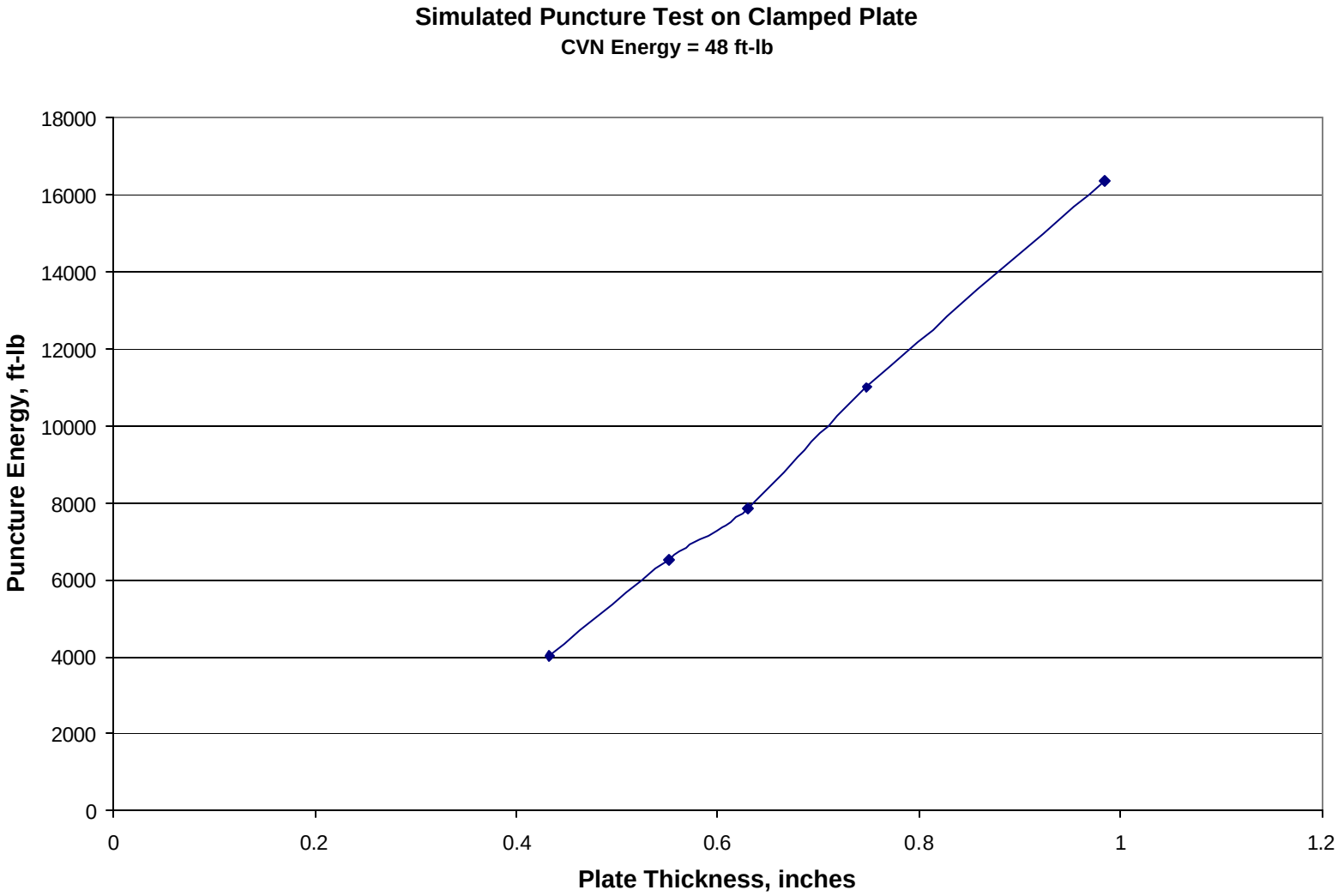

FIGURE 5.13 Puncture energy versus plate thickness in the simulated tests on clamped plates.

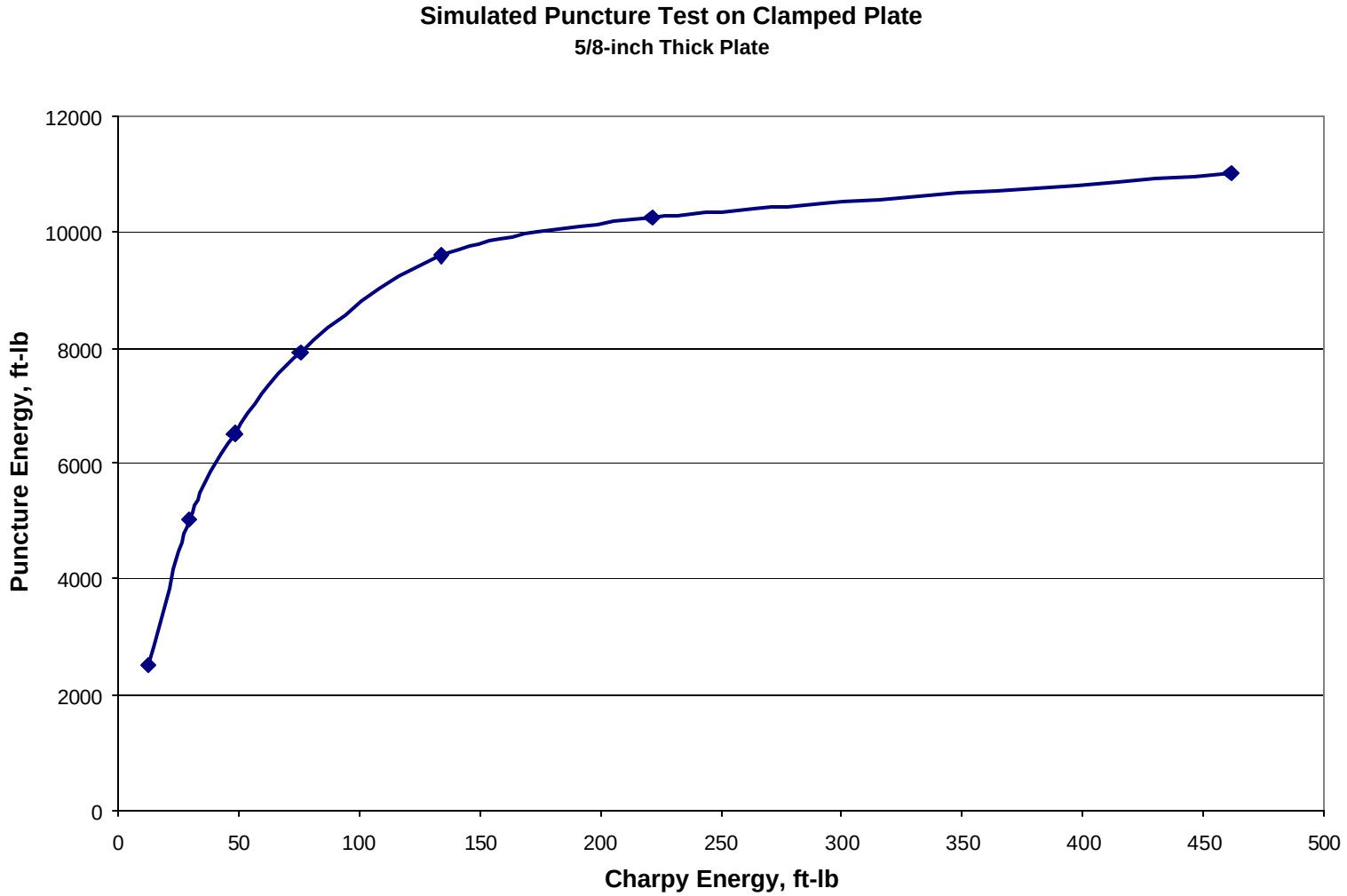

FIGURE 5.14 Puncture energy versus Charpy energy in the simulated tests on clamped plates.

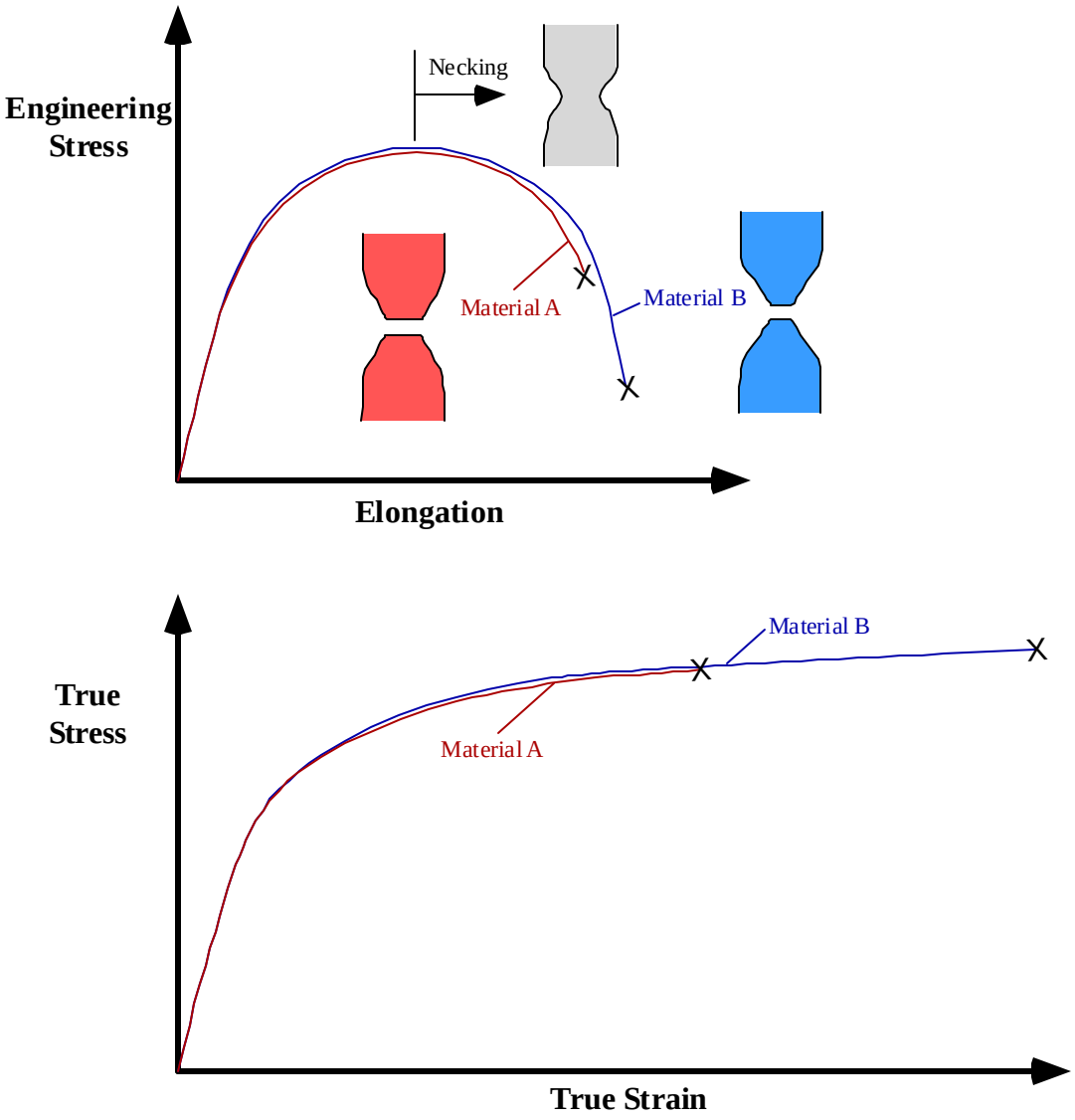

FIGURE 5.15 Schematic comparison of two materials with similar stress-strain behavior but differing ductility. The total energy absorbed by the two tensile specimens, which is proportional to the area under the engineering stress versus elongation curve, is similar despite the difference in the true stress-strain curves.

Impact testing of unnotched bars (Section 5.2) may be the best available alternative. Although this is not a true puncture test, it does provide information on fracture energy in the absence of a notch. At the very least, this test should be useful in validating the material model. If the Gurson-Tvergaard model can predict the fracture energy of both notched and unnotched specimens, it should produce realistic results in full-scale tank car puncture simulations.

6 CONCLUSIONS AND RECOMMENDATIONS

Lading loss through the head or shell of a tank car occurs through a ductile puncture mechanism in the vast majority of cases. Even when brittle fracture occurs in a tank car during an accident, it initiates at a notch-like feature. In the absence of a pre-existing notch, the tank car must first experience a ductile puncture before brittle crack propagation is possible. Although previous efforts to improve tank car steels have focused on low temperature toughness properties, the accident data indicates that the current focus should be on upper shelf toughness. There are relatively few brittle failures in older tank cars, and the problem of brittle fracture is essentially non-existent in normalized tank cars built after 1989. We recommend that a next-generation tank car steel specification be developed that incorporates very low sulfur allowances and sulfide shape control. We do *not* recommend an accelerated program to replace pre-1989 tank cars with cars made from the current generation of tank car steels.

A model calibrated from the accident database can be used to quantify the effect of design modifications and material properties on puncture resistance. The model and the database indicate that existing chlorine cars will experience a combined total of 44 punctures through the head and shell for every 1000 cars that are involved in an accident. If the proposed 600-lb car is adopted for chlorine transportation, but without improvements in steel properties, the number of expected punctures decreases to 12 per 1000 cars. On the other hand, if the chlorine car design remains the same and a new generation of steel with double the puncture resistance is adopted, the number of expected punctures decreases from 44 to 2 out of 1000 cars. If both the new steel and 600-lb car design are adopted, the predicted number of punctures is only 2 in 10,000.

Preliminary computer simulation indicates that a small-scale puncture experiment may not produce meaningful results due to local necking effects. A pendulum impact test on unnotched bars may be a reasonable alternative. At the very least, this test will be useful for validating the material model to be used in full-scale simulations of puncture in tank cars.

Recommendations for future work include:

- A feasibility study for C-Mn and microalloyed steels with low sulfur and sulfide shape control. This study would consist of experimental work as well as a cost/availability assessment of candidate steels. As many steel samples as is practical should be collected for ambient-temperature impact testing, tensile testing, fractography, and metallography. Such a study will quantify the relationship between upper-shelf toughness, chemical composition, processing, and microstructure. It will also indicate what toughness levels are attainable with economically viable steel specifications.

- Impact testing of unnotched bars to compare notched versus unnotched behavior, and to validate the material model for ductile fracture.

- Development of alternative tests for puncture resistance. Candidate tests should first be evaluated with dynamic finite element simulation. The most promising test method(s) could then be applied to real materials.

- Full-scale simulations of tank car impacts and punctures. Key parameters to be studied include wall thickness and material toughness. The effect of jackets, head shields, crumple zones, and other potential design features should also be evaluated.

- Development of a performance standard for puncture resistance.

7 REFERENCES

1. "Derailment of Canadian Pacific Railway Freight Train 292-16 and Subsequent Release of Anhydrous Ammonia near Minot North Dakota January 18, 2002." National Transportation Safety Board, March 2004.

2. NTSB Metallurgical Factual Report on Minot Derailment, April 2003.

3. Collision of Norfolk Southern Freight Train 192 With Standing Norfolk Southern Local Train P22 With Subsequent Hazardous Materials Release at Graniteville, South Carolina, January 6, 2005.

4. Philips, E.A. and Pellini, W.S., "Report on Behavior of Pressure Car Steels in Accidents" Report RA-03-6-48, RPI-AAR Railroad Tank Car Safety Research and Test Project, 1983

5. Hughes, J.P., Huer, C.F. and Anderson, T.L., "Fracture Behavior of Tank Car Steels in Accidents from 1981 Through 1994." Report RA-03-6-62, RPI-AAR Railroad Tank Car Safety Research and Test Project, 1998.

6. Anderson, T.L., *Fracture Mechanics: Fundamentals and Applications*. Third Edition, CRC Press, Boca Raton, FL, 2005.

7. Pellini, W.S., Eiber, R.J., and Olson, L.L., "Phase 03 Report on Fracture Properties of Tank Car Steels – Characterization and Analysis." Report RA-03-4-32, RPI-AAR Railroad Tank Car Safety Research and Test Project, 1975.

8. Eiber, R.J. and Olson, L.L., "Final Phase 03 Report – Material Study on Steels Used in Current and Former Tank Car Construction and from Cars Involved in Accidents." Report RA-03-5-33, RPI-AAR Railroad Tank Car Safety Research and Test Project, 1976.

9. Philips, E.A., "Evaluation of New Steels for Tank Cars." Report RA-03-7-53, RPI-AAR Railroad Tank Car Safety Research and Test Project, 1987.

10. Philips, E.A., "Evaluation of New Steels for Tank Cars, Phase II." Report RA-03-7-53, RPI-AAR Railroad Tank Car Safety Research and Test Project, 1991.

11. Anderson, T.L., Kirkpatrick, S.W., and McKeighan, P.C., Unpublished work pertaining to the investigation of the Minot derailment, 2005.

12. Anderson, T.L., "Elastic-Plastic Fracture Mechanics: Marine Applications." Report SSC-345, Part 2, Ship Structure Committee, 1990.

13. Manohar, M., Private communication, July 2006.

14. McKeighan, P.C., "Structural Reliability for Railroad Tank Cars," Ongoing FRA sponsored work, Southwest Research Institute, Volpe Contract No. DDTS.060183.000.801, 2006.

15. Gray, J.M., “Application of Modern Steels in Tank Car Construction.” Presented at the ASME ME 95 Congress and Exposition, November 1995.

16. Treichel, T.T., Hughes, J.P., Barkan, C.P.L., Sims, R.D., Phillips, E.A., and Saat, M.R., “Safety Performance of Tank Cars in Accidents: Probabilities of Lading Loss.” Report 05-02, RSI-AAR Railroad Tank Car Safety Research and Test Project, 2006.

17. Gurson, A.L., “Continuum Theory of Ductile Rupture by Void Nucleation and Growth: Part 1—Yield Criteria and Flow Rules for Porous Ductile Media.” *Journal of Engineering Materials and Technology*, Vol. 99, 1977, pp. 2-15.

18. Tvergaard, V., “On Localization in Ductile Materials Containing Spherical Voids.” *International Journal of Fracture*, Vol. 18, 1982, pp. 237-252.

19. Tvegaard, V., “Material Failure by Void Growth to Coalescence.” *Advances in Applied Mechanics*, Vol. 27, 1990, pp. 83-151.

20. Chu, C.C. and Needleman, A., “Void Nucleation Effects in Biaxially Stretched Sheets.” *Journal of Engineering Materials and Technology*, Vol. 102, 1980, pp. 249-256.

21. S.W. Kirkpatrick and R.W. Klopp, "Risk Assessment for Damaged Pressure Tank Cars," *2003 COMPUTER TECHNOLOGY AND APPLICATIONS*, ASME Publications, Proceedings of: PVP2003 - The 2003 ASME PVP Conference, July 20-24, 2003, Cleveland, Ohio, W. Reinhardt and D.J. Martin, Eds.

22. S.W. Kirkpatrick and R.W. Klopp, "Hazard Assessment for Pressure Tank Cars Involved in Accidents," ICrash 2000. Proceedings of the International Crashworthiness Conference, September 6-8, 2000, London, UK, E. C. Chirwa and D. Otte Eds., pp. 223-235.

23. R.W. Klopp, S.W. Kirkpatrick, and D.A. Shockey, “Damage Assessment of Tank Cars Involved in Accidents: Phase II - Modeling and Validation,” Final Technical Report to the Federal Railroad Administration, FRA Report, June, 1999.

24. LS-DYNA Keyword User’s Manual," Livermore Software Technology Corporation, Version 970, April 2003.

25. "TrueGrid Manual, Version 2.1.0," XYZ Scientific Applications, Inc., September 2001.

26. Stahl, S.W., “Puncture Resistance of Non-Pressure Tank Cars.” HLA Report No. 99320-0. HLA Engineers, Inc., 2000.